Spectroscopic Characterization of Photoresponsive Systems: from Chromoproteins to Switchable and Caged Compounds

---

Dissertation
zur Erlangung des Doktorgrades
der Naturwissenschaften

vorgelegt beim Fachbereich 14
der Goethe-Universität Frankfurt am Main

von
Christopher-Andrew Hammer
aus Caracas (Venezuela)

Frankfurt am Main 2018
(D30)

Vom Fachbereich 14 der
Goethe-Universität Frankfurt am Main als Dissertation angenommen.

Dekan	Prof. Dr. Clemens Glaubitz
1. Gutachter	Prof. Dr. Josef Wachtveitl
2. Gutachter	Prof. Dr. Alexander Heckel

Datum der Disputation: _____

Working hard is important.
But there is something that matters even more,
believing in yourself.

Harry Potter and the Order of the Phoenix - J. K. Rowling

Contents

List of Figures

List of Tables

List of Abbreviations

1PA	one-photon absorption
2PA	two-photon absorption
ATAS	**a**dvanced **t**ransient **a**bsorption **s**pectrometer
ACM	(7-**a**cetoxy**c**oumarin-4-yl)-**m**ethyl
BBO	β-**b**arium **bo**rate
BhC	(6-**b**romo-7-**h**ydroxy**c**oumarin-4-yl)methyl)
BWD	**b**and **w**idth **d**etector
CaF_2	calcium fluoride
cAMP	3',5'-**c**yclic **a**denosine **m**ono**p**hosphate
CCD	**c**harge-**c**oupled **d**evice
CO_2	carbon dioxide
CoA	**co**enzyme **A**
CPA	**c**hirped **p**ulse **a**mplification
CS_2	carbon disulfide
cw	**c**ontinuous **w**ave
DAS	**d**ecay **a**ssociated **s**pectra
DCM	**di**chloro**m**ethane
DEACM	(7-**die**thyl**a**mino**c**oumarin-4-yl)**m**ethyl
DMSO	**di**methyl**s**ulf**o**xide
DMCM	(6,7-**di**methoxy**c**oumarin-4-yl)**m**ethyl)

Dod	**dod**ecin
DTE	**dit**hienyl**e**thene
ET	**e**lectron **t**ransfer
ESA	**e**xcited **s**tate **a**bsorption
EWG	**e**lectron-**w**ithdrawing **g**roup
FAD	**f**lavin **a**denine **d**inucleotide
FI	**F**araday **i**solator
FLUPS	**fl**uorescence **up**conversion **s**pectroscopy
FMN	**f**lavin **m**ono**n**ucleotide
FRET	**F**örster **r**esonance **e**nergy **t**ransfer
FTIR	**F**ourier-**t**ransform **i**nfra**r**ed
FWHM	**f**ull **w**idth at **h**alf-**m**aximum
g	**g**erade
GLA	**g**lobal **l**ifetime **a**nalysis
GSB	**g**round **s**tate **b**leach
Glu	**glu**tamate
GM	**G**öppert-**M**ayer
GVD	**g**roup **v**elocity **d**ispersion
Hh	***H**alorhodospira **h**alophila*
HOMO	**h**ighest **o**ccupied **m**olecular **o**rbital
HRR	**h**orizontal **r**etro**r**eflector
Hs	***H**alobacterium **s**alinarum*
HWHM	**h**alf-**w**idth at **h**alf-**m**aximum
IC	**i**nternal **c**onversion
ICT	**i**ntramolecular **c**harge **t**ransfer

IET **i**ntramolecular **e**nergy **t**ransfer

IRF **i**nstrument **r**esponse **f**unction

ISC **i**nter**s**ystem **c**rossing

KDP potassium (german: **K**alium) **d**ihydrogen **p**hosphate, KH_2PO_4

LCAO **l**inear **c**ombination of **a**tomic **o**rbitals

LED **l**ight-**e**mitting **d**iode

LUMO **l**owest **u**noccupied **m**olecular **o**rbital

MCM (7-**m**ethoxy**c**oumarin-4-yl)**m**ethyl

MeOH methanol

Mt ***M**ycobaterium **t**uberculosis*

Nd:YVO_4 neodymium-doped yttrium vanadate

Nd:YAG neodymium-doped yttrium-aluminum-garnet

Nd:YLF neodymium-doped yttrium lithium fluoride

NIR **n**ear-**i**nfra**r**ed

NLT **n**on-**l**inear **t**ransmission

NMP **n**ucleoside **m**ono**p**hosphate

NOPA **n**on-collinear **o**ptical **p**arametric **a**mplifier

***o*NB** *ortho*-**n**itro**b**enzyl

OPA **o**ptical **p**arametric **a**mplifier

PBS **p**hosphate **b**uffered **s**aline

PC **P**ockels **c**ell

pcFRET **p**hoto**c**hromic **F**örster **r**esonance **e**nergy **t**ransfer

PDA **p**hoto**d**iode **a**rray

PCM (7-**p**ropionyloxy**c**oumarin-4-yl)**m**ethyl

PMT **p**hoto**m**ultiplier **t**ube

PPG **p**hotolabile **p**rotecting **g**roup

PPLN **p**eriodically **p**oled **l**ithium **n**iobate, $LiNbO_3$

PS **p**eri**s**cope

pss **p**hoto**s**tationary **s**tate

PTFE **p**oly**t**etra**f**luor**e**thylene

Rf **r**ibo**f**lavin

SE **s**timulated **e**mission

SFG **s**um **f**requency **g**eneration

SHG **s**econd **h**armonic **g**eneration

TCSPC **t**ime-**c**orrelated **s**ingle **p**hoton **c**ounting

TDG **t**ime **d**elay **g**enerator

TICT **t**wisted **i**ntramolecular **c**harge **t**ransfer

Ti:Sa **ti**tanium-doped **sa**pphire

TPEF **t**wo-**p**hoton **e**xcited **f**luorescence

TPIF **t**wo-**p**hoton **i**nduced **f**luorescence

u **u**ngerade

VRR **v**ertical **r**etro**r**eflector

1

Introduction

The indefatigable endeavor for the understanding of processes on a molecular level requires for their observation not only sophisticated techniques but their steady improvement. A famous example was the prediction of the simultaneous absorption of two photons in one quantum event, the so called two-photon absorption (2PA), by Maria Göppert-Mayer back in the year 1931.[1] As this process requires high photon density, its experimental evidence was first provided with the invention of the laser by Kaiser and Garrett 30 years later, as they observed fluorescence of Eu^{2+} upon 2PA.[2] With the proliferation of pulsed high-power lasers, the phenomenon attracted considerable attention due to its outstanding properties such as deeper sample penetration and high three-dimensional resolution accompanied with less phototoxicity, rendering the superiority of 2PA in many respects to the common one-photon absorption (1PA).[3] In analogy to Raman and infrared spectroscopy, 2PA is complementary to 1PA, enabling a 'new' spectroscopy with favorable characteristics.[4,5] Therefore, the two-photon technique is extensively applied in thriving research fields encountering material science, including data storage, in which different layers of a substance can be addressed to store and retrieve information,[6–11] and microfabrication.[11–19] In addition, 2PA found also application in other fields such as microscopy,[20–28] photodynamic therapy[29–35] and uncaging reactions where an effector molecule is encapsulated by a photocage and can be released upon irradiation.[36–40] Especially the last example joints the technique of 2PA with the strive for highly resolved spatiotemporal control of biological processes with light as harmless and ecological trigger.

At present, the research field exhibits only few potent two-photon activatable photocages as the computational calculation and deliberate design for increased efficiency regarding 2PA is yet an intricate challenge. One part of this work is dedicated to respond to this challenge with a molecular design strategy intended to achieve an enhanced 2PA

of a widely used and well-known photocage by introducing a molecular antenna for 2PA sensitization. This approach is based on the fact that readily available fluorophores display a high two-photon response which is by now not reached for photocages. The spectroscopic characterization of the antenna-photocage-system is one of the major objectives in this work, including its ultrafast photodynamics as well as the assessment of its 2PA with regard to the influence of the antenna and its functionality by means of the liberation of a caged molecule upon illumination.

A second class of photoactivatable compounds are photochromic molecules, also known as photoswitches as they are distinguished by the reversible switching upon light activation between at least two isomers. Among the plethora of photochromic compounds, the most prominent are stilbenes and azobenzenes which undergo a photoinduced cis-trans isomerization.[41–44] Additionally, photochromic reactions can also be rendered by an electrocyclization in which new bonds are formed or broken as it is found for fulgides (fulgimides) and dithienylethenes which are studied in this work. Moreover, photoswitches can be jointed with a strong fluorophore, enabling to modulate the fluorescence due to the photochromism. Aspects of the fluorescence modulation of such a cooperative dyad incorporating a dithienylethene are deduced from complementary time-resolved spectroscopic experiments in this study. Similar systems have already been thoroughly exploited in optical memory devices,[45–48] in fluorescent molecular switches[49,50] and as fluorescent markers in biological applications.[51–54] Especially, the last example constitutes the necessity of hydrolytic-stable photochromic compounds in aqueous environments. The second photochromic compound investigated in this work, a water-soluble fulgimide, meets this demand as by now only a few photoswitches have been studied in aqueous solution.[55–60] The ultrafast cyclization reaction of this photoresponsive system is spectroscopically characterized in this work.

The fourth photoresponsive system examined in this work is the flavoprotein dodecin. The cofactor flavin is distinguished by its chemical versatility accounted to its redox-active and light-sensory subunit isoalloxazine suiting the flavoprotein for electron transfer reactions e.g. in the citric acid cycle[61] or in the flavin-binding DNA photolyase which repairs damaged UV-irradiated DNA.[62] Dodecins exhibit a quaternary hollow-spheric structure in which the cofactor flavin is incorporated in an unique binding mode facilitating an ultrafast deactivation of the excited state of the flavin.[63–65] In general, dodecins can be divided into archaeal and bacterial flavoproteins where the first is already well characterized. Due to differing structural properties found in these two classes, different functional tasks are deduced. The aim of this work was to understand the function of the bacterial dodecin from *Mycobaterium tuberculosis* (*Mt*).

Part I of this work encompasses the theoretical framework of 2PA, fluorescence and photoactivatable compounds. Particularly, 2PA will be addressed in which a detailed theoretical description will be given (Chapter 2). Moreover, the classification of 2PA via several techniques will be discussed, as the quantitative characterization comprises technical obstacles yielding in partly divergent values for the 2PA. This is often caused by an inaccurate determination of the photon flux which is prone to any uncertainties within the excitation pulse. A solution to overcome this issue is the two-photon excited fluorescence (TPEF) technique.[66,67] In addition, fluorescence as a deactivation process and instrumental techniques to record time-resolved fluorescence are indited (Chapter 3). The last chapter of the theoretical framework (Chapter 4) introduces the molecule classes of photochromic and caged compounds. Part II delineates the materials and the applied experimental methods. Part III is devoted to the results in which Chapter 6 will focus on the spectroscopic characterization of the novel antenna-photocage-system with presumably improved characteristics regarding 2PA. Chapter 7 deals with the ultrafast photodynamics of photoresponsive systems with the emphasis on time-resolved fluorescence on the subpicosecond time scale. Here, the findings of the two photochromic compounds and the flavin-binding protein dodecin are presented. In the end, the achieved results of this work are concisely collated and a brief outlook is given (Part IV).

Part I

Theoretical Framework

2

Two-Photon Absorption

Two-photon absorption (2PA) is a third order non-linear optical (χ^3) process which can be described as simultaneous absorption of two low-energy photons in a quantum event, where the transition energy equals the sum of the energy of the two photons. In detail, a virtual state is created prior to the off-resonant absorption of the first low-energy photon. This virtual state shall not be understood as an *Eigenzustand* of the molecule but more as the interaction of the electric field of the photon with the molecule. The presence of this virtual state, which lives about 5 fs,[68] allows the second photon to induce a transition from the imaginary to the final state. Mostly, both photons in the 2PA process have the same energy (one-color) which usually corresponds to light of twice the wavelength required to reach an excited state in 1PA. This process is coined degenerated 2PA. The case where the two photons exhibit different levels of energy is called non-degenerated 2PA. Figure 2.1 encompasses in a simplified Jabłoński diagram the two cases of 2PA and the more common 1PA.

The main difference between 1PA and 2PA is the dependence on the photon flux (light intensity). While the involvement of only one photon in 1PA entails a linear dependence on the light intensity, the probability of 2PA exhibits a quadratic dependence, by virtue of the absorption of two photons at the same time. Consequently, the absorption of two photons at the same time can only be observed in focused beams of pulsed lasers with high-power outputs.

The compliant photon density within the use of such lasers and an appropriate lens is highest at the focal point and decreases along the z-axis with the squared distance leading to a very small fraction of excited molecules within the focus (Figure 2.2). The diffraction limit confines the dimensions of the excited volume approximately to the used excitation wavelength, resulting in a high three-dimensional (3D) resolution for

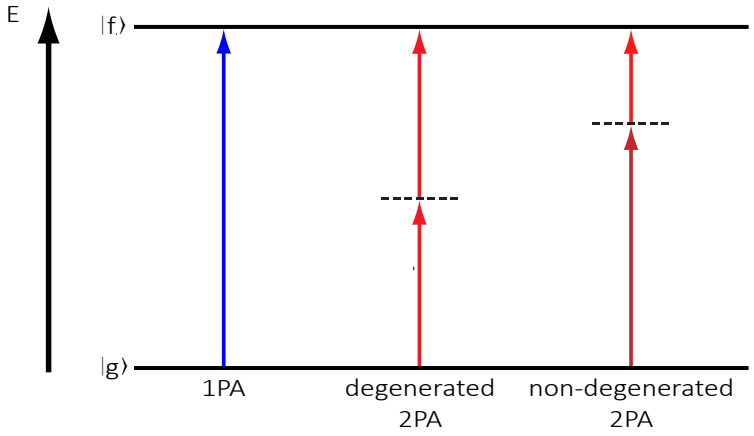

Figure 2.1: Simplified energy level diagram of one- (left) and two-photon absorption. The degenerated case where two-photons exhibit the same energy is shown in the middle, while the non-degenerated case encloses a transition of two photons with different amount of energies (right).

the process of 2PA. The off-resonant excitation provides the advantage of deeper sample penetration, while the excitation beam in 1PA is directly absorbed as it is incident on the material and further attenuated as it travels through the sample.

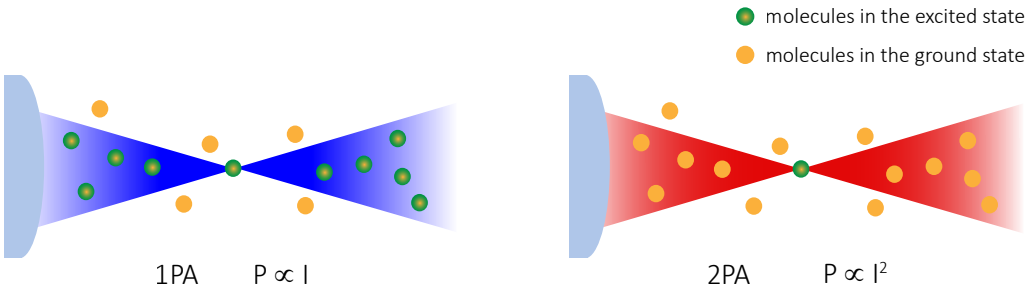

Figure 2.2: Schematic representation of the main difference between 1PA and 2PA. Within 2PA the quadratic intensity dependence provides 3D-resolution. Furthermore, this process is only observed at focal points with a pertinent photon density accessible with high-power pulsed lasers.[69]

Besides the high 3D-resolution and the deeper sample penetration, 2PA based on IR-light provides the access to the "phototherapeutic window" (690 - 950 nm) by means of harmless IR-light.[70,71] The combination of less phototoxicity and the above mentioned advantages enables the application of the 2PA technique to many biological systems.[72–80]

2.1 Theoretical Description of Two-Photon Absorption

According to the Lambert-Beers law, the extinction coefficient ε quantifies the strength of the 1PA of a material (Eq. 2.1).[81]

$$A = \varepsilon \cdot c \cdot d \tag{2.1}$$

where A is the absorbance, c the concentration of the investigated compound and d the optical path length of the sample.

In equivalence to the extinction coefficient, it is possible to express the 2P-response of a material through the so called two-photon cross section σ_{2P} in terms of the propagation equation with given wavelength incident on the 2P absorbing compound (Eq. 2.2).[82]

$$\frac{d\phi}{dz} = -\sigma_{2P} \cdot N \cdot \phi^2 \tag{2.2}$$

With ϕ as the the photon flux, N as the number of molecules in the ground state per volume unit and z as the propagation direction of the beam. The determination of σ_{2P} of two-photon absorbing materials is very desirable and will be discussed in detail in Section 2.4. At this point, it shall be noted that the σ_{2P} also known as two-photon absorption cross section (or 2PA cross section) is frequently abbreviated by a δ or $\sigma^{(2)}$. The unit of σ_{2P} is given by $m^4\,s/(molecule\ photon)$. Because of the relatively unwieldy expression the unit Göppert-Mayer (GM), in honor to Maria Göppert-Mayer, is commonly used and is defined as follows: 1 GM = 10^{-50} $cm^4 s/(molecule\ photon)$.

In case of additional 1PA, a second term has to be considered in which Eq. 2.2 becomes Eq. 2.3:[82]

$$\frac{d\phi}{dz} = -\sigma_{2P} \cdot N \cdot \phi^2 - \varepsilon \cdot N \cdot \phi \tag{2.3}$$

On the basis of the relation of the photon flux ϕ to the intensity of the beam by the photon energy $E_{ph} = \frac{hc}{\lambda} = h\nu$ (where h is Planck's constant and c the speed of light)[3,81,82]

$$\phi = \frac{I}{E_{ph}} \tag{2.4}$$

Eq. 2.3 can be expressed in terms of the beam intensity:[3]

$$\frac{dI}{dz} = -\frac{\sigma_{2P}}{E_{ph}} \cdot N \cdot I^2 - \varepsilon \cdot N \cdot I \tag{2.5}$$

With the considerations made above, a given 2PA band with a Lorentzian line shape resulting from a transition from the ground state $|g\rangle$ to a final state $|f\rangle$ σ_{2P} can be expressed in Eq. 2.6:[3]

$$\sigma_{2P} = \frac{2\,\pi\,E_{ph}^2\,L^4}{\varepsilon_0^2\,\rho^2\,c^2\,\Gamma}\,S_{fg} \tag{2.6}$$

with ρ as refractive index, ε_0 as the vacuum permittivity, Γ as the half-width at half-maximum (HWHM) and the factor L (L=(n^2 + 2)/3) which arises from the difference of the optical field in a medium to that in vacuum.

S_{fg} describes the squared sum of the product of oscillating dipole moment vectors induced by light, which matches the energy difference between the ground and an intermediate state (μ_{gi}), as well as the energy difference between the intermediate and the final state (μ_{if}) divided by the energy difference between the ground and the intermediate state and the energy of one photon involved in the 2PA process. Since the molecule rotates with many dipole moment vectors in solution, an average in the direction of the beam propagation is necessary. An approximated expression of S_{fg} valid for the most two-photon absorbers is given in Eq. 2.7:[3]

$$S_{fg} = \frac{1}{5}\left[\left(\frac{\Delta\,\mu_{gf}\,\mu_{gf}}{h\,\nu}\right)^2 + \sum_{i\neq f,g}\left(\frac{\mu_{gi}^2\,\mu_{if}^2}{(E_{gi}-h\,\nu)^2}\right)\right] \tag{2.7}$$

with $\Delta\mu_{gf}$ as the difference of the static dipole moment between ground and final state. The first summand in Eq. 2.7 is called the dipolar term abbreviated with D. The second term is coined the two-photon term (T).

2.2 Selection Rules

Depending on the molecule symmetry different selection rules have to be applied concerning 2PA. Considering centrosymmetric molecules all static dipole moments are negligible resulting in an absent dipolar term. The expression of σ_{2P} can than be simplified to:

$$\sigma_{2P} = C\frac{\mu_{gi}^2\,\mu_{if}^2}{(E_{gi}/h\nu)-1)^2\Gamma} \tag{2.8}$$

where C is a constant.

For the study of two-photon absorption four states have to be considered. In the present scenario, the ground $|g\rangle$ and the final state $|f\rangle$ which shall have *gerade* (g) parity, as well as the *ungerade* (u) intermediate $|i\rangle$ state and a virtual state which are depicted in Figure 2.3.

For centrosymmetric molecules transitions between two states of different parity (g→u and u→g) are electric-dipole-allowed for 1PA. Thus, in this case 1P-transitions are allowed from the ground to the intermediate state ($|g_g\rangle \rightarrow |i_u\rangle$) and from the intermediate to the final state ($|i_u\rangle \rightarrow |f_g\rangle$), while a direct transition from the ground to the final state is forbidden ($|g_g\rangle \rightarrow |f_g\rangle$. In case of 2PA, the photon energy is off-resonant with both transitions $|g_g\rangle \rightarrow |i_u\rangle$ and $|i_u\rangle \rightarrow |f_g\rangle$. However, a virtual state is created, as

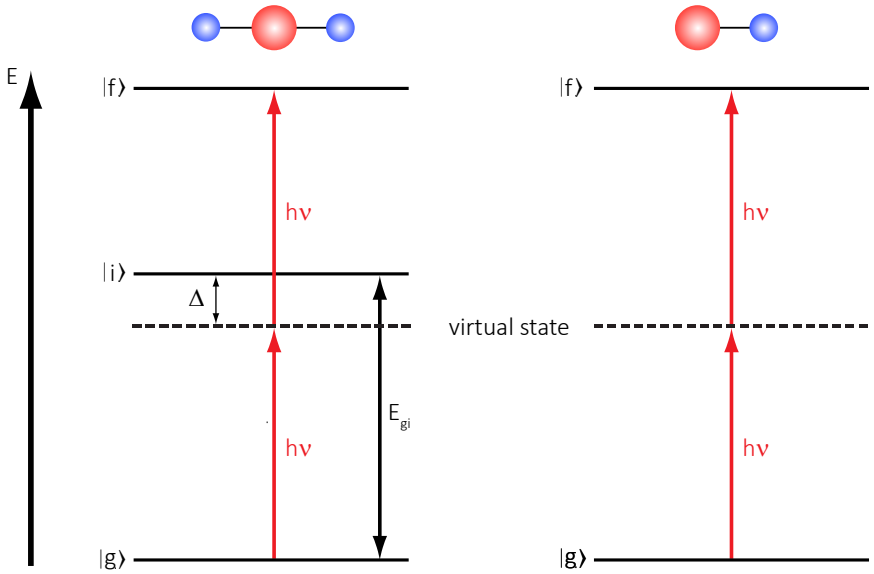

Figure 2.3: The four essential states for 2PA shown in the energy level diagram for centrosymmetric (left) and non-centrosymmetric molecules (right).[3]

the first absorbed low-energy photon interacts with the molecule. Due to its presence and its *ungerade* parity, the second photon can be absorbed to the final state and is therefore 2PA-allowed.

As a molecule exhibits a dipolar character when it is non-centrosymmetric, the D-term of σ_{2P} has now to be considered. The $|g_g\rangle \rightarrow |f_u\rangle$-transition is then allowed for 1PA and 2PA ($|f_u\rangle$ is now *ungerade*). However, the T-term (two-photon term) becomes now smaller than the D-term, since the $|i\rangle$ now lies energetically above $|f_u\rangle$ ($\Delta > h\nu$).

The D-term becomes smaller when $|i\rangle$ lies below $|f\rangle$, since Δ is now smaller than the photon energy, as seen for centrosymmetric molecules.

In a nutshell, transitions between states bearing the same parity (*gerade* to *gerade* or *ungerade* to *ungerade*) are 2PA-allowed for molecules with an inversion center, while a transition between two states of different parity is 1PA-allowed. An exclusiveness of states which can be reached via 1PA or 2PA does not exist for non-centrosymmetric molecules. However, there is no correlation between 1PA and 2PA transition strengths.

2.3 Enhancement of Two-Photon Cross Sections

The design of efficient 2P absorbers has been, to a certain extent, a trial and error process, since μ_{if}^2- values are experimentally not readily accessible. In contrast, μ_{gi}^2 and μ_{gf}^2 are proportional to the 1PA oscillator strengths so that their magnitudes can

be inferred from theoretical calculations. The first attempt to increase the σ_{2P} is the extension of the π-system within a given molecule as reported by Albota *et al.*[83] and is shown in Figure 2.4.

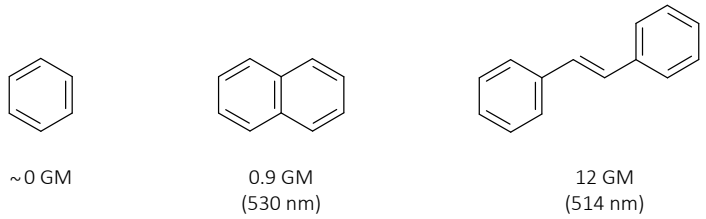

Figure 2.4: The introduction of extended π-systems within a molecule enhances the σ_{2P}. While the σ_{2P} of benzene is negligible, naphthalene exhibits a measurable value. The stilbene molecule enclosing a conjugated system between two benzenes provides a reasonably high σ_{2P}.[69]

Another strategy is the introduction of electron-withdrawing (A) and electron-donating (D) substituents to the chromophore which creates a push-pull-system with dipole character enhancing μ_{gf}^2. Those dipolar systems (D-π-A) display a dramatic increase of 2P response as larger charge displacements are present in a transition from a donor-centered HOMO to an acceptor-centered LUMO. This approach can also be applied to symmetric systems (D-π-A-π-D and A-π-D-π-A), so called quadrupolar systems.[83] A further extent are octupolar systems which expose triangular structures of quadrupolar systems within one molecule (D-(π-A)$_3$ and A-(π-D)$_3$). A σ_{2P} of 450 GM at an excitation wavelength of 740 nm has been reported with this approach.[69]

Since the mentioned approaches to increase σ_{2P} contain the use of large organic frameworks, an elevated hydrophobicity is caused. In terms of encountering biological demands under physiological conditions, a certain water-solubility should be given claiming a compromise between the σ_{2P} and the hydrophilic character.

Another approach to enhance the two-photon cross-section is the design of cooperative dyads comprising a strong 2P absorber as an antenna or sensitizer and a photoactivatable compound e. g. a photocage[84] or a photochromic compound.[85]

2.4 Determination of Two-Photon Cross Sections

To date, a plethora of techniques for the determination of σ_{2P} is available which can be divided into wave-mixing techniques, direct and indirect measurements. All of them are based on different principles exhibiting advantages and disadvantages. Thus, the comparison of absolute σ_{2P} is very delicate. Rumi *et al.* reviewed σ_{2P}-values for N,N-diphenyl-7-[2-(4- pyridinyl)ethenyl]-9,9-di-n-decylfluoren-2-amine (AF-50) and the photochromic bis(dibutylamino)stilbene obtained by different methods revealing substantial

disagreement between published values as they vary several orders of magnitude.[82] It is therefore difficult to assess a method which provides reliable values for σ_{2P}. The following sections shall provide a general overview of the two most commonly used experiments to determine σ_{2P}. While Section 2.4.1 is dedicated to the direct method 'z-scan', a detailed description will be devoted to the indirect method 'two-photon excited fluorescence' in Section 2.4.2. The latter was employed in this work to determine σ_{2P}.

2.4.1 Z-Scan

Direct measurements of σ_{2P} have great similarity to the characterization of the one-photon absorbance of a compound. Likewise, the attenuation of the 2P excitation beam, as it is absorbed by the sample, is the observed parameter within this method. The σ_{2P} can then be derived by detecting the transmittance as the intensity alters. This is accomplished by varying the spot size with a defined excitation pulse energy or by variation of the excitation pulse energy with given spot size. Z-scan and the non-linear transmission (NLT) method, respectively, avail this strategy. In the latter, the excitation pulse energy is measured before and behind the sample along the propagation plane in a series with different excitation pulse energies. With exact knowledge of the experimental parameters and the pulse properties, the dependence of the transmittance on the excitation energy can be exploited and σ_{2P} values can be derived.[86–88]

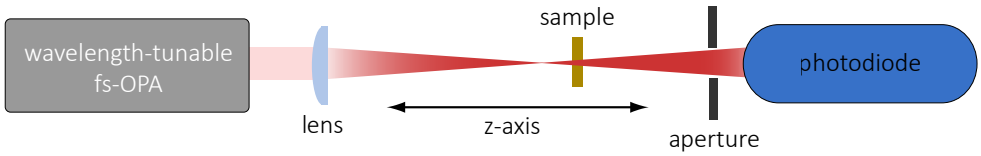

Figure 2.5: Schematic z-scan setup for the determination of σ_{2P}. The output of the wavelength-tunable OPA is focused with a lens on the sample which is moved along the z-axis. The transmissions at different positions are detected via a photodiode.

In the z-scan experiment the intensity is fixed while the position of the sample along the propagation axis (z-axis) of a focused laser beam is varied. Hence the sample experiences different spot sizes and the corresponding transmittance is detected (Figure 2.5). Since the two-photon process occurs in the focal point, the transmittance should be 1 when the sample is out of the focus range and the off-resonant excitation induces no 1PA. As the sample is translated towards the focal point, the probability of 2PA increases, hence the transmittance decreases and peaks at the maximum intensity, which is at the focal point where z is defined as 0. As the sample is "scanned" further away

from the focus, the transmittance increases until any two-photon process is absent and the transmittance is 1 again.[88–91] By dividing ϕ^2 in Eq. 2.2 and integrating over space, σ_{2P} can be determined using the initial condition $\phi(0)$ for the photon flux at z = 0:[82]

$$\begin{aligned} \frac{d\phi}{\phi^2} &= -\sigma_{2P} \cdot N dz \\ \int \frac{d\phi}{\phi^2} &= -\int \sigma_{2P} \cdot N dz \\ -\frac{1}{\phi} + \frac{1}{\phi(0)} &= -\sigma_{2P} \cdot N \cdot z \end{aligned} \tag{2.9}$$

By solving Eq. 2.9, the photon flux at each position z is expressed in Eq. 2.10:[82]

$$\phi(z) = \frac{\phi(0)}{1 + \sigma_{2P} \cdot N \cdot z \cdot \phi(0)} \tag{2.10}$$

In order to diminish the inaccuracy, several measurements of the pulse energy before and behind the sample are performed, although Eq. 2.10 indicates that a single measurement would be sufficient to determine σ_{2P}. Moreover, the dependence of σ_{2P} on the difference of two values with similar magnitudes ($\phi(0)^{-1}$ and $\phi(z)^{-1}$, Eq. 2.9) may result in uncertainties requiring a series of measurements. The above mentioned equations apply also to the NLT-experiment with the difference that the sample is fixed and the intensity is varied.

Eq. 2.10 premises an approximately constant beam intensity along the focal plane and that the attenuation of the beam intensity is only occurring from 2PA, neglecting the fact that the intensity differs within a focused beam along the z-axis as considered in Figure 2.5. Taking this into account, further parameters have to be considered in Eq. 2.10. Besides a collimated or a focused beam, the pulse profile which can differ in space and in time has to be deliberated which makes the interpretation of the measurement more sophisticated. The most common combination encompasses a focused beam with a Gaussian profile in space and time and an open aperture. The term "open aperture" is related to the fact that the beam is neither confined by any aperture, nor by the sensor of the detector. The accuracy of σ_{2P} gained with this combination within z-scan depends on the deviation of the experimental beam profile to an ideal Gaussian beam which is assumed in the referring equations. However, profiles divergent from the ideal case can lead to systematic errors entailing inaccurate σ_{2P}.

2.4.2 Two-Photon Excited Fluorescence

Indirect methods monitor deactivation processes of the excited state upon 2PA in order to acquire σ_{2P}. Two-photon excited fluorescence (TPEF) also known as TPIF (two-photon induced fluorescence) is one of the most prominent experiments belonging to the category of indirect methods.

The process of two-photon induced fluorescence is very similar to the radiative deactivation after one-photon excitation. However, the final state which is reached after two-photon absorption is disregarded as the molecule relaxes non-radiatively within $\sim 1\,\mathrm{ps}$[92] to the lowest vibrational state of the first electronically excited state (Kasha's rule).[93] From there, the molecule relaxes radiatively or/and non-radiatively to the ground state with a fluorescence lifetime typically in the ns-range. $\sigma_{2\mathrm{P}}$ can be inferred by monitoring the fluorescence intensity. Besides exact knowledge about the spatial and temporal properties of the excitation beam and the characteristics of the experimental setup, in particular of the detection system, it is required to access absolute $\sigma_{2\mathrm{P}}$ values. This can be circumvented with the relative measurement in which the intensity of a reference compound with known $\sigma_{2\mathrm{P}}$ is compared to the 2PA response of the investigated sample.

Recently, TPEF studies have been performed in the relative fashion, since the indirect method in an absolute way bears several difficulties. For the purpose of facilitated relative TPEF measurements, Xu and Webb established a reliable database with many reference compounds exhibiting absolute cross section values from the visible to the NIR-range.[66,67]

With TPEF a two-photon action cross section (σ_{TPA}) can be determined which displays a linear dependence on the product of $\sigma_{2\mathrm{P}}$ and the fluorescence quantum yield (ϕ_{fl}) upon two-photon activation (Eq. 2.11).[66,67]

$$\sigma_{TPA} = \phi_{fl}\,\sigma_{2P} \tag{2.11}$$

In the two-photon induced fluorescence process the number of absorbed photons per time unit ($N(t)$) is twice the number of fluorescence photons per time unit ($F(t)$). Under the assumption that self-quenching or stimulated emission effects are absent, the relation between absorbed and emitted photons is directly correlated to the experimental emission collection efficiency ψ and can thus be expressed as in Eq. 2.12.[66,67]

$$F(t) = \frac{1}{2}\,\psi\,\phi_{fl}\,N(t) \tag{2.12}$$

The measure in this experiment is the time-averaged fluorescence $\langle F(t)\rangle$ which can be expressed as:[66,67]

$$\langle F(t)\rangle = \frac{1}{2}\,\psi\,\phi_{fl}\,\sigma_{2P}\,c\frac{g_p}{f\,\tau}\frac{8\,\rho\,\langle P(t)\rangle^2}{\pi\,\lambda} \tag{2.13}$$

with c as the concentration, ρ as the refractive index of the solvent, λ as the excitation wavelength, $\langle P(t)\rangle$ as the time-averaged power and g as parameter of the pulse shape,

τ as the full width at half-maximum (FWHM) and f as the repetition rate of the laser. Eq. 2.13 comprises relevant parameters such as the fluorescence collection efficiency or the degree of second-order temporal coherence (g_p) which have to be characterized in absolute measurements. Nonetheless, the determination of these parameters can be avoided by using standard calibration samples with known two-photon action cross sections and new σ_{TPA} can be derived from the ratio of measured fluorescence signals Eq. 2.14.[66,67]

$$\frac{\langle F(t)\rangle_{cal}}{\langle F(t)\rangle_{new}} = \frac{\psi_{cal}\cdot\phi_{fl,cal}\cdot\sigma_{2P,cal}\cdot c_{cal}\cdot\langle P_{cal}(t)\rangle^2\cdot\eta_{cal}}{\psi_{new}\cdot\phi_{fl,new}\cdot\sigma_{2P,new}\cdot c_{new}\cdot\langle P_{new}(t)\rangle^2\cdot\eta_{new}} \tag{2.14}$$

with *cal* as index for the calibration sample and *new* as index for the compound with the to determinable σ_{TPA}. Under identical conditions the ratio of fluorescence signals can be simplified to:[66,67]

$$\phi_{f,new}\sigma_{2P,new} = \frac{\langle F(t)\rangle_{new}}{\langle F(t)\rangle_{cal}}\frac{c_{cal}}{c_{new}}\frac{\eta_{cal}}{\eta_{new}}\phi_{f,cal}\sigma_{2P,cal} \tag{2.15}$$

The σ_{TPA} can now be calculated with knowledge about concentration, refractive index, incident pulse power, the σ_{TPA} of the calibration sample and the measured fluorescence intensities.

The schematic setup is depicted in Figure 5.8 in Section 5.5.2 where the pulse of a wavelength-tunable laser is continuously monitored with a fiber spectrometer to diminish any uncertainties of the pulse within the measurements. The beam is focused with a microscope objective on the sample. The generated fluorescence upon two-photon absorption is subsequently collected with a second objective and guided to the detector, while any scattering or back reflections can be depleted with adequate filters.

In order to obtain a broadband two-photon absorption spectrum with σ_{TPA}, the sample can be excited with 2P with various wavelengths. Before a wavelength-dependent measurement is performed, a power-dependent experiment should be carried out by varying the pulse intensity at a fixed excitation wavelength. This procedure displays whether the dependence of the fluorescence intensity on the squared laser beam intensity is given. Otherwise the results could be misinterpreted. Stimulated emission, ground state depletion, linear absorption and excited state absorption may be reasons for deviations from the dependence on the quadratic laser intensity. Moreover, a broadband fluorescence detection is advantageous, as scattered light, cosmic peaks or other artifacts would lead to an overestimation of detected light for example by using a photon counter.

Fluorescence as measure for two-photon excitation is advantageous since it is very sensitive. Thus high energy pulses are not required as in the case of z-scan. However, the pronounced dependence on the spontaneous emission confines the method to molecules with a fluorescent character. Apart of the pertinent fluorescence, the method requires detailed knowledge of the fluorescence properties, particularly the fluorescence quantum yield upon 2PA. Since this parameter is hard to determine, the approximation of 1P fluorescence quantum yields have to be made. Hence, strong fluorescent signals do not indicate directly large σ_{2P} as the fluorescence quantum yield has to be considered.

3

Fluorescence

This chapter provides a general overview to fluorescence. Section 3.1 gives insight into the basic principles of fluorescence, while Section 3.2 will focus more closely on the spectroscopic instrumentation for capturing fluorescence. In particular the Kerr shutter as time-resolved method for the observation of fluorescence will be discussed.

In the past decades the attention on fluorescence as non-invasive technology to investigate matter increased significantly. Nowadays, fluorescence has become an indispensable method, based on its high sensitivity and the ease of applicability in biological issues and demands.[92,94,95] It is considered as one of the leading tools in the research field of biochemistry, biophysics and physical chemistry but has also a substantial impact in other disciplines as depicted in Figure 3.1.

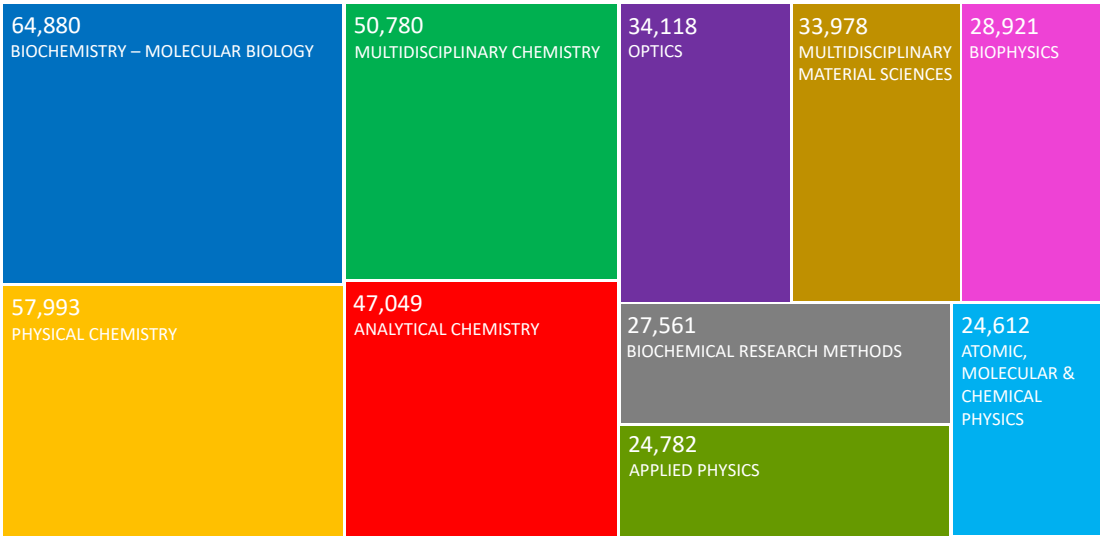

Figure 3.1: Fluorescence-related publications in different research fields visualize the massive impact of fluorescence as indispensable tool for non-invasive investigation of matter.[96]

3.1 Basic Principles on Fluorescence Spectroscopy

Interaction of electromagnetic radiation with matter can lead to the absorption of a photon when its energy matches the transition energy between an occupied and an unoccupied state.[81,92] From the excited state various processes can take place (Figure 3.2). Radiation-free deactivation is achieved by converting the electronic energy into rotational, translational and vibrational energy. On the other hand, radiative relaxation from an excited state back to the ground state is called luminescence, in particular fluorescence and phosphorescence. The type of luminescence is defined by the multiplicity of the excited state from where it is emitted. Fluorescence is the spontaneous emission of a photon from an excited singlet state.

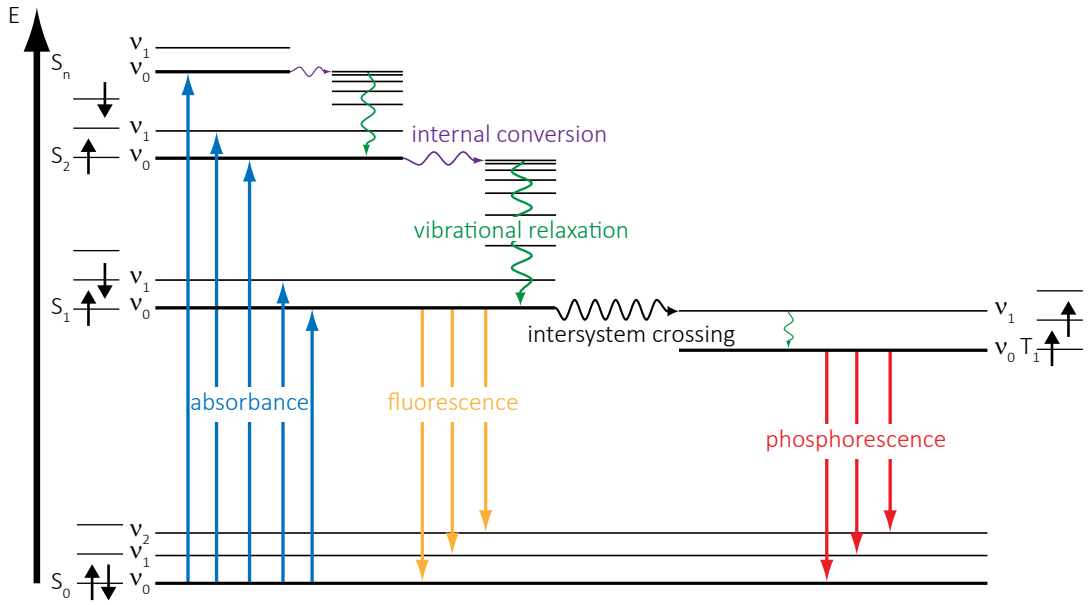

Figure 3.2: Jabłoński diagram with schematic representation of processes occurring between the electronic and the vibrational states after an initial absorption of a photon. The diagram is based on reference 97.

After the initial absorption into an excited vibronic state, the molecule descends to the lowest vibrational level of the reached excited state (vibrational relaxation). From there, the molecule can relax radiation-free to a vibrational level of a lower singlet state which is called internal conversion (IC). The molecule undergoes these two processes until it reaches the lowest vibrational level of the lowest excited state, the S_1-state. These radiationless relaxation pathways are usually very fast. Times for the internal conversion are typically in the order of 10^{-12} s[92,98] which is the reason for the subsequent emission from the first excited state. This is manifested in "Kasha's rule".[93]

Exceptions from this rule are observed for example for azulene, 1,4,7-triazacycl[3,3,3]-

azine and ovalene which violate Kasha's rule by fluorescing from the S_2-state. In particular, certain circumstances are necessary for the violation of Kasha's rule. In case of azulene with an IC-time of 10^{-12} s and 1,4,7-triazacycl[3,3,3]azine the energy gap between the S_2 and the S_1-state is comparatively high, thus the IC related to these two states is much slower than the $S_1 \rightarrow S_0$-transition. As a result, a photoexcited azulene[99] and 1,4,7-triazacycl[3,3,3]-azine[100,101] emit from the S_2-state. Another reason leading to an exception of Kasha's rule can be seen on the example of ovalene, where the energy gap between S_2 and S_0 is large but the transition gap between S_1 and S_2 and the oscillator strength of the $S_0 \rightarrow S_1$-transition are very low.[102,103] In this case, a relative long fluorescence lifetime from the S_1-state and a thermal population of the S_2-state are observed and hence the $S_2 \rightarrow S_0$-emission becomes competitive to the typical emission from the S_1-state. This so called two-level emission can be suppressed at lower temperatures as the thermal population of the S_2-state decreases. The third exception to this rule was detected for several hydrocarbons with a reasonable high sensitivity, where triplet-triplet annihilation was used in order to diminish any stray light sources.[104,105]

As the molecule is in the lowest vibrational level of the lowest excited state (S_1), a vertical transition to the electronic ground state (S_0) takes place in accordance to the Franck-Condon-principle. Due to the previously dissipated energy by translational, rotational or vibrational relaxation, fluorescence is shifted to higher wavelengths in respect to the absorbance which refers to the Stokes shift. A further reason for red-shifted fluorescence is based on solvent reorganization. The transition from the first excited to the ground state ($S_1 \rightarrow S_0$), where the two unpaired electrons in the ground and the excited state exhibit opposite spin-orientation, is completed after a few nanoseconds.[92] Typical spontaneous emission rates are therefore in the range of $10^{-8}\,s^{-1}$ whereas phosphorescence takes place on a time scale of microseconds to hours. In general, phosphorescence occurs when the molecule undergoes intersystem crossing (ISC) which is an isoenergetic transition between two states of different multiplicity. This optically forbidden process from a singlet to a triplet state can only be realized by a strong magnetic field. In case of light, the intrinsic magnetic field is easily compensated by its electric field. Nevertheless, strong spin-orbit-coupling, an intrinsic perturbation of the molecule, can cause a spin flip of the excited electron. As a result the spins in the ground and in the electronically excited state display the same orientation. From there, the molecule descends the vibrational states until it is trapped at the lowest triplet energy level T_1, since a return to the ground state is again spin-forbidden. However, a strong spin-orbit-coupling relaxes the spin forbidden transition by a further spin flip. Consequently, long-lived emission by means of phosphorescence is detected as a result of the recombined electrons in the ground state.

3.2 Time-Resolved Fluorescence

Time-correlated single photon counting (TCSPC) is characterized by its ease of use and therefore considered as the most-widely applied technique to investigate fluorescence behavior in the ns-range.[106–108] The method TCSPC comprises a relatively inexpensive setup which is distinguished by high sensitivity. The principle is based on the assumption that the probability of a single photon detected at a certain time delay is proportional to the fluorescence intensity at this very time. Hence, many excitation pulses cause a fluorescence decay histogram from which a lifetime of the excited state can be inferred.

In practical, the excitation pulse is split, where one part is directly detected by a photodiode setting the starting value and the second fraction is used to photoexcite the sample and thus generate fluorescence. As a photomultiplier, which serves as a photon counter, detects one incoming fluorescence photon, the stop-signal is set. This start-stop-sequence is repeated over several times and yields the above mentioned histogram.

Besides the above mentioned advantages, the highest-achieved time-resolution of the TCSPC is in the range of some picoseconds convoluted by the instrumental response.[109] Observation of fluorescence dynamics in the femto- to picosecond range requires other techniques *i.e.* the Kerr shutter or the upconversion. Both methods rely on the technique of optical gating.[109–111]

Table 3.1: Comparison of Time-resolved Fluorescence Methods.[112]

method	time resolution	remarks
TCSPC	20-30 ps	electronics-limited IRF
streak camera	2-10 ps	ease of use
upconversion	40 fs[113]	difficult alignment
Kerr shutter	100 fs[114]	broadband spectra

While the upconversion provides single-wavelength fluorescence traces by monitoring the sum frequency of a so called gate pulse and the spontaneous emission, broadband fluorescence spectra can be obtained with the Kerr shutter. This method for capturing ultrafast fluorescence depends on the Kerr effect which refers to the birefringence induced in an optical material upon application of an electric field. This is realized by focusing a 'gate pulse' and the polarized fluorescence on an isotropic Kerr medium between two polarizers with crossed orientation to each other. Hence, anisotropy is generated and subsequently, a change in polarization of the fluorescence is induced,

allowing a certain amount to pass through the second polarizer.

3.2.1 Optical Gating

The Kerr shutter and the upconversion rely on the principle of optical gating where fluorescence light and a gate pulse are superimposed in an optical switch. Thus, the gate pulse induces temporary modifications of the fluorescence characteristics and hence a time-resolution, which depends in first approximation on the length of the used laser pulses, is created.

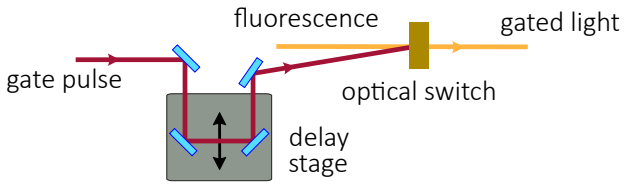

Figure 3.3: Schematic representation of optical gating as it is realized for the upconversion and for the Kerr shutter.

By varying the path length of the gate pulse with respect to the excitation pulse, a time delay between the two pulses is introduced in order to monitor fluorescence spectra time-dependently. Each variation of the beam path Δs results in a change of time Δt in respect to the speed of light c (Eq. 3.1).[81]

$$\Delta t = \frac{\Delta s}{c} \tag{3.1}$$

The optical switch used in the upconversion is a β-barium borate crystal (β-BaB_2O_4) abbreviated as BBO which is applied in many non-linear optical processes, due to its large birefringence and small dispersion.[115] Generated fluorescence light with the frequency ω_{fl} and the wave vector $\vec{k}_{\mathrm{fl}}$ is focused together with the gate pulse (ω_{g}, $\vec{k}_{\mathrm{g}}$) into the BBO-crystal. In the case of temporal and spatial overlap of both pulses, frequency mixing takes place due to the non-linear 2$^{\mathrm{nd}}$ order susceptibility ($\chi^{(2)}$) at perfect phase matching conditions (Eq. 3.2):[116]

$$\Delta\vec{k} = \Delta\vec{k}_{fl} + \Delta\vec{k}_{g} - \Delta\vec{k}_{s} = 0 \tag{3.2}$$

and a sum frequency signal is obtained:[116]

$$\omega_s = \omega_{fl} + \omega_g \tag{3.3}$$

In this non-linear process energy and momentum are conserved, leading to no dissipative energy. A drawback of this technique is the fact that the thickness of the crystal

and fixed crystal angles restrict the phase matching only to a small frequency range. Therefore, obtaining transient fluorescence spectra via the upconversion method is aggravated. One approach to realize a broadband fluorescence spectrum would be the use of many scans, each with varying phase matching angles. This technique demands long measurement times and entails the drawback of obtaining low quality spectra caused by low-frequency noise. Another approach to enlarge the acceptance band width $\Delta\nu$ can be inferred by Eq. 3.4.[117]

$$\Delta\nu \sim \frac{\left(\frac{1}{d}\right)}{\left(\frac{c}{V(\nu_s)} - \frac{c}{V(\nu_{fl})}\right)} \tag{3.4}$$

with V as the group velocities of the light and d as the thickness of the non-linear crystal. Hence, a thin crystal with low-dispersion such as KDP (potassium dihydrogen phosphate, KH_2PO_4) should positively affect $\Delta\nu$. Furthermore, gate pulses in the infrared region should decrease the dispersion. Thus it is possible to obtain a broad spectral range of $10.000\,\mathrm{cm}^{-1}$ by using a KDP-crystal with a thickness of (0.1 mm) and a gate pulse with a central wavelength of 1300 nm.[118] This method with the acronym FLUPS (fluorescence upconversion spectroscopy) became very popular in terms of ultrafast spectroscopy and is nowadays commercially available.

Differently, phase matching conditions have not to been considered with the Kerr shutter used in this work. It therefore provides intrinsically broadband fluorescence spectra. On the other hand, the time resolution becomes worse compared to the IRF (instrument response function) of the upconversion which is in the range of couple of ten femtoseconds. Nevertheless, time resolution below 100 fs can be achieved with the Kerr shutter.

3.2.2 Kerr Shutter

The Principle

In contrast to linear optics, the linear proportionality between the polarization $\vec{P}$ and the electric field strength $\vec{E}$ is not given in non-linear optics anymore, due to the interaction of high-energetic laser light with electrons. While the first term of Eq. 3.5 would suffice to describe a linear relationship between $\vec{P}$ and $\vec{E}$, the non-linearity, found in the processes exploited by the upconversion or the Kerr shutter, can be represented by a Taylor series development of polarization in higher order terms depending on the electric field strength.[119]

$$\vec{P}(\vec{E}(t)) = \varepsilon_0 \left[\chi^{(1)} \cdot \vec{E}(t) + (\chi^{(2)} \cdot \vec{E}(t)) \cdot \vec{E}(t) + (\chi^{(3)} \cdot \vec{E}(t) \cdot \vec{E}(t)) \cdot \vec{E}(t) + ...\right] \tag{3.5}$$

where ε_0 is the absolute dielectric constant in vacuum and $\chi(n)$ are the n$^{\text{th}}$ order of the dielectric susceptibility tensors which are way smaller for higher orders and can be therefore neglected at small electric field strengths.

While the upconversion is an optical method relying on a non-linear 2$^{\text{nd}}$ order process, the Kerr shutter is based on the non-linear 3$^{\text{rd}}$ order susceptibility ($\chi^{(3)}$) of a material which is proportional to the non-linear part of its refractive index n_0. The Kerr effect, also known as the quadratic electrooptic effect, often uses isotropic media as Kerr medium, hence the 2$^{\text{nd}}$ order susceptibility becomes zero and $\chi^{(2)}$-processes e.g. sum frequency generation are minimized. The first and the third order of the polarization $\vec{P}$ yields the total polarization of the Kerr medium (Eq. 3.6):

$$\begin{aligned}\vec{P}(\vec{E}(t)) &= \vec{P}^{(1)}(\vec{E}(t)) + \vec{P}^{(3)}(\vec{E}(t)) \\ &= \varepsilon_0 \left[\chi^{(1)} \cdot \vec{E}(t) + \left(\chi^{(3)} \cdot \vec{E}(t) \cdot \vec{E}(t) \cdot \vec{E}(t)\right)\right] \\ &= \varepsilon_0 \left[\left(\chi^{(1)} + \chi^{(3)} \cdot (\vec{E}(t))^2\right) \cdot \vec{E}(t)\right]\end{aligned} \tag{3.6}$$

By applying a strong time-dependent electric field, the refractive index n is changed by a non-linear intensity-dependent part which is described with the following equation:[120–122]

$$n_{I,t} = n_0 + n_2 I(t) = n_0 + \Delta n(t) \tag{3.7}$$

with n_0 as the refractive index without the electric field and Δn as the change of the refractive index in respect to the polarization of the gate pulse. The refractive index is independent of the intensity of the electric field *I(t)*, thus the expression is extended by n_2 which considers the strength of the applied field to the intensity over time:[123]

$$n_2 \approx \frac{1}{n_0^2\, \varepsilon_0 c} \cdot \chi^{(3)} \tag{3.8}$$

The intensity is given by:[123]

$$I = \frac{1}{2} \cdot n_0\, \varepsilon_0\, c\, |E|^2 \tag{3.9}$$

Kerr gating can be realized upon photoexcitation of the investigated sample. The generated fluorescence is collected via a Schwarzschild objective and then passed through a polarizer. The linear polarized fluorescence is impinged on the isotropic Kerr medium which is located between two crossed thin-film polarizers. Due to the crossed orientation of the analyzer (second polarizer) with respect to the first polarizer, the linear polarized fluorescence is not able to pass through the analyzer. In presence of the gate pulse and temporal and spatial overlap with the fluorescence light, birefringence is induced, hence anisotropy leads to partly change of the polarization of the fluorescence impulse which is not anymore linear but elliptical.[124] A certain amount is now able to pass through the gate for detection which is open for the duration of the length of the gate pulse.

Since this principle is only based on the anisotropic change of the refractive index and is therefore wavelength-independent, the Kerr shutter does not have to meet any phase matching conditions to obtain broadband emission spectra. By varying the length of the beam path of the gate pulse with respect to the excitation pulse via an electronic delay line, the intensity of the fluorescence can be detected at different delay times.

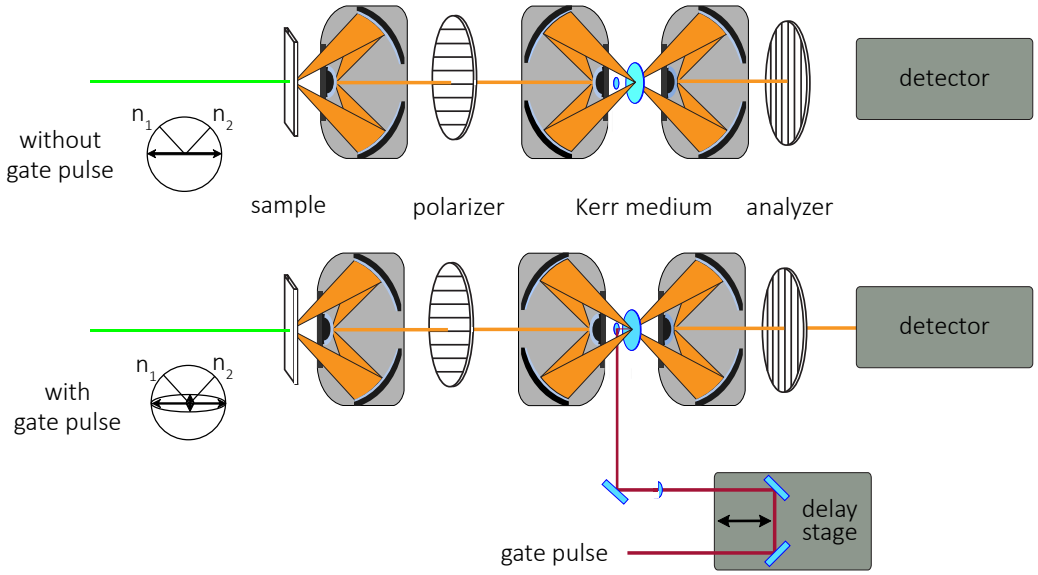

Figure 3.4: Schematic representation of the Kerr shutter principle. In the absence of the gate pulse (upper case) the fluorescence is blocked by the analyzer, while in the lower scenario anisotropy is induced in the Kerr medium by the gate pulse and fluorescence is gated to the detector.

A very important parameter of the Kerr shutter is the gating efficiency T which is the ratio between gated fluorescence and total fluorescence impinged on the Kerr shutter per time unit. The efficiency depends on the phase shifting $\phi(t)$ and on the angle Ω between the two polarization faces of fluorescence and gate pulse. The phase shifting can be expressed in the following way:[124,125]

$$\phi(t) = \left(\frac{2\pi\delta n(t)l}{\lambda_{fl}}\right) \tag{3.10}$$

while the gating efficiency can be described as in Eq. 3.11:[125,126]

$$T \sim sin^2(2\Omega) \cdot sin^2\left(\frac{1}{2}\phi(t)\right) \tag{3.11}$$

On the basis of Eq. 3.11 the gating efficiency reaches its maximum at an angle of 45° for Ω. Under the assumption of very low $\phi(t)$ the gating efficiency can be approximated by Eq. 3.12:

$$T \approx \left(\frac{\pi n_2 l I}{\lambda_{fl}}\right)^2 \tag{3.12}$$

Thus T is dependent on the square of the non-linear refractive index n_2, the path length of the Kerr medium l, the intensity of the gate pulse and the reciprocal of the squared fluorescence wavelength. However, the most crucial parameter concerning the gating efficiency is the Kerr medium itself. While the solid isotropic material fused silica exhibits gating efficiencies of few percents, about half of the fluorescence can be gated when the solvent benzene is used as Kerr medium (Section 3.2.2).

The Kerr Medium

In general, Kerr media have to be isotropic in order to diminish any $\chi^{(2)}$- effects, since those would dominate over the less efficient $\chi^{(3)}$-Kerr effect. Furthermore, the material of the Kerr medium determines the achieved time-resolution and the gating efficiency. The traditionally used carbon disulfide (CS_2) exhibits a relatively weak time-resolution of 1.32 ps. On the other hand, it is characterized by a very high gating efficiency.[127] The relatively long IRF found for CS_2 and in general for liquids is caused by an additional response of the nuclei (58%), which is not present in crystals.[128,129] Excellent time-resolutions can be achieved by the usage of optical glasses or in general solid materials. The gating efficiency increases proportionally with the dispersion and the refractive index of the respective Kerr medium.[130] However, 2PA and temporal broadening caused by the group velocity dispersion (GVD) may perturb the emission in some cases.[112]

In this work, two different types of Kerr media were used. On the one hand the solid material fused silica and on the other hand the solvent benzene. A careful choice between those has to be made, since both materials exhibit advantages and disadvantages. Particularly, fused silica is distinguished by a very fast time-resolution of ∼100 fs because its Kerr response depends only on the electronic polarizability.[112] However, fused silica as Kerr medium exhibits a relatively small gating efficiency which is typically located in the low percent range. From Eq. 3.12 it can be extracted that a higher gate pulse energy would lead to an elevated gating efficiency. Unfortunately, increased gate pulse energies entail the generation of the second and/or the third harmonic of the gate pulse which then dominate the spectrum. Hence, fluorescence would be superimposed with the much larger perturbation signals and therefore not evaluable. Consequently, increased intensities are impractical in aspiring higher gating efficiencies. Since low gating efficiencies entail rather modest signal-to-noise-ratios, a relatively stable sample is required to accumulate the fluorescence signal over several scans.

On the other hand, benzene's gating efficiency of ∼ 50% distinguishes the solvent as an outstanding Kerr medium. As high gate pulse energies would cause white light within benzene which would negatively affect the fluorescence spectrum, the power has

to be decreased to $\sim$10 µJ/pulse to reach such high efficiencies. Nevertheless, as liquid, benzene exhibits, just like CS_2, an additional nuclear response of $\sim$ 15%, yielding a worse time-resolution compared to the solid material fused silica.[131] The minimal reached IRF with benzene as Kerr medium is approximately 500 fs, while the time-resolution of fused silica would be in the range of 100 fs accentuating that it is unambiguously smaller than that of benzene. In comparison to CS_2 and fused silica, it can be deduced that benzene as Kerr medium offers the best compromise between efficiency and time resolution.[127]

4

Photoactivatable Compounds

The term photoactivatable compounds encompasses the idea of the spatial and temporal control of molecules via an external stimulus by means of light. Light as a non-invasive trigger is distinguished by its versatility, harmlessness and its ecological employment. In particular, two major classes of molecules are coined photoactivatable compounds which are on the one hand photocages and on the other hand photoswitches. The probably most crucial difference between both representatives is the reversible switching, concisely encapsulated in the term photochromism, whereas photocages undergo an irreversible process when triggered with light. Commonly, a liberation of an active site or of a bioactive molecule takes place. The following sections will give a general overview about photocages and photoswitches and introduce the systems investigated in this thesis. Detailed information concerning photocages and photochromic compounds can be found elsewhere.[45,69,71,132–138]

4.1 Introduction to Photocages

The successful application of pharmacologically active substances can be very challenging in many respects. For example, the pharmaceutical may not reach the site of action as it is degraded en route, hence modifications of the drug to improve its properties are required. Therefore, pharmacologically active substances are sometimes incorporated in a precursor substance. So called prodrugs are precursor substances which become active after metabolism. This concept is primarily aiming at improving pharmacokinetic properties of the substance e.g. the oral absorption and/or bioavailability but also at reducing the first-pass effect, or enabling a drug to pass the blood-brain barrier. Subsequently, the prodrug with negligible or no pharmacological activity can be converted

chemically and/or enzymatically into its active state at the target site.[139] Switching a molecule from its inactive to its active state can also be triggered by light and is an elegant way to face the interest of controlling biological and chemical processes. Light as trigger exhibits clear advantages such as control over the spatial and the time domain and harmlessness. Molecules which are released by a molecular framework upon irradiation are coined "caged compounds" where an effector molecule, often a biomolecule, is caged by a photoremovable protecting group (PPG, photocage or cage).

In 1962 Barltrop and Schofield introduced the very first PPG on a biologically relevant substrate in their publication "Photosensitive Protecting Groups", where glycine was liberated from benzyloxycarbonylglycine upon irradiation at 253.7 nm via a photodecarboxylation.[140] Another application to biological issues was performed by Engels and Schlaeger, who caged the second messenger 3',5'-cyclic adenosine monophosphate (cAMP) to the photolabile ortho-nitrobenzyl (*o*NB) and photolyzed the compound at 366 nm.[141] Besides nitroaryl groups arylcarbonylmethyl and coumarin-4-ylmethyl are the most prominent PPGs.

In general, the mechanism of the uncaging reaction can proceed in two ways (Figure 4.1).[69] The first and also faster mechanism encompasses a solvent-assisted S_N1-type reaction in which the effector molecule (X in Figure 4.1) is cleaved off. A PPG undergoing an uncaging reaction via this type is for example (7-dieyhtlaminocoumarin-4-yl)methyl (DEACM, Figure 4.1a)). The second mechanism includes an intramolecular rearrangement as it occurs for nitrophenyl photocages (e.g. *o*NB, Figure 4.1b)).

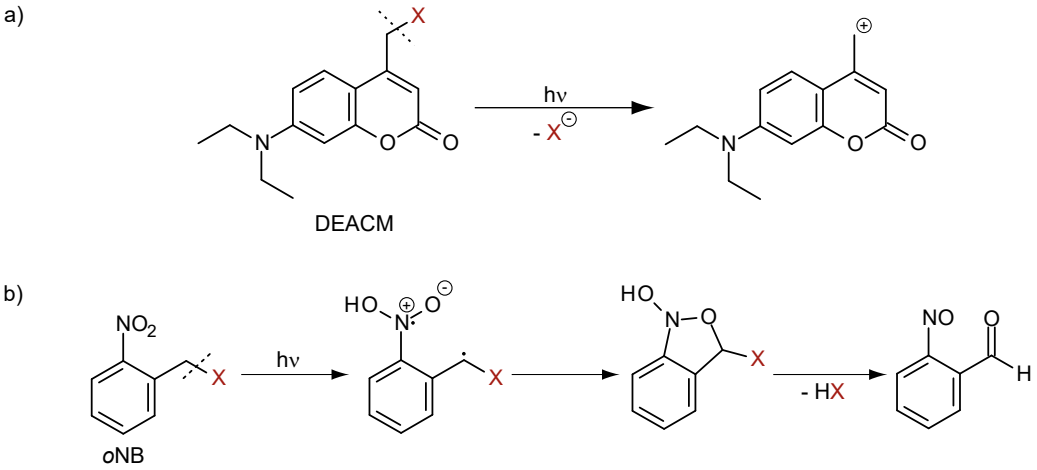

Figure 4.1: The two mechanisms of uncaging reactions. a) The faster uncaging reaction discloses a S_N1-type mechanism, as found for coumarin cages. b) The other mechanism encompasses an intramolecular rearrangement prior to the liberation of the caged compound.

Uncaging reactions are quantified by the uncaging quantum yield, which is the ratio

between the amount of released molecules and the amount of photons absorbed by the caged compound. Besides a considerable uncaging quantum yield, a large extinction coefficient of the PPG and thus the ability to collect light is desirable. However, a high extinction coefficient must not necessarily lead to a high uncaging quantum yield since diverse competing relaxation pathways such as fluorescence could deactivate the excited state. Consequently, in the design of an efficient PPG, knowledge about the photochemistry and the photophysics of the PPG are indispensable. Dependent on the field of application, the requirements which the cage has to meet and hence its properties can strongly differ. For biological concerns the caged compound should be stable under physiological conditions and exhibit high water-solubility. Contrarily, for in-cell applications the caged compound should exhibit a lipophilic character in order to diffuse through cell membranes to reach the site of action. Once, the effector molecule is photochemically released, the photoproduct of the PPG should not be harmful nor interact with the released bioactive molecule. Besides, an absorption in the phototherapeutic window is eligible. In this sense, PPG sensitized to two-photon activation is a promising approach.

4.1.1 Coumarin

Among the various types of photocages, coumarin, in particular the coumarin-4-ylmethyl, comprises most of the requirements for an excellent photocage. In general, coumarins are strong fluorophores exhibiting high photostability, which is why they where used as laser dyes in the first place.[142,143] The very first application of a (coumarin-4-yl)methyl as photocage, in detail the (7-methoxycoumarin-4-yl)methyl (MCM), was reported by Givens and Matuszewski in 1984, where upon irradiation at 360 nm, the corresponding coumarin alcohol was formed and the caged diethylphosphate was released. This was the starting shot for the application of hitherto unknown photocages.[144] Additionally, its strong fluorescent character provides an intrinsic marker for observations of reactions, making an external fluorescent probe redundant.

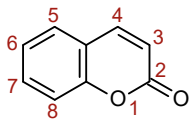

Figure 4.2: Numbering and chemical structure of coumarin which belongs to the class of benzopyrones.

The coumarin scaffold (Figure 4.2) provides many sites for versatile modifications

in order to create a photocage with desirable characteristics. Water-solubility, membrane permeability, improved quantum yields in respect to the uncaging reaction and absorbance in the long wavelength-range are some of the aimed properties. Consequently, a plethora of derivatives were established which, in general, can be subdivided into four groups: the 7-alkoxy- (e. g. MCM), 6,7-dialkoxy- (e. g. DMCM - (6,7-dimethoxycoumarin-4-yl)methyl), 6-bromo-7-alkoxy- (e. g. BhC - (6-bromo-7-hydroxycoumarin-4-yl)methyl) and 7-dialkyl-amino-substituted coumarins (e. g. DEACM).

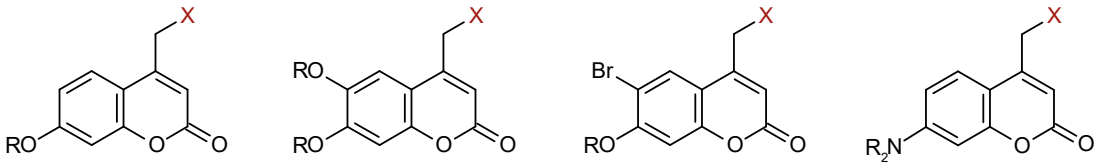

Figure 4.3: Due to the chemical structure of coumarin, plenty of different coumarin photocages were established in order to fulfill desirable characteristics.

Any of those groups include water-soluble or membrane-permeable representatives. As for the 7-alkoxy group, the (7-acetoxycoumarin-4-yl)-methyl (ACM) and the (7-propionyloxycoumarin-4-yl)methyl (PCM) derivatives are hydro- or lipophilic due to the acetyl- or the propionyl-group, respectively. Another derivative displaying high water-solubility is CMCM ((7-carboxymethoxycoumarin-4-yl)-methyl), where the carboxylic acid is ionized at a physiological pH. As depicted in Table 4.1 the different substitution patterns lead to the desired bathochromic shifts of the absorbance band.

Table 4.1: Photochemical Characteristics of the Four Groups of Coumarin Photocages.[145]

	7-alkoxy	6,7-dialkoxy	6-bromo-7-alkoxy	7-dialkylamino
λ_{max} / nm	325	345	375	395
ε_{max} / $M^{-1}cm^{-1}$	12000	12000	12000	20000
ϕ_u	~0.1	~0.1	~0.1	~0.3

ϕ_u = uncaging quantum yield

A modification to yield larger bathochromic shifts and higher quantum yields was demonstrated by Furuta *et al.* as they exploited the combination of an electron-withdrawing substituent with a heavy-atom-effect by introducing bromine at the C6 position of the coumarin scaffold resulting in BhC with a reported absorption maximum of 370 nm.[37]

A further improvement was set by introducing the diethylamino-substituent to the C7 position yielding DEACM. While the unsubstituted coumarin-4-yl-alcohol bears an absorption maximum at 310 nm, in DEACM the electron-donating diethylamino-

substituent at the C7 position leads to a bathochromic shift of about 90 nm with a molar extinction coefficient of approximately 20 000 $M^{-1}\,cm^{-1}$ at the absorption maximum. Furthermore, a slight elevated uncaging quantum yield of 0.3 was found compared to BhC. These favorable characteristics were exploited to address many biological demands.[77,146–151]

4.1.2 Photochemistry of Coumarin-4-ylmethyl

Coumarins exhibit a strong UV-absorption band which is assigned to the $S_0 \rightarrow S_1$-transition. This band of unsubstituted coumarin peaks at 313 nm and refers to a π-π^*-transition.[152,153] However, the energetically higher n-π^*-transition and the π-π^*-transition expose a certain overlap, hindering to exclusively address one of these transitions.[154,155] As in many other cases, the solvent has a decisive impact on the absorption, as shown for MCM, where the population of an excited state originates from an n-π^*-transition in aprotic solvents, whereas in protic solvents a π-π^*-transition is preferred.[154]

The photoreactivity of coumarin-4-ylmethyl can be directly inferred from the nature of the C4 atom which exhibits a relatively small electron density of the HOMO (highest occupied molecular orbital) in the ground state while the LUMO (lowest unoccupied molecular orbital) displays a rather high electron density.[152,156] Moreover, photoreactivity is supported by a charge transfer occurring from the benzylic moiety to the pyranone fragment. The so called intramolecular charge transfer (ICT) can be amplified by sophisticated substitutions at the coumarin scaffold by creating strong push-pull systems (Figure 4.4). Introducing an electron-donating, e.g. a diethylamino-unit to the C7 position, and an electron-withdrawing (EWG) substituent at the C3 position realizes such a push-pull-system. A famous example is the DEAC450.[71,157]

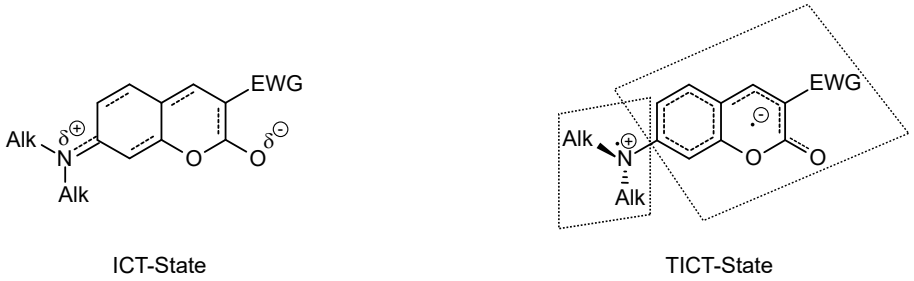

Figure 4.4: ICT- and TICT-state of dialkylamino-substituted coumarins. In the ICT-state (left) partial charges are located at the nitrogen-atom and the carbonylic oxygen via the delocalization of π-electrons. The TICT-state (right) exhibits two planes with a torsion angle of 90° and localized charges on each plane.

Besides an ICT, also a TICT (twisted intramolecular charge transfer) was found

for derivatives with such substitution patterns. Upon photoexcitation the primarily formed ICT-state with partial charge transfer character facilitates the twisting of one substituent leading to a pyramidal structure and a charge transfer is induced in the TICT-state.[158–160]

The uncaging mechanism of (coumarin-4-yl)methyl derivatives is widely-studied and well-known.[150,154,161–163] Upon photolysis the bond between the benzylic carbon and the leaving group is heterolytically cleaved forming a coumarin alcohol as a photoproduct and an anionic leaving group.

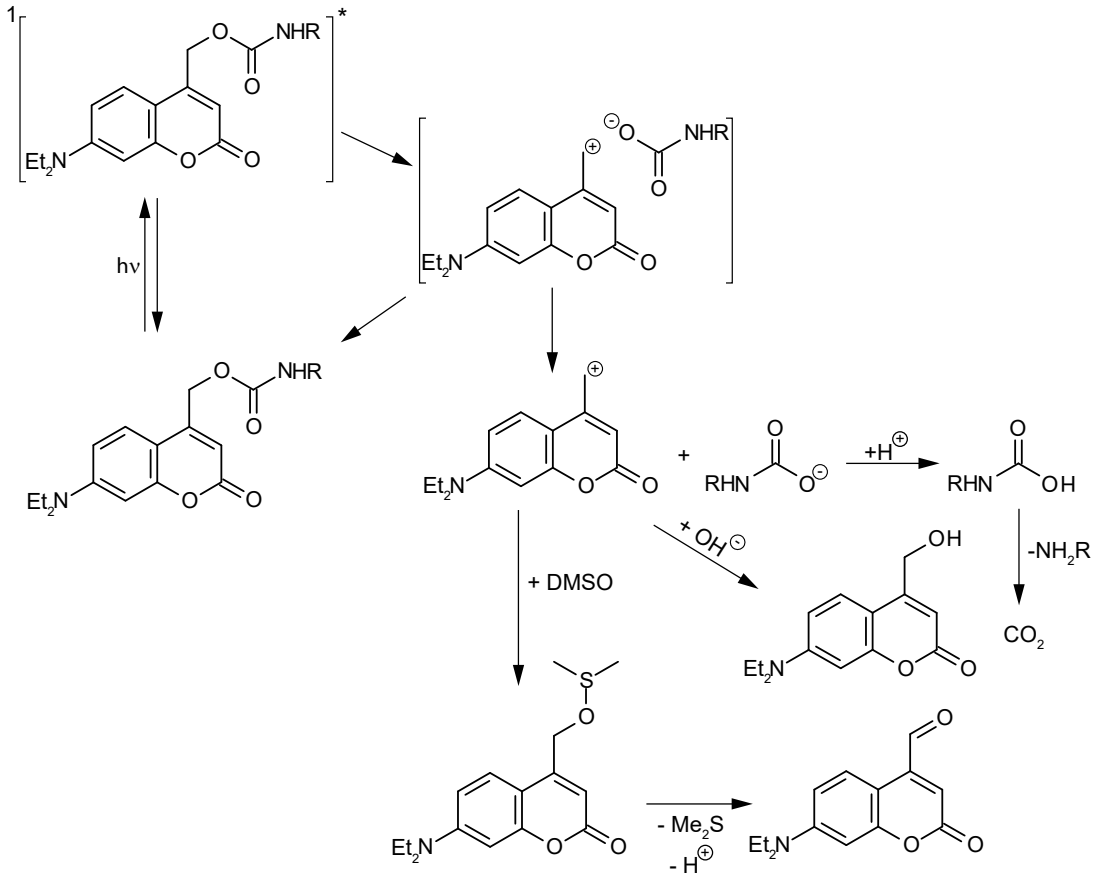

Figure 4.5: Uncaging mechanism of (coumarin-4-yl)methyl photocages in DMSO in which the leaving group R is linked via a carbamate to the coumarin moiety.

Figure 4.5 comprises the water/DMSO-assisted (dimethylsulfoxide) uncaging mechanism of DEACM which is jointed via a carbamate to the leaving group R. After photoexcitation of the DEACM, vibrational relaxation leads to the lowest excited singlet state. From there, different reaction pathways are likely to occur. The molecule can relax to the ground state either radiation-free or via emission, in particular fluorescence. The third possibility is a heterolytically bond cleavage (C-X) which forms a tight ion pair between a coumarinylmethyl cation and the later leaving group. However, in cer-

tain cases a formation of the tight ion pair is not observed.[164] The latter reaction path can split into two possibilities yielding either the repopulation of the ground state due to recombination of the ions, or a solvent-assisted step leads to the uncaging reaction. The separation of the tight ion pair leads to the nucleophilic substitution of the formed coumarinylmethyl cation with a present nucleophile which is the solvent in most scenarios. In presence of water, the carbocation and the anion are quenched yielding the corresponding coumarin alcohol and carbon dioxide originating from the photodecarboxylation reaction of the carbamate.[150,163] With DMSO as solvent/nucleophile the corresponding aldehyde and dimethylsulfide is obtained via an intermolecular proton transfer from the methylene group of coumarin to the carbamate anion. Subsequently, carbon dioxide is generated by the photodecarboxylation of the carbamate. However, smaller reaction rates were found for uncaging in anhydrous DMSO than for DMSO with a certain amount of water.[165]

At this point it shall be conceded that upon photoexcitation of the coumarin-caged compound a homolytic bond cleavage is also possible. The formed radicals consequently undergo an ISC to a triplet state.[37] However, radical photoproducts have only been reported for a heterolytic bond cleavage.[166]

4.1.3 Improvements of the DEACM Photocage

The employment of two-photon uncaging is desirable for the already mentioned reasons. However, its successful application is hindered by the lack of two-photon response of the photocage. Section 2.3 concludes different strategies to enhance the σ_{2P} of organic molecules.

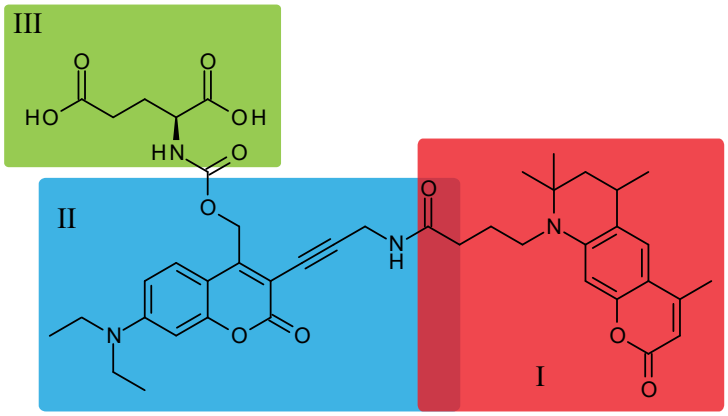

Figure 4.6: Molecular structure of the novel photocage system consisting of ATTO 390 (red, I) linked via a propargylic linker to DEACM (blue, II). Glutamate (green, III) was used as the caged biomolecule jointed via a carbamate to the photocleavable site of coumarins.

By implementing an antenna with a large σ_{2P} to the widely-used DEACM photocage, certainly a different approach was used to address this demand. As an antenna (sensitizer) molecule the commercially available ATTO 390 was chosen, which is distinguished by a larger σ_{2P} compared to the σ_{2P} of DEACM. Moreover, the large Stokes-shift of ATTO 390 causes negligible reabsorption effects and a good overlap with the absorption of DEACM derivatives, which are substituted at the C3 position, and therefore facilitating an intramolecular excitation energy transfer. Thus, the collected energy by ATTO 390 (I) is transferred to the photocage (II) which in turn shall liberate the caged glutamate (III). The biological signaling molecule glutamate (neurotransmitter), a non-essentially amino acid, is inactivated by the photosensitive protecting group DEACM. Upon illumination the covalent bond from the DEACM-moiety to the neurotransmitter is broken resulting in the release of glutamate. This novel designed photocage investigated in this work is depicted in Figure 4.6.

The detailed synthesis route of the triad can be found elsewhere, however the synthesis should be briefly outlined here.[167,168] Starting with 7-dimethyl-aminocoumarin, the DEACM alcohol was obtained in five reaction steps including a Steglich esterification with subsequent iodination.

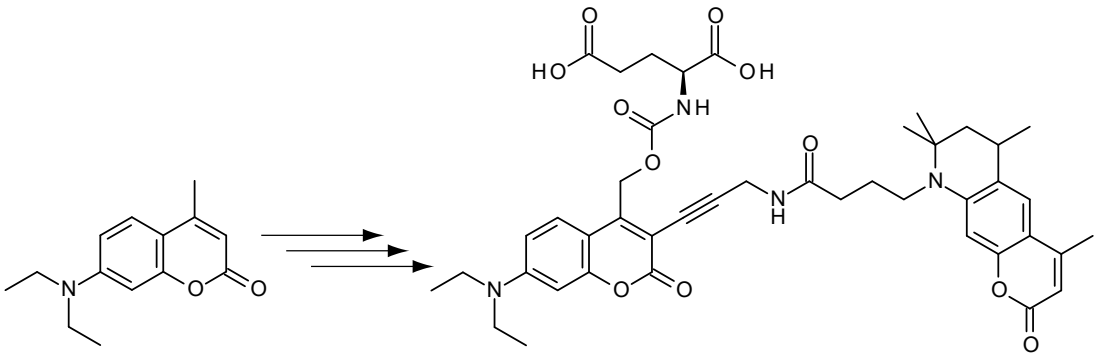

Figure 4.7: The synthesis of the triad consisting of ATTO 390, DEACM and glutamate attached via a carbamate comprises in total eleven reaction steps starting from 7-dimethyl-aminocoumarin and were performed by Andreas Jakob (Heckel group, Goethe-University Frankfurt).

The palladium- and copper(I)-catalyzed Sonogoshira-coupling was performed in order to couple the terminal alkyne of the propargylic linker with the iodized coumarin scaffold at the C3 position. The glutamate (III) was then linked as a leaving group via an active ester. After deprotection of the linker, the fluorophore antenna (ATTO 390) could be attached to it. Deprotection from the Fmoc-group of glutamate with the aid of piperidin yielded the target molecule which comprises a synthesis route consisting of eleven steps. Detailed description of the synthesis is described elsewhere.[167]

The solvent-assisted S_N1-type uncaging reaction of I+II+III results in the corresponding photoproduct (I+II), L-glutamic acid and carbon dioxide, as displayed in Figure 4.8

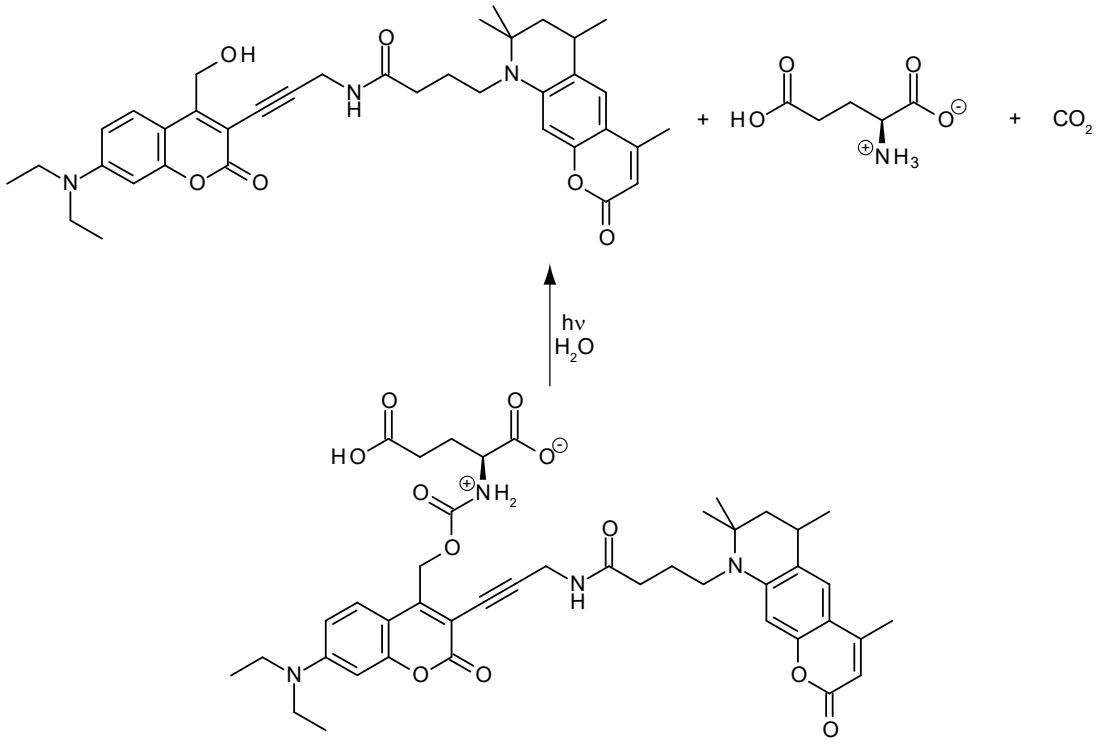

Figure 4.8: Proposed photoreaction of the triad. Irradiation yields the corresponding photoproduct (I+II), the neurotransmitter glutamate (III) and carbon dioxide.

For over 60 years the excitatory action of glutamate in the spinal cord and the mammalian brain is evident.[169] In respect to this, it is possible to detect uncaging of excitatory active glutamate within functional mapping of neurotransmitter receptors.[73] Though, detection of glutamate with the help of spectroscopic methods is aggravated, since glutamate exposes no contributions in the visible range. On the other hand, the liberation of carbon dioxide is advantageous. Due to its intense absorption in the IR-range it can be used as an intrinsic marker as it was already used elsewhere.[150,163,170] On the basis of this advantage, it is possible to monitor the process of the uncaging reaction spectroscopically.

4.2 Introduction to Photoswitches

The second class of photoactivatable molecules discussed in this thesis are photochromic compounds also known as photoswitches. The term photochromism, first introduced by Hirshberg, is distinguished by the reversible switching between at least two isomers.[171] The switching from one to the other molecular entity can be induced by UV-, visible or IR-light, while the back reaction can be initiated either photochemically or thermally. The most prominent molecules exhibiting photochromism are stilbenes, azobenzenes and spiropyranes.[135] In this work the photodynamics, in particular the ultrafast deactivation of the excited state, of the fluorophore (BODIPY) coupled to dithienylethene (DTE) and a water-soluble fulgimide were investigated.

4.2.1 Dithienylethene

Due to the excellent properties regarding photo- and thermal stability, strong resistance to fatigue and an extraordinary high quantum yield, the representative of the class of diarylethenes attracted considerable attention to the material sciences. These characteristics are exploited for example in optoelectronic devices such as storage systems, since they demand high thermal stability and an efficient write/delete procedure.[45,172–175] The photochromism of DTE is defined by a ring-closing reaction upon UV-irradiation and a ring-opening reaction after photoexcitation with visible light.

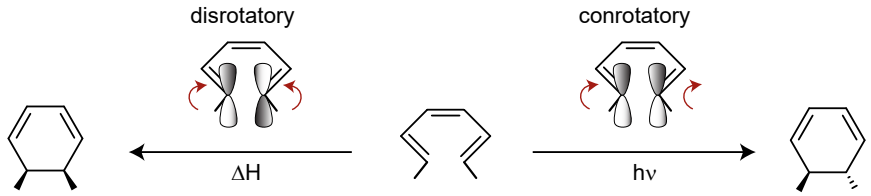

Figure 4.9: Ring-closing reaction of 1,6-dimethyl-1,3,5-hexatriene yield different isomers dependent on the excitation. A disrotatory movement of the orbitals can be achieved thermally while a photoinduced excitation would lead to a conrotatory ring-closure.

The substantial molecular motif for this cyclization is a 1,3,5-hexatriene which is formed to a 1,3-cyclohexadiene. The mechanism of this reaction on the example of 1,6-dimethyl-1,3,5-hexatriene, depicted in Figure 4.9, can be described with the linear combination of atomic orbitals (LCAO) and the Woodward-Hoffmann-rules.[176–178] The formation of the 1,3-cyclohexadiene derivative can be either initiated thermally or by light, enclosing a disrotatory or a conrotatory cyclization of the orbitals and yield different configurations, respectively.

Another approach to exploit the efficient switching between the open and the closed form is the modulation of fluorescence, where the energy from a jointed photoexcited fluorophore is transferred on the closed DTE and thus the fluorescence is quenched. If DTE is present in its open form an energy transfer is not observed but the radiative relaxation of the fluorophore.[179–181]

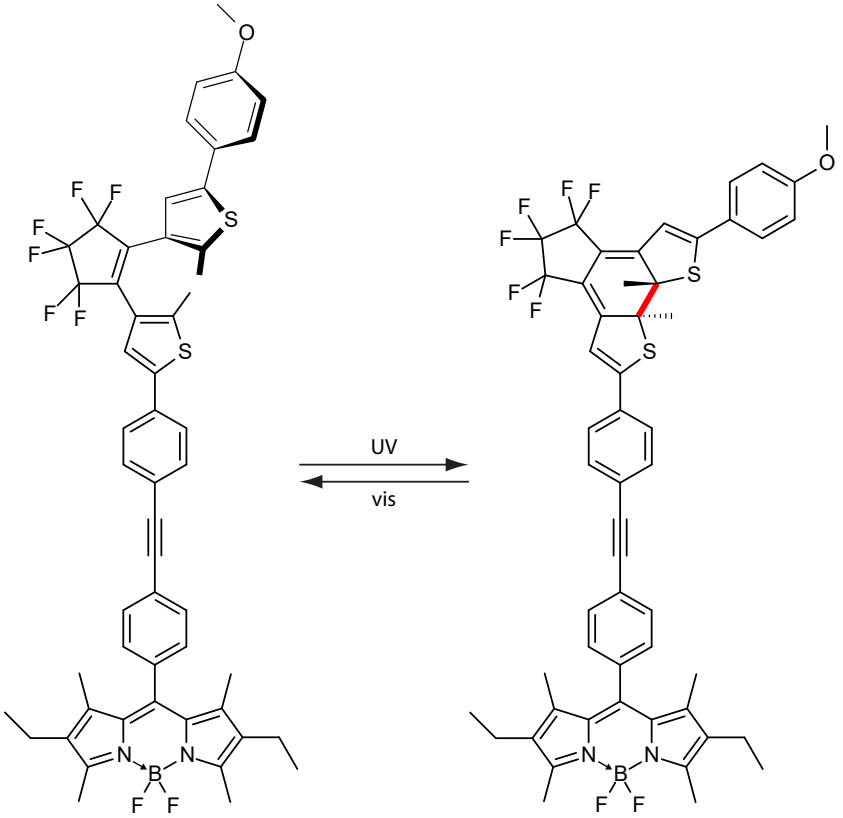

Figure 4.10: Molecular structure of the BODIPY-DTE which are linked via a phenyl-ehtinyl-phenyl-subunit. The photochromic character is derived by the DTE-photoswitch with the cleavable bond in the closed ring depicted in red.

The investigation of the modulation of such a cooperative dyad system between a fluorophore and the DTE photoswitch was part of this work. Boron-dipyrromethene (BODIPY, 4,4-difluoro-4-bora-3a,4a-diaza-s-indacene) served as fluorophore in the investigated system. It is distinguished by very sharp absorption and emission bands exhibiting a high extinction coefficient as well as a high fluorescence quantum yield. The BODIPY moiety is linked via a phenyl-ethinyl-phenyl-unit to the DTE photoswitch (Figure 4.10). The results concerning the molecular dyad can be found in Section 7.1.

4.2.2 Fulgides and Fulgimides

The other photochromic compound investigated in this work is based on the scaffold of a fulgide. Fulgides were first reported by Stobbe who found a change in color upon irradiation of the anhydrides of 1,3-butadiene-2,3-dicarboxylic acid. He introduced the name fulgide due to the intense color of the closed form (from latin *fulgere* = shine). Based on the substitution of the methylene hydrogen atoms with methyl groups, fulgides become thermally irreversible.[182] Furthermore, the photoswitch offers many sites for versatile modifications providing a tailored photoswitch for designated applications. The photochemical reactions of fulgides encompass an intramolecular rearrangement of free electron pairs as depicted in Figure 4.11, as was first reported by Santiago and Becker.[183]

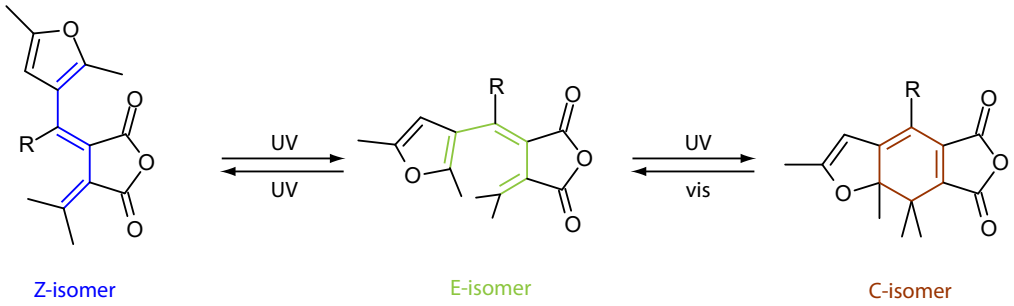

Figure 4.11: Photochromic reactions of fulgides. A ring-closing reaction to the C-isomer (right, brown) is only accessible through the E-isomer (middle, green) which is in a photochemical equilibrium with the non-cyclizable Z-isomer (left, blue).

The cyclization reaction yields the closed isomer (C-isomer) which is only accessible via the isomer where the two outer double bonds are parallel oriented to each other. In this case, it is the E-isomer (middle, green) which is in equilibrium with the non-cyclizable Z-isomer (left, blue). In analogy to DTE, the photochemical ring-opening reaction as well as the 6π-electrocyclization follows a conrotatory movement of the orbitals in the context of the Woodward-Hoffmann rules.[176–178]

However, the presence of the non-cyclizable isomer and the chemical instability caused by the hydrolysis reaction of the succinic anhydride renders a less efficient switching and confines its applications to non-aqueous media. In order to prevent the formation of the non-cyclizable isomer, and therefore to pattern a more compatible switching reaction, indolylfulgides were introduced, exhibiting a relatively bulky substituent the formation of the non-cyclizable open form can be inhibited. Furthermore, the replacement of the succinic anhydride with a succinimid ring entails an improvement of water-solubility

introducing the indolylfulgimide to a wide range of applications in aqueous environments.[184] The investigated water-soluble indolylfulgimide and its photochemical reactions are depicted in Figure 4.12.

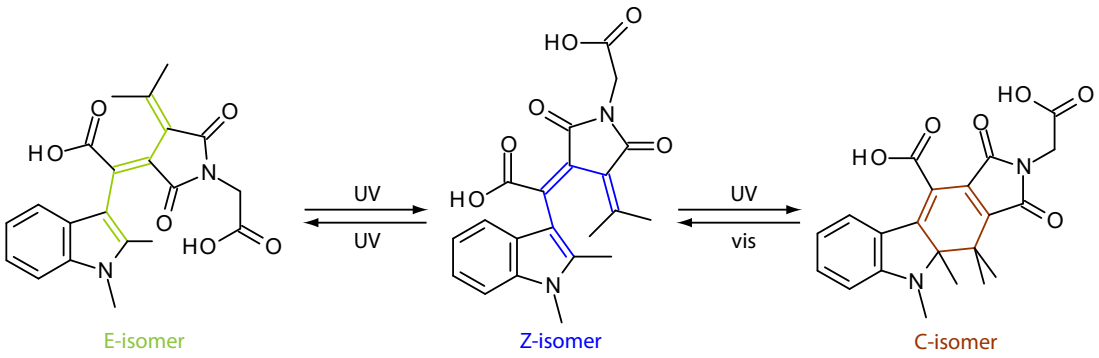

Figure 4.12: Molecular structure of the water-soluble indolylfulgimide and its photochemical reactions including three isomers. The cyclized isomer (C-isomer, brown) is only accesible through the Z-isomer (blue), while the green E-isomer is non-cyclyzable.

Due to the solubility-mediating carboxylic acid group at the inner double bond, the priority of this substituent is now higher. Therefore, the isomer which undergoes the electrocyclization reaction bears now a Z-configuration, while the E-isomer is now the non-cyclizable entity. The detailed synthesis of the water-soluble indolylfulgimide is reported in the literature.[185] The results regarding the photoswitch can be found in Section 7.2.

Part II

Experimental Procedures

5

Materials and Methods

This part outlines the experimental framework which relies on the theoretical background (Part I). The following section summarizes all materials, including solvents and compounds which were used. An explanation of the experimental procedures are provided in Section 5.2. Sample preparation for the experiments are delineated and an accurate description of the laser systems and experimental setups is provided.

5.1 Materials

Most of the molecules, which are based on the principle of the enhancement of the two-photon response of DEACM (Chapter 6), are provided by the group of Prof. Dr. A. Heckel (Goethe-University Frankfurt). Detailed information on the synthesis of this molecules can be found elsewhere.[167,168] The NHS-ester of the fluorophore antenna ATTO 390 (I) in the molecular triad (I+II+III, Figure 4.6) was directly purchased from ATTO-TEC GmbH (Siegen, Germany).

The reference compounds for TPEF measurements and the solvents in which they were dissolved are summarized in Table 5.1. The pH-value of fluorescein had to be adjusted, since its absorbance strongly depends on its protonation state. The composition of the PBS buffer which was used for experiments concerning DEACM and its derivatives is shown in Table 5.2.

The BODIPY-DTE photoswitch (Figure 4.10) was synthesized in the group of Prof. Dr. K. Rück-Braun (TU-Berlin).[181,186] The water-soluble dicarboxylic acid indolylfulgimide dissolved in 50 mM sodium phosphate buffer (pH 7.4) was synthesized in the group of Prof. Dr. W. J. Lees (Florida International University). The synthesis of the fulgimide has been published in detail.[185] *Mt*Dod:FMN and the referring buffers were

Table 5.1: Purchased Chemicals Used in this Work and Their Supplier.

reagent	supplier
Coumarin 307	Radiant Dyes Laser & Accesoires (Wermelskirchen, Germany)
Fluorescein*	Sigma-Aldrich (St. Louis, USA)
Rhodamine B	Sigma-Aldrich (St. Louis, USA)
DMSO	ACROS Organics (New Jersey, USA)
DMSO-d6	Deutero GmbH (Kastellaun, Germany)
Methanol	Fisher Chemical (New Jersey, USA)
NaOH	VWR Chemicals (Radnor, USA)

*NaOH was used to adjust the pH-value of fluorescein sodium salt to 11

Table 5.2: Composition of the Buffer Solutions Used in this Work.

	300N5M20T7.5	300N5M20A5	fulgimide buffer	PBS
pH	7.5	5.0	7.4	7.4
NaCl	300 mM	300 mM	-	140 mM
$MgCl_2$	5 mM	5 mM	-	-
Tris-HCl	20 mM	-	-	-
acetic acid	-	20 mM	-	-
KCl	-	-	-	2.7 mM
Na_2HPO_4	-	-	-	10 mM
NaH_2PO_4	-	-	10 mM	-
Na_2HPO_4 x 7 H_2O	-	-	40 mM	-

prepared in the group of Prof. Dr. M. Grininger (Goethe-University Frankfurt) and are described in 187. Phosphate buffered saline (PBS) buffer was provided by the group of Prof. Dr. A. Heckel and used for the experiments on DEACM. The composition of the buffers used in this work are shown in Table 5.2.

5.2 Methods

5.2.1 Stationary Spectrometers

Absorption Spectrometer

Absorption spectra in the UV/vis were recorded with a Specord S100 or S600 (Analytik Jena AG, Jena, Germany) using the program WinASPECT. The Specord spectrometers

are equipped with a diode array for detection. Integration time of the spectra varied between 110 and 150 ms. Samples were measured in 1x10 mm or 10x10 mm fused silica cuvettes (Starna Scientific, Ilford, UK or Hellma-Analytics, Müllheim, Germany). For illumination experiments (Section 5.2.2) cuvettes with an optical path length of either 10 mm or 4 mm were used.

FTIR Spectrometer

Information on the vibrational behavior were extracted from IR spectra recorded with a Bruker Vertex 80 (Bruker Corporation, Billerica, USA) FTIR-spectrometer (Fourier-transform infrared). Self-built cuvettes were used to record FTIR spectra. For this purpose a polytetrafluorethylene (PTFE) ring with 50 µm layer thickness was placed with PTFE paste on a CaF_2-window. The sample dissolved in deuterated DMSO (mM-range) was pipetted on the CaF_2-window and sealed with a second CaF_2-window. Within this procedure it had to be assured that the cuvette does not contain any air bubbles, otherwise strong scattering would negatively affect the IR-signals. Prior to every measurement, the chamber was purged with nitrogen to eliminate any gaseous contamination. Especially evaporated water and carbon dioxide (CO_2) generate perturbing signals in FTIR-spectra. A background spectrum was recorded before the cuvette have been placed in the chamber. To avoid any noise from residual gases, the illumination experiment was started after an additional purging time of approximately 45 min. This was checked by continuously recording "dark" spectra until the CO_2 signal disappeared. The samples were illuminated with light-emitting diodes (LEDs) (Thorlabs, Newton, USA) of different wavelengths (Table 5.3). The light of the externally mounted LED was guided through a telescope system on a mirror within the measuring chamber from where it is impinged on to the sample.

Fluorometer

For examination on the emission behavior of the investigated compounds, fluorescence spectra were recorded at a Jasco FP8500 fluorometer (Jasco Deutschland GmbH, Pfungstadt, Germany). Measurements were performed in 4x10 mm or 2x10 mm cuvettes at room temperature. The absorbance of the samples never exceeded an optical density of 0.1 ($d = 10$ mm) to diminish any inner filter or reabsorption effects.

Stationary Fluorescence requires several corrections, which shall be mentioned in the next section.

Correction of Stationary Fluorescence

Four major corrections were carried out on the obtained fluorescence data. The first correction is the baseline correction. Therefore, the lowest value or the average over a wavelength-range, where no fluorescence (F_{min}) is expected, is subtracted from the initial fluorescence spectrum F.

$$F_{korr1}(\lambda) = F(\lambda) - F_{min} \tag{5.1}$$

with $F_{korr1}(\lambda)$ as baseline-corrected fluorescence spectrum. The second correction (Eq. 5.2) considers the attenuation of the excitation beam as it travels through the sample:

$$F_{korr2}(\lambda) = \frac{F_{korr1}(\lambda)}{10^{-A(\lambda_{exc})\ .\ \frac{l_{exc}}{d}}} \tag{5.2}$$

The sensitivity of the detector is taken into account by a correction curve (D(λ)) as seen in Eq. 5.3:

$$F_{korr3}(\lambda) = \frac{F_{korr2}(\lambda)}{D(\lambda)} \tag{5.3}$$

The contribution of reabsorption has to be considered. This phenomenon occurs when only a small Stokes-shift is present, resulting in a certain overlap between absorption and fluorescence band.

$$F_{korr4}(\lambda) = \frac{F_{korr3}(\lambda)}{10^{-A(\lambda_{exc})\ .\ \frac{l_{em}}{b}}} \tag{5.4}$$

with $F_{korr4}(\lambda)$ as the final corrected fluorescence.

Determination of Fluorescence Quantum Yields

The strength of a fluorophore is characterized by the fluorescence quantum yield ϕ_{fl} which is defined as the ratio between the number of emitted and absorbed photons (Eq. 5.5):[98]

$$\phi_{fl} = \frac{n_{fl}}{n_{abs}} \tag{5.5}$$

ϕ_{fl} can also be expressed as ratio between the rate of fluorescence to the rates of all other deactivation channels (Eq. 5.6). It reflects the probability that an excited state will be deactivated by fluorescence instead of another process. e.g. ISC, IC and vibrational relaxation:

$$\phi_{fl} = \frac{k_{fl}}{k_{ISC} + k_{IC} + k_{vr} + ...} \tag{5.6}$$

Determination of fluorescence quantum yields can either be performed on an absolute or a relative method. While only the latter requires specific knowledge about instrumental parameters, the comparative method turned out to be one of the most reliable

Table 5.3: Peak Wavelengths and Bandwidths of LEDs Used for Uncaging Experiments in this Work.

peak wavelength / nm	365	385	405	420	455	470
bandwidth (FWHM) / nm	7.5	10	20	12	18	25

approaches to determine fluorescence quantum yields.[188] However, this method requires a reference sample with a known ϕ_{fl} in order to refer the integrated emission intensities with the sample of unknown ϕ_{fl}.[189] The method demands samples with low concentrations to diminish any reabsorption or inner filter effects. By measurements of several fluorescence intensities with reasonable sample concentrations and a subsequent extrapolation to OD 0, errors caused by reabsorption and internal reflections within the cell can be eliminated. Furthermore, the method suffers from polarization effects and the influence of varying optical densities. If different solvents are used for the reference and the investigated samples, refractive indexes of the solvents should be included. Most of these error sources necessitate corrections which may entail a reduced accuracy of the determined value.

$$\phi_{fl,x} = \phi_{fl,ref} \left(\frac{m_x}{m_{ref}} \right) \left(\frac{\eta_x^2}{\eta_{ref}^2} \right) \tag{5.7}$$

Fluorescence quantum yields can also be determined by using an integrating sphere, which is also known as Ulbricht sphere named after Friedrich Ulbricht. As an absolute method it does not necessitate any reference samples and therefore overcomes problems entailed by polarization and refractive index changes.[189,190]

5.2.2 Illumination Experiments

Uncaging reactions were induced by continuous illumination with LEDs (Thorlabs, Newton, USA) with various excitation wavelengths and monitored with an UV/vis or a FTIR-spectrometer. LEDs were connected to a hub and controlled by a driver (DC4100, Thorlabs). The LED was either mounted on the sample cell holder or the LED-light was directed onto the sample through a fiber after it has been focused with a telescope system. In both cases the cuvette was placed in a Peltier-cooled cell holder to ensure a constant temperature, and a stirring bar was added to maintain a homogeneous sample.

5.3 Laser Spectroscopy

In this work several experimental setups, hence different laser sources were used. This section firstly introduces the laser systems and secondly gives a general overview of

non-linear optical processes occurring in the setups.

5.3.1 Clark MXR CPA

The laser system used in transient absorption experiments is a Clark-MXR CPA-2110 (Clark-MXR Inc., Dexter, USA) based on the chirped pulse amplification (CPA) principle for which Mourou and Strickland were honored with the Nobel Prize in physics in 2018 and is discussed in detail in Section 5.3.3.[191,192] The laser consists of an oscillator/amplifier system. "Pump" energy for the lasing process of the mode-locked Er^{3+}-doped fiber oscillator is continuously supplied by 980 nm pulses of a laser diode. Generated pulses at a central wavelength of 1550 nm are frequency-doubled by a PPLN crystal ($LiNbO_3$) providing laser pulses at 775 nm) which are used to seed the active medium in the amplifier. The latter is pumped by a neodymium-doped yttrium-aluminum-garnet (Nd:YAG) laser (532 nm) creating a population inversion which amplifies the seed pulses. The Nd:YAG laser is pumped by an arc lamp. The mode locking is realized by self-phase modulation and cross-phase modulation, which are third-order non-linear optical effects.[193] Amplified pulses with a fundamental wavelength of 775 nm, a repetition rate of 1 kHz, a pulse length of 100 fs and a pulse energy of approximately 1 mJ are decoupled.

5.3.2 Tsunami

Three Tsunami lasers (Spectra-Physics, Darmstadt, Germany) were used in this work. One served as seed laser for the Spitfire Pro F system (Spectra-Physics, Darmstadt, Germany), the other provided laser pulses in TPEF measurements (Section 5.5.2) and the third was used in TSCPC experiments. A Millennia (Spectra-Physics, Darmstadt, Germany) cw-laser (continuous wave) with a neodymium-doped yttrium vanadate (Nd:YVO_4) gain medium continuously pumps the active solid-state titanium-doped sapphire (Ti:Sa) laser medium of the mode-locked Tsunami with a wavelength of 532 nm.[194,195] The absorption of Ti:Sa peaks in the 500 nm range enabling the efficient photoexcitation of the crystalline material with green light of the a Nd:YVO_4-laser. Due to the broad emission band with a maximum located at roughly 800 nm of the Ti:Sa material, the Tsunami laser exhibits a broad tunable operation range in the NIR from 730 to 930 nm. With additional arrangements even a range from 690 to 1080 nm is amenable.

5.3.3 Spitfire Ace Laser System

Two different Spitfire laser systems were used to run the Kerr shutter setup. The Spitfire Ace 120-F (amplifier laser, Spectra-Physics, Darmstadt, Germany) is seeded by a Ti:Sa-laser (MaiTai SP, Spectra-Physics, Darmstadt, Germany) with a repetition rate of 40 MHz and a tunable output from 780 - 820 nm. The Ti:Sa-crystal of the regenerative amplifier Spitfire is pumped by a neodymium-doped yttrium lithium fluoride (Nd:YLF) Empower 45 laser (Spectra-Physics, Darmstadt, Germany) (527 nm). The Spitfire Ace 120-F exploits the CPA-principle allowing to work with amplified pulses without damaging any optics or the Ti:Sa material within the amplifier laser. Figure 5.1 shows the three compartments of the Spitfire Ace (stretcher, amplifier and compressor) necessary for CPA. Firstly, the seed pulse provided by the MaiTai laser enters the stretcher in order to temporally broaden the pulse before it is amplified in the crystal. Recompression of the amplified pulses leads to short high-output pulses. In the following the CPA principle shall be illustrated.

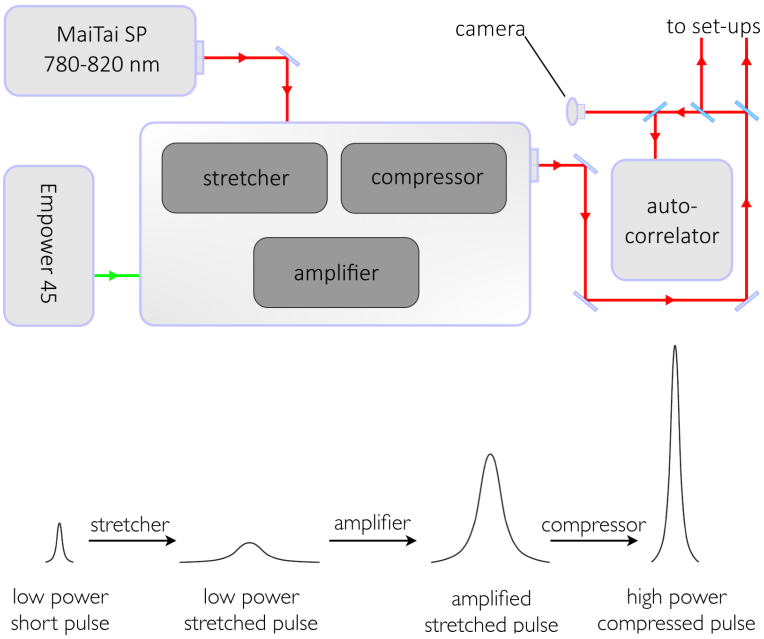

Figure 5.1: Schematic representation of the Spitfire Ace laser system enclosing the seed laser MaiTai SP, the pump laser Empower 45 and the regenerative amplifier Spitfire Ace 120-F which works on the CPA-principle in order to stretch the seed pulse before it will be amplified and then leaving the compressor yielding a high power compressed output.[196] A self-built autocorrelator and two cameras (one camera is not shown) monitor the pulse width and the beam profile, respectively.

At first, the seed pulse provided by the MaiTai passes through a Faraday isolator (FI) in order to protect the optics of the MaiTai laser by severe back reflections. The

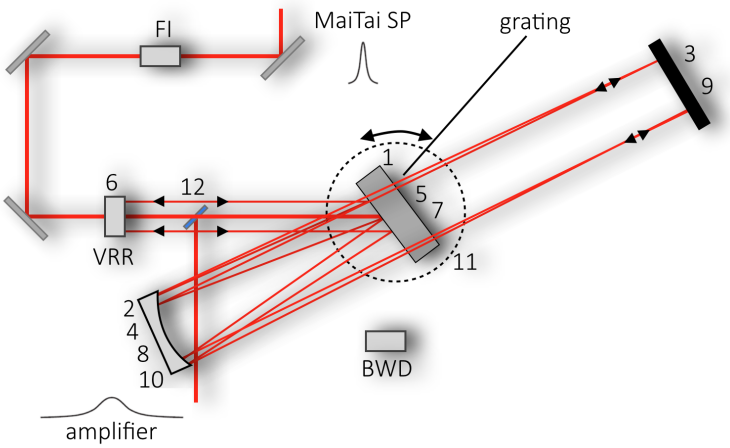

Figure 5.2: Schematic representation of the stretcher in order to prevent damage of optics by amplified pulses. The stretcher enclosed in the Spitfire is conceived in a way that only one grating is used to minimize adjustments.

pulse is broadened by introducing a positive chirp where longer wavelengths take a shorter beam path than blue parts. In general, prisms or gratings can be used for this purpose. In particular, the Spitfire Ace uses a single grating for creating positively chirped pulses on which the beam is impinged (1) before traveling through the slit of the vertical retroreflector (VRR). Subsequently, the temporally broadened pulse is routed to a concave mirror (2) which is slightly facing upwards in order to send the broadened pulse over the grating to the end mirror (3). From there the pulse is directed back to the concave mirror (4) which reflects it again to the grating (5). The further stretched pulse is now incident on the lower mirror of the vertical retroreflector (6) from where it is stepped upwards in order to retrace the same path in the stretcher (7-11). By this, the longer wavelengths have to travel a shorter path introducing an even further positive chirp to the pulse. Before exiting the stretcher compartment to the amplifier by the pick-off mirror (12) the beam is focused back into a Gaussian-shaped pulse. A band width detector (BWD) consisting of two photodiodes senses reflections of the broadened pulse. If no light is incident on the photodiodes, the internal shutter of the Spitfire Ace closes automatically to prevent damages.

Pulses from the stretcher are vertically polarized by the polarization rotating periscope (PS) and are changed in height but not in polarization by a second periscope (PPS). The pulse is now incident at the extra-cavity Pockels cell (PC1). Depending on its state, one of four cases concerning the polarization will happen. In case of a turned-off Pockels cell the polarization experiences no change. The vertically polarized pulse is then reflected away from the cavity by the polarizer. The same applies, when the Pockels cell is switched on and the timing is 180° out of phase, which is defined by the

TDG (time delay generator). A low amplification can be achieved when PC1 is on and the timing is set such that two pulses enter the cavity. However, they will be vertically polarized within the cavity and are not capable of exiting the amplifier by the polarizer. The forth case describes the basis of a successful amplification where PC1 is on and the timing allows one pulse to enter the cavity hence the horizontally polarized pulse is transmitted by the polarizer and will remain in the amplifier cavity. Now, one of three different cases can occur depending on the state of the intra-cavity PC (PC2).

The first cases describe the PC2's state off allowing the pulse to transmit without any polarization change. It is then rotated 45° by passing through the $\frac{1}{4}$ waveplate ($\frac{\lambda}{4}$). It is then reflected back and incident on the $\frac{\lambda}{4}$ causing a vertical polarization due to a rotation of another 45°. Since the polarizer reflects vertically polarized pulses it is sent to the Ti:Sa crystal where the pulse experiences first gain as it passes through the crystal. Routed by the following mirrors it is reflected back through the crystal to the $\frac{\lambda}{4}$ which the pulse has to pass two times yielding horizontal polarization, hence the pulse exits the cavity as it transmits through the polarizer.

When the PC in the cavity is turned on, the upcoming pulse is rotated 45°. Another 45° are added to polarization as it is directed to the $\frac{\lambda}{4}$. Subsequently, it is reflected back to the $\frac{\lambda}{4}$ and the polarizer yielding the initial polarization causing the beam to leave the cavity through the polarizer without any amplification.

The third case comprises the description of a successful amplification, where PC2 is off and then turned on. The pulse enters the cavity through PC2 leaving its polarization unchanged since it is turned off. It is then vertically polarized after passing two times through $\frac{\lambda}{4}$ forcing the pulse to the direction to the Ti:Sa crystal where it picks up first-pass gain. In the meanwhile, PC2 is turned on, causing the pulse to rotate 180° everytime it travels back and forth through PC2 and $\frac{\lambda}{4}$. Consequently, the polarization of the pulse remains unchanged and gets amplified as it is incident on the crystal. The maximum amplification of the pulse is reached as it passed 12-15 times the Ti:Sa crystal. The TDG sets the precise timing to turn off the PC2, thus the pulse rotates 45° as it passes $\frac{\lambda}{4}$ and another 45° as it is reflected back through $\frac{\lambda}{4}$. The vertical polarization of the pulse allows now the pulse to exit the cavity as it impinges on the polarizer. As stated above the Ti:Sa crystal is pumped at 527 nm by the Empower 45 pump laser. Its pulses are vertically polarized as they pass through the polarization rotator and then focused on the crystal. Green light which is not absorbed by the Ti:Sa crystal transmits through the intra-cavity mirror, while red light is reflected. A curved mirror reflects back the green light for further absorption by the crystal.

Stretched high-power pulses are routed from the amplifier to the compressor in order

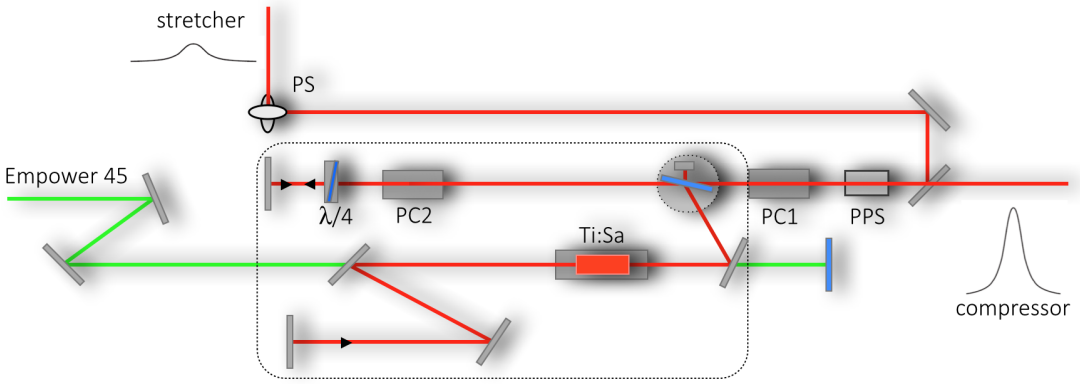

Figure 5.3: Schematic representation of the amplifier used in the Spitfire. It comprises a Ti:Sa crystal as laser medium which is pumped by the green light of an Empower, two periscopes (PS and PPS), two Pockels-cells (PC1 and PC2) and a $\frac{\lambda}{4}$-waveplate.

to obtain a short amplified laser pulse. The positive chirp introduced in the stretcher must be compensated again. The shorter wavelengths now have to take a shorter path than the longer wavelengths and thus can catch up with them again (negative chirp). Therefore, the amplified pulse is directed over several mirrors (1) on to the right side of a grating (2) where it is reflected on a horizontal retroreflector (HRR, 3-4) which flips it back to the grating (5). The pulse is now incident on the left side of the grating and sent to the bottom part of a vertical retroreflector (VRR, 6). From the top mirror, the pulse is routed back now to the lower left of the grating (7) where it starts to refocus again. Afterwards the pulse is again incident on the horizontal retroreflector (8-9) which directs the beam to the grating (10) and the compressed pulse is able to leave the laser (11).

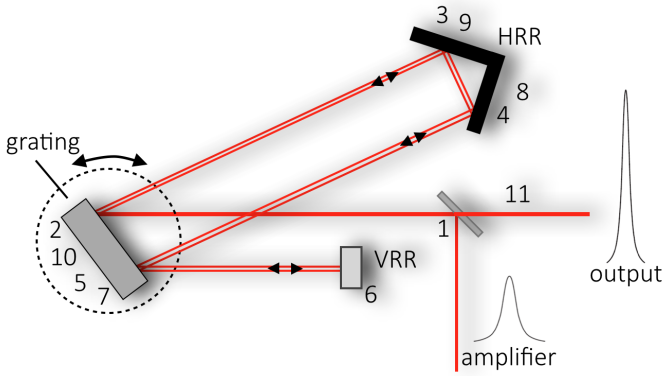

Figure 5.4: Schematic representation of the compressor in the Spitfire laser. Like in the stretcher only one grating is implemented in order to compress the pulse.

Table 5.4: Lasers Used in this Work.

Laser	active medium	wavelength	rep. rate	purpose
Millennia Pro	Nd:YVO_4	532 nm	cw	pump source
Tsunami	Ti:Sa	730-930 nm	80 MHz	seed source & TPEF
Spitfire Pro	Ti:Sa	730-930 nm	1 kHz	synchronization experiment
Empower 45	Nd:YLF	527 nm	1 kHz	pump source
MaiTai	Ti:Sa	780-820 nm	40 MHz	seed source
Spitfire Ace	Ti:Sa	780-820 nm	1 kHz	Kerr-shutter
CPA2110	Ti:Sa	775 nm	1 kHz	ATAS*

*ATAS = advanced transient absorption spectrometer

5.4 Non-linear Optical Processes

Any of the presented time-resolved measurements in the third part of this thesis exploit non-linear optical processes (Eq. 3.5). The theoretical description of those are out of scope of this work, instead it shall be referred to other theses.[123,197–199] However, in this section the most important processes are shortly delineated.

In order to excite specific transitions in a molecule, it is necessary to tune the excitation wavelength of the laser pulses. For this purpose various frequency conversion techniques are used. In addition to the non-collinear optical parametric amplifier (NOPA, Section 5.4.1), this can be achieved by sum frequency generation (SFG, Section 5.4.3) or frequency doubling (second harmonic generation, SHG Section 5.4.4).

5.4.1 NOPA

Due to the usage of a NOPA it is possible to set any wavelength in the visible and infrared spectral range by focusing a broadband white light pulse (seed) and a frequency-doubled laser pulse (pump) in a BBO-crystal. In the case of temporal and spatial overlap a new wave is created within the crystal. Due to the requirement of momentum and energy conservation, the pump photon is converted into a high-energy signal and a low-energy idler photon. The frequency of the signal photon results from the energy conservation which is the difference between the frequencies of pump and idler photon.

The parametric amplification requires phase matching of the three waves which can be achieved by varying the angle between signal and idler photon. If the spatial and temporal overlap of the pulses is given, the desired wavelength can be selected by delaying the seed pulse and by the tilt angle of the BBO crystal.

5.4.2 OPA

A self-built two-stage OPA (optical parametric amplifier) was used for the generation of the gate pulse for time-resolved fluorescence measurements. Similar to the NOPA, a white light is generated as seed pulse. In this scenario only the red part of the white light is used as seed pulse by using a filter (KG 650) which is superimposed with the fundamental in a BBO-crystal. Contrarily to the NOPA, both pulses are collinearly aligned in front and behind the crystal collinear aligned to each other which gives access to near-infrared (NIR) pulses. The generated pulse with a central wavelength of 1300 nm is reflected back to the BBO-crystal via a retroreflector where it is superimposed for a second time with the fundamental (2^{nd} stage).

5.4.3 Sum Frequency Generation

SFG is a second-order non-linear optical process. It can be generated in a non-linear crystal in which two laser beams generate a third beam with the sum of the frequencies of the two incoming beams (Eq. 3.3). The generation of excitation pulses below 470 nm is possible with this technique, which is not accessible via the NOPA process. However, a NOPA is necessary to generate one of the two initial beams in the SFG.

5.4.4 Second Harmonic Generation

Frequency doubling is a special case of the SFG and is therefore a non-linear optical process of second order. In contrast to SFG, two laser pulses of the same wavelength are required to generate the frequency doubling, where an excitation pulse with half the wavelength of the incoming pulse in the BBO-crystal is generated. For a laser pulse with a central wavelength of 775 nm, this means a frequency doubling to a wavelength of 388 nm.

5.4.5 Pulse Compression

Non-linear optical processes require plenty of optics. As light travels through them, a positive GVD, hence a temporal broadening is introduced. In order to obtain high time-resolutions, the pulse can be routed through a grating (Figure 5.4) or a prism compressor which is used in the Advanced Transient Absorption Spectrometer (ATAS), where an overall negative chirp is generated to compensate the positive chirp occurring in the complete beam path.

5.4.6 White Light

The non-linear third order processes self-focusing and self-phase modulation are necessary for white light generation. Self-focusing describes the phenomenon that laser beams diverge or focus within a medium resulting in a modification of its refractive index, leading to further focusing of the pulse and hence a further amplification. The self-phase modulation provides a temporal compression of pulses and a generation of a supercontinuum which corresponds to a spectral broadening.

White light is used as seed pulse for the NOPA (Section 5.4.1) or the OPA (Section 5.4.2) process or in pump-probe spectroscopy in order to probe the state of the photoexcited molecule. To obtain a corresponding "response", light, which covers the entire UV/vis range, is used. For this purpose, the laser fundamental is sent through a transparent medium, typically sapphire, calcium fluoride or YAG crystals, which results in different spectral broadenings of the pulses.[200]

5.5 Experimental Setups

5.5.1 Transient Absorption Spectroscopy

Processes at the atomic as well as the molecular level, such as bond formation or fission, take place on an ultrashort time scale. Conventional methods are insufficient to gain insight into these crucial processes. Pump-probe spectroscopy proves to be a tool for observing processes on such time scales. A schematic representation of a corresponding instrumental setup (ATAS) which was used in this work is shown in Figure 5.5. The photosensitive system is initially photoexcited by a narrow-band laser pulse to an electronically excited state. After a variable time interval, a second spectrally broad laser pulse induces then further transitions.

Laser pulses for transient absorption measurements were provided by the Clark-MXR CPA-2110 (Section 5.3.1). The laser supplies pulses with a central wavelength of 775 nm, which are divided by a beam splitter into the pump and the probe pulse. The excitation pulse is delayed by a variable delay line (M-531.DD, Physik Instrumente, Karlsruhe, Deutschland) relative to the probe pulse. Thus signals of the occurring processes can be observed as a function of the delay time. The pump-probe setup is equipped with a delay line with a path length difference of 1 µm up to 30 cm enabling the measurement of photodynamics up to 2 ns within the experiment. The lower limit of the time-resolution for the experiment is confined by the pulse length. NOPA, SHG or SFG were applied for the wavelength conversion of the excitation pulse. Sapphire and calcium fluoride

(CaF_2) crystals were used in order to generate white light. CaF_2 exhibits a wide spectral range, however, the crystal does not withstand high laser intensities like sapphire. Consequently, the crystal must be moved continuously which may lead to a reduced stability of the generated white light, hence to higher noise in the data. The probe pulses were recorded with a spectrometer and an electronic acquisition system with a spectral resolution of 6.7 nm or 4 nm depending on the grating. The detection unit consists of a 64-channel photodiode array (PDA), a signal processing chip (S8865-64, Hamamatsu Photonics, Hamamatsu, Japan), a driver circuit (C9118, Hamamatsu Photonics, Hamamatsu, Japan) and a data acquisition card (NI-6110, National Instruments, Austin, USA) digitizing the analog PDA-signals with 12 bits.

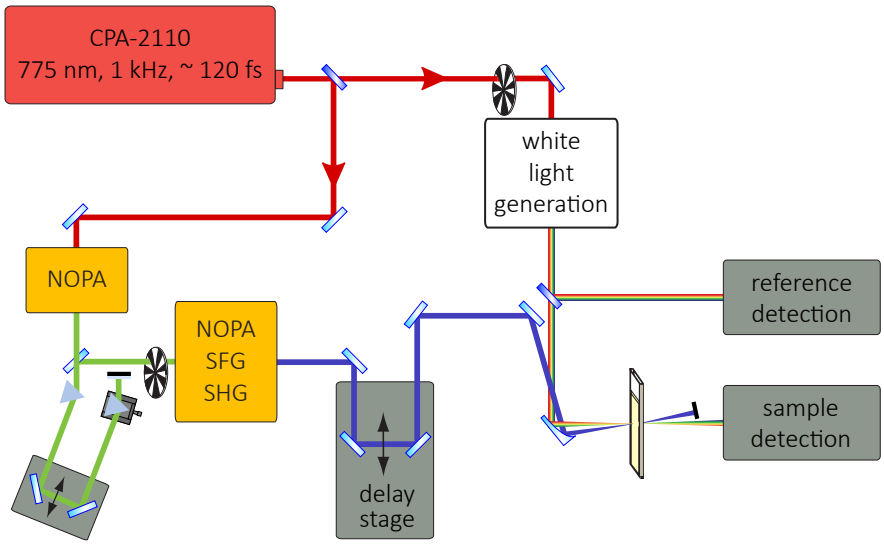

Figure 5.5: Schematic representation of the pump-probe setup used in this work.

The result of the transient absorption measurements are wavelength-dependent absorption difference spectra which are obtained from the logarithm of the relation between the intensities of non-excited $I(\lambda)_{non}$ and excited sample $I(\lambda)_{exc}$ (Eq. 5.8):

$$\Delta A(\lambda) = log\left(\frac{I(\lambda)_{non}}{I(\lambda)_{exc}}\right) \tag{5.8}$$

For a better signal-to-noise-ratio, the white light is detected separately (I_{ref}), in order to consider its fluctuations and therefore subtracted from the signal (I_{sig}) and taken into account in Eq. 5.9:

$$\begin{aligned}\Delta A(\lambda) &= log\left(\frac{I(\lambda)_{sig,non}}{I(\lambda)_{sig,exc}}\right) - log\left(\frac{I(\lambda)_{ref,non}}{I(\lambda)_{ref,exc}}\right) \\ &= log\left(\frac{I(\lambda)_{sig,non}\cdot I(\lambda)_{ref,exc}}{I(\lambda)_{sig,exc}\cdot I(\lambda)_{ref,non}}\right)\end{aligned} \tag{5.9}$$

Chopper wheels are placed in the beam path of the pump and the probe pulse to detect the different intensities. The chopping scheme is shown in Figure 5.6.

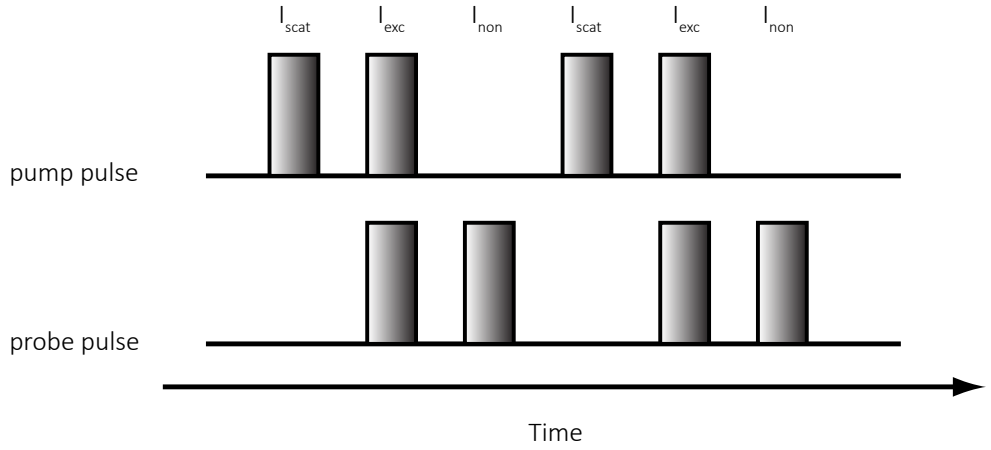

Figure 5.6: Chopping scheme used in the ATAS setup. Pulses which are not shown are blocked by the chopper wheel.

In case of a chopped probe pulse and a detected pump pulse, scattered light from the excitation pulse (I_{scat}) can be assessed and is considered in Eq. 5.10:

$$\Delta A(\lambda) = log\left(\frac{I(\lambda)_{ref,exc} - I(\lambda)_{ref,scat}}{I(\lambda)_{sig,exc} - I(\lambda)_{sig,scat}} \cdot \frac{I(\lambda)_{sig,non}}{I(\lambda)_{ref,non}}\right) \tag{5.10}$$

This approach yields negative and positive difference signals. The most common difference signals are the result of ground state bleach (GSB), excited state absorption (ESA) and stimulated emission (SE) and which are schematically visualized in Figure 5.7. The GSB origins from the fact that the pump pulse excites about 5% of the molecules into an electronic excited state. The subsequent probe pulse than induces the same transition, but less molecules are now in the ground state leading to an attenuation of this process.

As the initial excitation pulse transfers the molecules into an electronically excited state, it facilitates further absorptions into higher electronic states by the probe pulse which is called ESA resulting in new positive difference signals. SE occurs when the probe pulse offers an energy which matches the transition energy between the first excited and the ground state, it is therefore an induced emission with two coherent photons resulting in a negative signal, since now more light is detected. The positioning of the GSB and the SE can be derived by the stationary absorption and the fluorescence band, respectively.

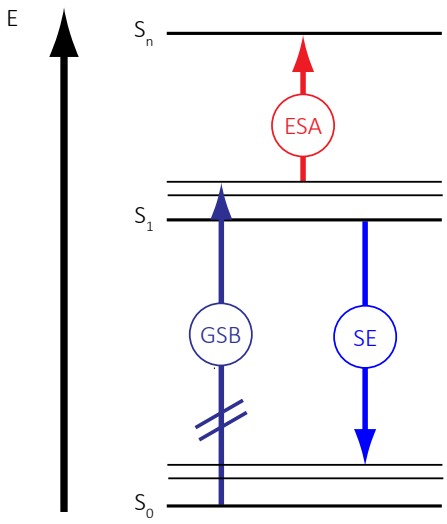

Figure 5.7: Schematic representation of the most common signals detected in transient absorption spectroscopy.

Data Evaluation

In order to assign the detected signals to specific processes, a global lifetime analysis (GLA) was performed with the OPTIMUS software.[201] Prior to this, a correct interpretation of the above mentioned difference signals requires the compensation of the GVD caused by the probe pulse by using a second- or third-order polynomial. Additionally, the detected signal is a convolution of the molecular response and the IRF. The first can be approximated in a sum-of-exponentials function with lifetimes (τ_j) over the whole detected spectrum by means of the GLA. In respect to varying absorbance changes throughout the spectrum, the time constants are weighted with wavelength-dependent amplitudes A_j. The IRF has to be solved by iterative reconvolution which is concisely shown in Eq. 5.11:[201]

$$S(t, \lambda_{exc}, \lambda_i) = \sum_{j=1}^{n} A_j(\tau_j, \lambda_{exc}, \lambda_i) \cdot exp\left(\frac{-t}{\tau_j}\right) \otimes IRF(t) \tag{5.11}$$

For further information, reference is made to Slavov *et al.*[201] The obtained amplitudes are represented in decay associated spectra (DAS) where the amplitudes of the corresponding time constants are plotted against the wavelength.

5.5.2 Two-photon Excited Fluorescence

The determination of σ_{TPA} (Section 2.4) was derived from fluorescence measurements after two-photon excitation. TPEF-experiments were carried out by using the wavelength-tunable Tsunami laser (Section 5.3.2). A schematic representation of the setup for measuring TPEF is displayed in Figure 5.8. The Tsunami laser is equipped with a four-prism sequence configuration in which the pulse is spatially dispersed. The desired excitation wavelength is obtained by varying the width of the slit between the two inner prisms which also determines the output bandwidth and therefore the pulse duration. This can result into long pulses which has to be corrected by moving the prisms in order to obtain the shortest pulse width.

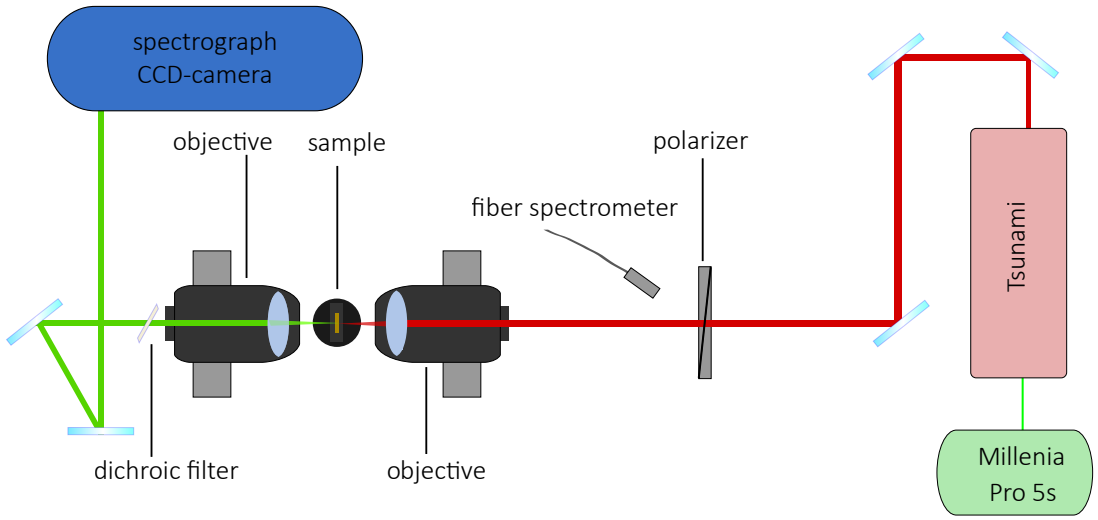

Figure 5.8: Schematic representation of the TPEF setup used in this work for the determination of σ_{TPA}. The laser pulse of a wavelength-tunable laser is focused with an objective on the sample and generated fluorescence is subsequently collected with a second objective and guided to the detector. A dichroic filter blocks the intense excitation light.

The laser output enters a prism compressor introducing a negative chirp to the pulse, so that a later introduced positive chirp can be compensated. Directly after the polarizer which is used to adjust the pulse, a fiber spectrometer is mounted to monitor the spectral pulse shape. Subsequently, the laser pulse is focused with the aid of a microscope objective (Plan N, 20/0.40, Olympus, Tokyo, Japan) on the sample which is placed in an 1x10 mm cuvette. The generated fluorescence upon two-photon excitation is collected with a second objective (UPlanFL N, 20x/0.50, Olympus, Tokyo, Japan) and routed to the detector. Both microscopes were mounted on linear translation stages enabling them to move in each dimension. A short-pass dichroic mirror (FF670-SDi01, Semrock, Rochester, USA) and a band-pass filter (BG38, Schott, Jena, Germany) were placed

after the second objective to diminish any perturbation signals. The fluorescence was routed via two mirrors into the spectrograph (SpectraPro 300i, Acton Research, Munich, Germany) equipped with a CCD-camera (charge-coupled device, 400 Pixel x 1340 Pixel, Roper Scientific, Munich, Germany). The signals were monitored in the computer program WinSpec (Roper Scientific, Munich, Germany). The sample concentration was roughly 100 µM, the integration time was set to 500 ms and 10-20 scans were recorded for each measurement. The power was set to 500 mW for the most excitation wavelengths and controlled prior and after measurement. A pulse intensity of 500 mW was not reached for excitation wavelengths at the edges of the tunable range. However, the reference compound and the sample with unknown σ_{TPA} were measured at identical pulse intensities, according to Eq. 2.15 the power than can be neglected.

5.5.3 Time-correlated Single Photon Counting

Measurements of fluorescence lifetimes in the ns-range were determined with a TCSPC-setup. Laser pulses are provided by a wavelength-tunable Tsunami laser equipped with a frequency doubler and a pulse picker (Model 3980, Spectra-Physics, Darmstadt, Germany). The laser output is split, where the fundamental is detected by a fast photodiode (TDA 200, PicoQuant GmbH, Berlin, Germany) setting the start signal for the measurement, while the frequency-doubled pulse is used as excitation pulse which travels through a filter (BG40, Schott, Jena, Germany) in order to diminish residual light of the fundamental. Excitation light is focused on the sample which is placed in a 4x10 mm cuvette (Starna Scientific, Ilford, UK). Generated fluorescence is detected by a photomultiplier tube and sets the stop signal (PMA-C 182-M; TimeHarp 260 PicoQuant GmbH, Berlin, Germany). Further information can be found elsewhere.[197]

5.5.4 Kerr Shutter

The laser pulse used in the Kerr shutter setup is provided by a Spitfire laser system. Measurements on the water-soluble fulgimide (Section 7.2) and the functional BODIPY-DTE dyad (Section 7.1) were performed with a Spitfire system emitting pulses with a central wavelength of 775 nm at a frequency of 1 kHz with an output energy of around 1.1 mJ per pulse with a laser pulse width of about 130 fs. Further information on this setup can be found elsewhere.[123] During this doctoral thesis the Kerr shutter setup was moved and a new Spitfire Ace laser system was installed Section 5.3.3.

With a repetition rate of 1 kHz the new laser system emits with a central wavelength of 800 nm and a laser pulse width of about 120 fs and a pulse energy of 6 mJ. About 1 mJ is used for the Kerr shutter setup which is schematically represented in Figure 5.9.

The setup encapsulates two "arms" for the generation of the gate and excitation pulse. First of all, the diameter of the Spitfire Ace laser is reduced with a telescope to an appropriate size for the optics within the Kerr shutter setup and subsequently split for the prevailing wavelength conversions. The reflected part ($\sim 60\%$) is used to seed a two-stage OPA providing the IR gate pulse, whereas the transmitted laser pulse is either used to generate a SHG by focusing the laser fundamental in a BBO-crystal or for an one-stage NOPA (Section 5.4) generating excitation pulses in the wavelength range from 470 – 700 nm.

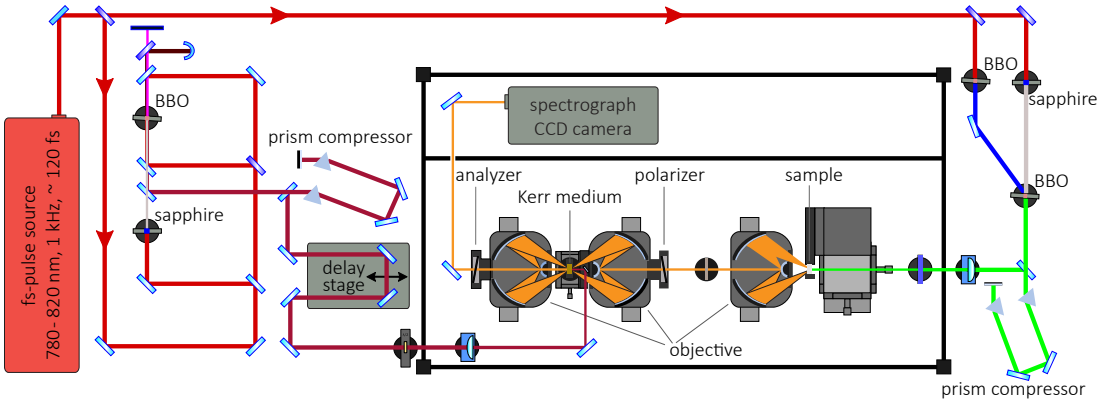

Figure 5.9: Schematic representation of the Kerr shutter setup to detect time-resolved fluorescence on an ultrafast time scale.

The gate pulse can be tuned in its central wavelength between 1150 – 1350 nm in the two-stage OPA, whereby the gate pulse generated in the current Kerr shutter setup exhibits a central wavelength at 1300 nm. Besides using the IR pulse for gating, also the direct use of the laser fundamental (780 – 820 nm) without any wavelength conversions can be used as gate pulse. Since no wavelengths have to be converted, the direct use of the laser fundamental as gate pulse can be seen as advantageous. However, the intense signal of the laser fundamental dominates the obtained spectra, although notch filters were used to minimize the intensity of the fundamental. Moreover, it is advisable to use wavelengths in the IR as gate pulses, as they do not affect the spectral range where fluorescence typically is expected. On the other hand, IR gate pulses with high intensities will cause their 2^{nd} and/or their 3^{rd} harmonic which will negatively influence the fluorescence. For example, the used IR gate pulse at 1300 nm, if intense enough, would produce higher harmonic generations at 650 nm and at 433 nm which will significantly perturb the fluorescence spectrum.

Subsequently, the gate pulse is directed to a prism compressor. After compression, the pulse travels through an electronic delay line (M-531.DD, Physik Instrumente, Karlsruhe, Deutschland) which enables the possibility to monitor the decay of the fluores-

cence at several delay times. As the thin film polarizers allow only an extinction ratio between $10^{-3} - 10^{-4}$, causing relatively large background, time scales up to hundreds of picoseconds are common.[112,114,118] This problem could be solved by the usage of thin Glan polarizer.[202,203] After leaving the delay line the gate pulse is incident on a $\frac{\lambda}{2}$ changing its initial polarization before the gate pulse is focused on the Kerr medium.

The transmitted laser fundamental from the very first beam splitter in Figure 5.9 is used to generate the excitation pulse. After wavelength conversion and compression, the excitation pulse is focused on the sample in a flow-through cuvette made of fused silica (d=500 µm, 130.199-QS, Hellma-Analytics, Müllheim, Germany). The investigated sample is circularly pumped from a reservoir (typically an Eppendorf tube) via PTFE tubes (d=800 µm) to the cuvette. Due to this arrangement a minimum sample volume of ∼500 µL is required.

The generated fluorescence will be subsequently collected via a Schwarzschild-objective (5002-000, Beck Optronic Solutions, Brighton, UK) which directs the collimated fluorescence through a wire-grid polarizer with fused silica as substrate (PFU04C, d = 700 µm, Moxtek, Orem, USA) which is distinguished by a transmission of 82% over a spectral window from 450 – 700 nm. The parallel polarized fluorescence is now incident on a second Schwarzschild-objective which focuses the fluorescence on the Kerr medium, either benzene (anhydrous, >99.8%, Sigma-Aldrich, St. Louis, USA) in a cuvette (d = 1 mm) or fused silica (Suprasil, d = 1 mm, Hereaeus, Hanau, Germany). As no gate pulse is applied, the fluorescence will be gathered by the third objective and reflected by the analyzer with a vertical orientation regarding to the first polarizer. If the gate pulse is focused on the Kerr medium via a silver mirror with a diameter of 4 mm, which is mounted after the second objective, a change in polarization of the fluorescence occurs and is capable to transmit through the analyzer while the gate pulse is blocked by the backside of the third objective.

After passing through the analyzer the fluorescence is directed via two silver mirrors and a lens into the spectrograph (SpectraPro 2358, Acton Research, Munich, Germany). Inside of the spectrograph the fluorescence is guided on one of the pre-mounted gratings with a blazing of 300 nm, 500 nm or 800 nm. In this work only the grating with a blazing of 500 nm was used to detect time-resolved fluorescence. Afterwards, the emission will be detected via a nitrogen-cooled back-sided illuminated CCD camera (400 Pixel x 1340 Pixel, Spec-10:400B/LN, Princeton Instruments, Trenton, USA). Time-resolved fluorescence data are acquired with the aid of a LabView-based program which drives several electronics including the delay stage, the spectrograph and the CCD camera. A detailed description of the measurement program is described elsewhere.[123]

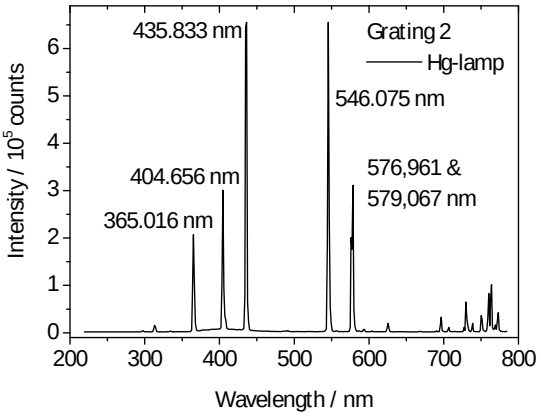

Figure 5.10: Mercury lamp spectrum detected with grating 2 with a 500 nm blazing in order to calibrate the spectrograph.

Correction of Time-resolved Fluorescence

Similar to stationary fluorescence, time-resolved fluorescence spectra have to undergo several corrections as well. The sensitivity of the detection is taken into account by multiplying the fluorescence with a correction curve obtained with the radiation of a tungsten-halogen lamp (63358, LOT-Oriel, Darmstadt, Germany) and a provided calibration curve. The resulting correction curve is depicted in Figure 5.11.

The reabsorption correction is performed in the same way as described in Section 5.2.1 by which the fluorescence is divided by the half of the transmission assuming that fluorescence is generated in the middle of the cuvette after photoexcitation. Furthermore, Eq. 3.12 reveals the dependence of the gating efficiency on λ^2 which is considered by multiplying the time-resolved fluorescence accordingly with λ^2. Moreover, the impact of the GVD on the fluorescence has to be corrected. Hence, the beam path through the materials and their wavelength-dependent refractive indexes had to be determined. Therefore, the Sellmeier equation was consulted (Eq. 5.12) and its first derivative was formed according to the wavelength for the calculation of the group velocity.[204]

$$n^2(\lambda) = 1 + \sum_{i=1}^{n} \frac{\lambda^2 \cdot A_i}{\lambda^2 - B_i} \tag{5.12}$$

with A and B as material-specific constants.

The total beam path causing GVD encompasses 0.25 mm of the used solvent and under the assumption that the fluorescence is generated in the middle of the cuvette, 1.95 mm of fused silica in account of the sample cuvette and the wire-grid polarizer. The last value depends on the used Kerr medium. In case of benzene, 1 mm fused silica of the cuvette and another 0.5 mm benzene had to be considered. When fused silica was used as Kerr medium only 0.5 mm had to be added to the path.

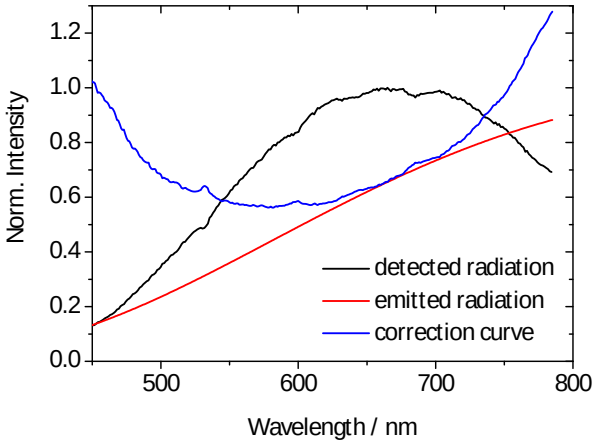

Figure 5.11: Correction curve (blue line) obtained by the spectrum of a halogen lamp (black line) divided by the provided calibration curve (red line) in order to consider the sensitivity of the detector. The correction curve has to be multiplied with the uncorrected fluorescence. The correction curve comprises the spectral correction for the Kerr shutter setup with benzene as Kerr medium and the grating 2 with a blaze wavelength of 500 nm.

Subsequently, the delay time at the excitation wavelength is set to zero and the amount of the materials will be added. The next step is to apply the delay times to all wavelength channels where every channel gets an individual time-axis. In the end, all channels will be interpolated to a mutual time-axis.

A last correction is necessary when filters were used to diminish any perturbation signals, most-commonly in the excitation beam. Thus the fluorescence is divided by the transmission of the used filters.

Part III

Results

6

Sensitized Two-Photon Cages

The results shown in this chapter refer to the improvement of coumarin-based photocages (Section 4.1.3). In particular, the aim was to enhance the two-photon absorption of a widely-used cage. Due to the favorable properties of coumarin-4-yl cages, DEACM was used as the backbone (Section 4.1.2). The characterization of glutamate caged by DEACM (DEACM-Glu) and the corresponding photoproduct DEACM-OH, which serve as model systems, are shown in the following section. Spectroscopic investigations on ATTO 390, the other moiety of the triad, are presented in Section 6.2, while the characterization on the novel system consisting of ATTO 390, DEACM and glutamate is shown in Section 6.3. The last section of this chapter briefly summarizes and discusses the presented results.

6.1 DEACM-Glu

6.1.1 Stationary UV/vis Characterization

To investigate the spectral properties of the newly designed cage consisting of ATTO 390 and DEACM, stationary UV/vis absorption spectra were recorded and compared with the individual fragments of the dyad. DEACM-Glu and DEACM-OH (Figure 6.1) dissolved in DMSO both exhibit major absorption bands with maxima at 378 nm and 375 nm and are therefore about 75 nm red-shifted compared to unsubstituted coumarin (Figure 6.2).

Both absorption bands are assigned to a π-π^*-transition.[152,153] Furthermore, a higher energy absorption band is visible if DEACM-Glu or DEACM-OH are dissolved in PBS-buffer (Figure 6.3). This short-wavelength absorption band results most probably from

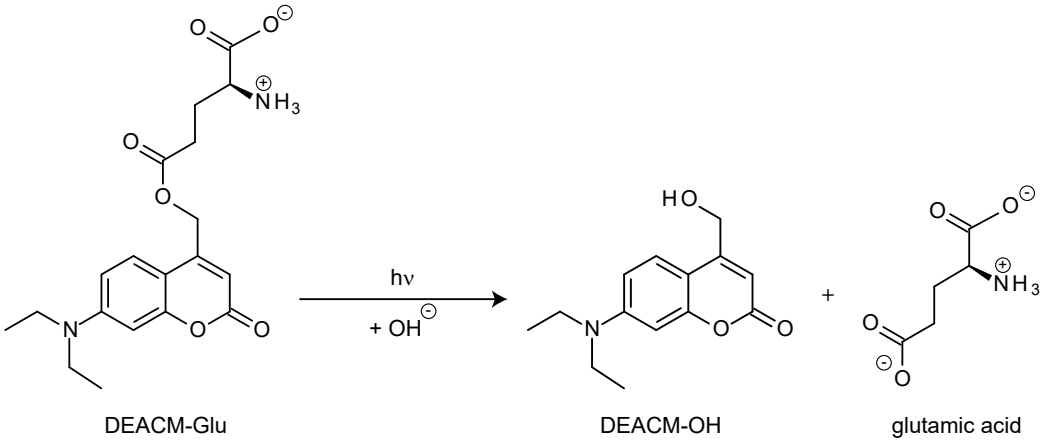

Figure 6.1: Proposed uncaging reaction of DEACM-Glu. The solvent-assisted reaction yield DEACM-OH and glutamic acid.

a π-π^*-transition from the HOMO-1 to the LUMO as the symmetry-forbidden n-π^*-transitions are characterized by very low ε, although they are found in the UV region of the spectrum.[152,205] Since DMSO shows strong absorption in the UV range, higher energy absorption bands are not visible in DMSO. Due to the carboxylate-units of glutamate, DEACM-Glu shows modest solubility in PBS-buffer, while DEACM-OH is poorly soluble in aqueous buffer solutions.

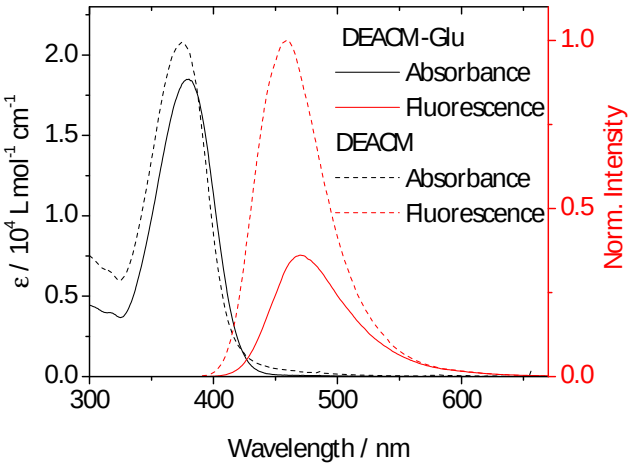

Figure 6.2: UV/vis absorption spectra of DEACM-Glu (black line) and of the corresponding photoproduct DEACM-OH (dashed black line) in DMSO; Fluorescence spectra of DEACM-Glu (red line) and DEACM-OH (dashed red line) in DMSO.

The absorption band of DEACM-OH dissolved in DMSO experiences a bathochromic shift of about 10 nm compared to DEACM-OH dissolved in PBS-buffer, while the shape of the absorption band is independent of the solvent.

The linkage of glutamate to DEACM leads to no major changes in the spectral shape

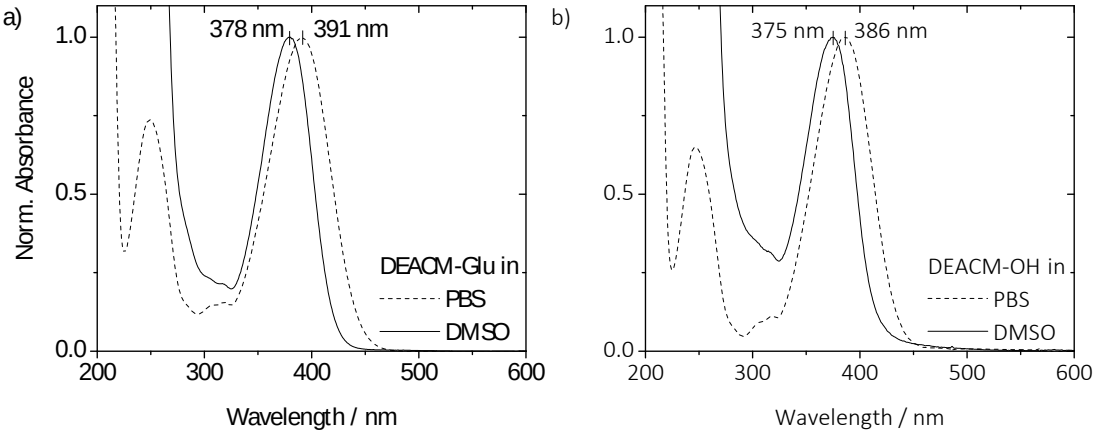

Figure 6.3: Normalized steady-state absorption of (a) DEACM-Glu and (b) DEACM-OH in DMSO (solid line) and in PBS-buffer (pH = 7.4) (dashed line). The absorption spectra of the compounds dissolved in PBS reveal a higher energy absorbance band, which cannot be observed in the spectra of the samples dissolved in DMSO, due to its absorbance.

of the absorption but is about 5 nm bathochromically shifted compared to DEACM-OH. Furthermore, a higher extinction coefficient of DEACM-OH was found compared to DEACM-Glu. Again, the main absorption band is assigned to the π-π^*-transition. Intriguingly, solvent effects as well as the process of uncaging lead to bathochromic shifts (Figure 6.3).

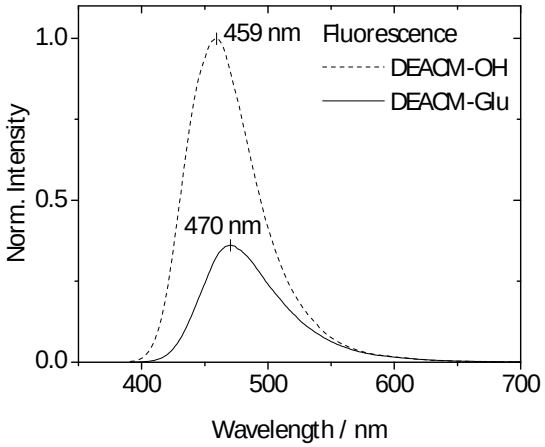

Figure 6.4: Fluorescence bands of DEACM-Glu (black line) and DEACM-OH (dashed black line) dissolved in DMSO show a quenched fluorescence intensity for the caged compound compared to the corresponding photoproduct DEACM-OH.

Additionally, emission properties of DEACM-OH and DEACM-Glu have been examined. Normalized fluorescence of DEACM-OH and the according fluorescence of DEACM-Glu are shown in 6.4, revealing a quenched intensity of DEACM-Glu compared

to DEACM-OH. The Stokes-shift of DEACM-OH is about 75 nm yielding in an emission maximum at 459 nm, while the emission maximum of DEACM-Glu is at 470 nm and therefore exhibits a Stokes-shift of about 90 nm. Furthermore, the fluorescence shape of DEACM-Glu seems to differ in comparison to DEACM-OH, which might be due to intramolecular interactions caused by the glutamate moiety and the diethylamino-unit. Typically, the caged compound DEACM-Glu reveals a lower FQY (0.32 ± 0.03) than DEACM-OH (0.85 ± 0.09) This is in line with other caged compounds and their corresponding photoproducts.

6.1.2 Uncaging Experiments

Uncaging experiments were carried out by continuous illumination of DEACM-Glu dissolved in PBS-buffer at 385 nm (Figure 6.5). An absorption change is already seen at early times upon irradiation, where the absorption continuously shifts hypsochromically. Isosbestic points are clearly visible for both absorption bands, indicating a photoinduced reaction. The hypsochromic shift can be denoted to the formation of DEACM-OH. Nonetheless, the absorption decreases, although it should increase during uncaging based on the single component absorption spectrum. This leads to the assumption that the compound experiences a photodegradation upon illumination.

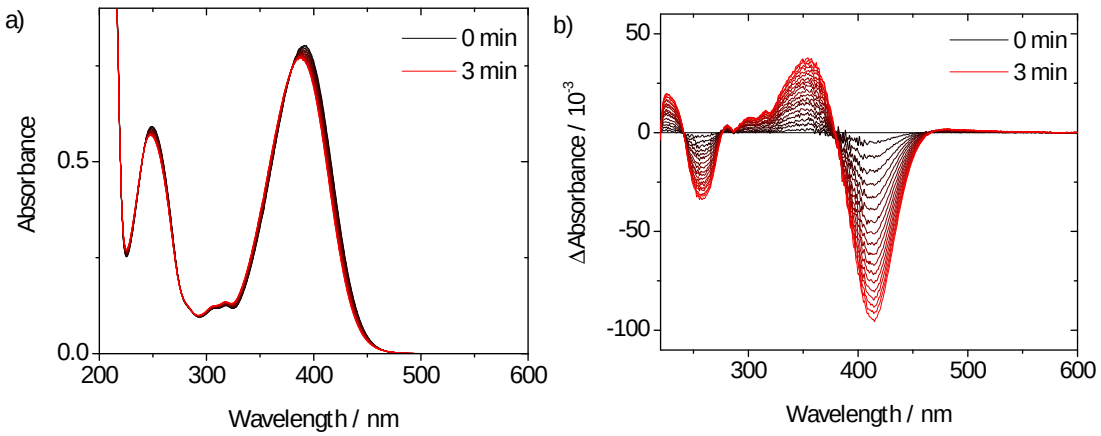

Figure 6.5: a) Absorption spectra of DEACM-Glu in PBS-buffer (0 min - 3 min) recorded during continuous illumination ($\lambda = 385$ nm). The resulting difference spectra during continuous illumination of DEACM-Glu in PBS-buffer are shown in b).

Longer illumination times lead to new evolving isosbestic points at 363 nm and at 438 nm and to the formation of an absorbance above 450 nm which could be explained by further degradation of the investigated sample as seen in Figure 6.6.

The same experiment was conducted with DEACM-Glu in DMSO (Figure 6.7).

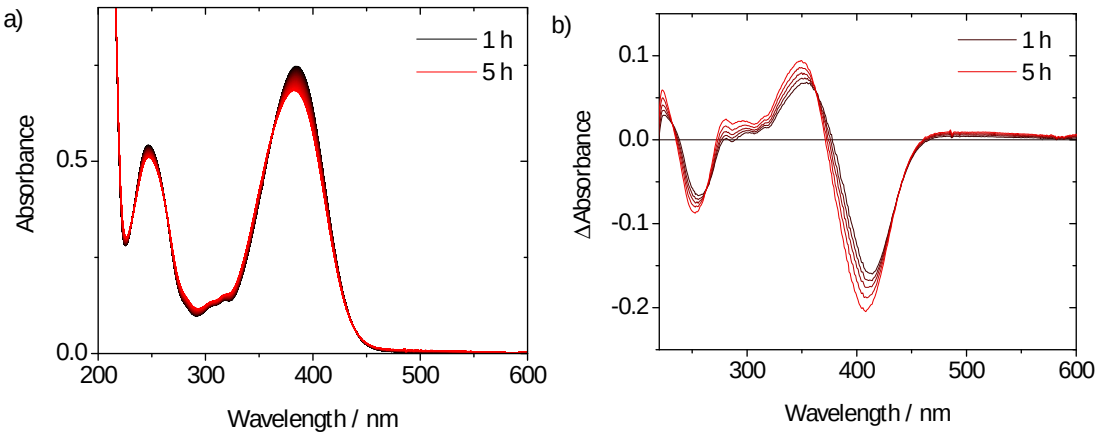

Figure 6.6: Absorption spectra of DEACM-Glu in PBS-buffer from 1 h-5 h recorded during continuous illumination (λ = 385 nm). The resulting difference spectra during continuous illumination of DEACM-Glu in PBS-buffer are shown in b).

Again, clear absorption changes are visible, indicated by two isosbestic points at 340 nm and at 420 nm. The absorption band decreases and shifts to higher energies upon photoexcitation at $\lambda = 385$ nm. Intriguingly, the hypsochromic shift and the absorption above 450 nm are even more pronounced than in the case of DEACM-Glu in PBS-buffer. Furthermore, the wavelengths of the isosbestic points do not change over the entire time of the experiment, suggesting a less complex reaction in comparison to the longtime-illumination experiment of DEACM-Glu in PBS-buffer (Figure 6.5 and Figure 6.7).

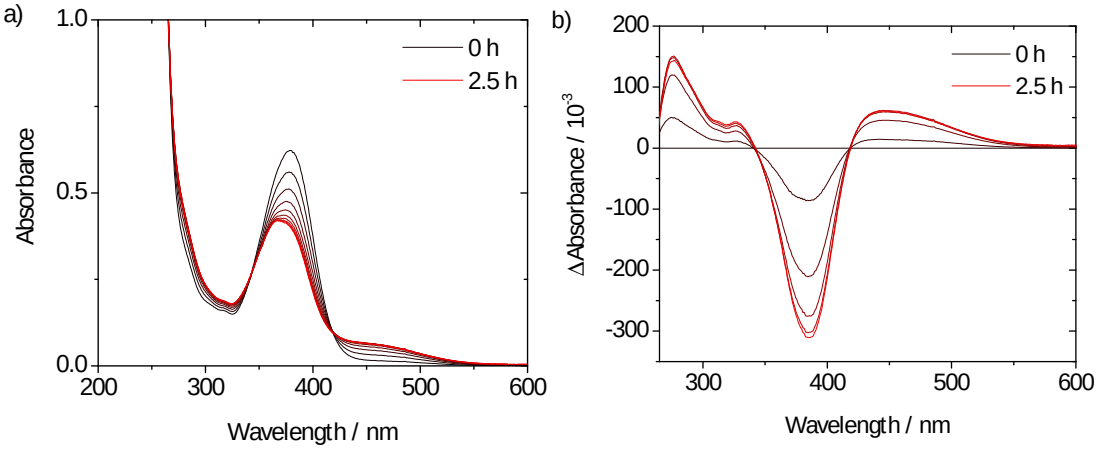

Figure 6.7: Absorption spectra of DEACM-Glu in DMSO from 0 h - 2.5 h recorded during continuous illumination (λ = 385 nm) in the UV/vis range. The resulting difference spectra during continuous illumination of DEACM-Glu in PBS-buffer are shown in b).

The origin of the evolving absorption in the red is ambiguous. Assignments of this absorption band to DEACM-aldehyde after photoexcitation of DEACM compounds were reported in the literature.[164,206] The reaction mechanism seems unlikely. A DMSO-assisted reaction mechanism as depicted in Figure 4.5 is more likely to occur. Another possibility would be an aggregation of coumarin scaffolds (π-stacking). This is supported by the lack of hydrogen bonds in DMSO. A third possibility could be a DEACM dimer obtained by the reaction of a cationic coumarinmethyl molecule with the DEACM alcohol. Longtime-illumination experiments in the UV/vis reveal complex solvent-dependent photodynamics of DEACM-Glu. However, due to a missing characteristic change in UV/vis absorption caused by glutamate, a clear evidence of uncaging, could not be extracted from UV/vis absorption measurements.

6.1.3 Transient Absorption Spectroscopy

UV/vis-pump-vis-probe experiments were carried out to examine the ultrafast photodynamics of DEACM-Glu in different solvent-mixtures to study the influence of protic polar solvents. Ultrafast measurements of the corresponding photoproduct DEACM-OH can be found elsewhere.[150,163] Transient absorbance changes were detected after photoexcitation close to the absorption maximum of DEACM-Glu at 388 nm, by generation of the second harmonic of the laser fundamental (Section 5.4.4). The probe pulses were generated by focusing the laser fundamental into a CaF_2 crystal, resulting in white light covering a spectral range from 375 nm to 675 nm (Section 5.4.6).

Figure 6.8 shows the transient absorption spectrum of DEACM-Glu in pure DMSO, while Figure 6.9 displays the ultrafast photodynamics of DEACM-Glu in a DMSO-PBS-mixture (4:1). At first glance, high similarity between both spectra is evident. However, a closer look reveals significant differences caused by the solvent. Both experiments lead to four prominent signals, which decay very slowly, so that signal amplitudes at the maximum delay time are still visible. Two negative signals (shown in blue) can be identified below 400 nm and at 450 nm to 550 nm. The first negative signal (>400 nm) can be assigned to the GSB of DEACM-Glu, reflecting the missing absorption from the ground state to the first electronically excited state. However, the GSB exhibits only a small noisy signal which is caused by the strong overlap with the positive signal above 400 nm and due to the photoexcitation of the pump pulse at 388 nm. The second negative band (450 nm - 550 nm) refers to the stimulated emission (SE) occurring from the S_1-state to the ground state. Two positive signals are located above 550 nm and centered at 425 nm. Both positive absorbance changes describe a population of an higher electronically excited state caused by absorption from the S_1-state (ESA).

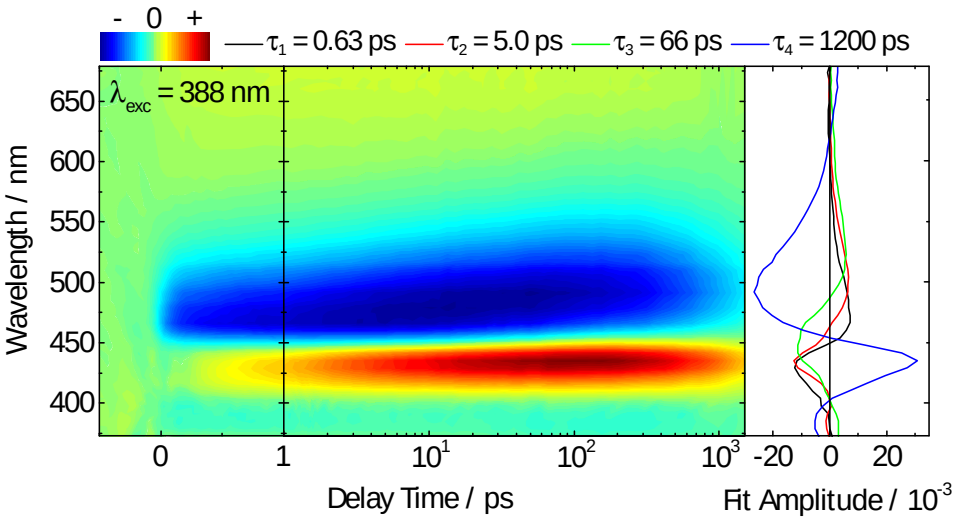

Figure 6.8: Transient absorption spectrum of DEACM-Glu in DMSO. The sample was photoexcited at the S_1-transition at 388 nm. Red indicates positive and blue negative absorbance changes. The corresponding DAS of τ_1 (black), τ_2 (red), τ_3 (green) and τ_4 (blue) are shown on the right.

The data of the ultrafast absorption measurements was analyzed by using a GLA (Figure 5.5.1). The measurement was successfully described with four time constants which are depicted in the decay associated spectra (DAS, Figure 6.8). The GSB is instantaneously present after photoexcitation at 388 nm but dominated by the strong ESA-signal above 400 nm. As for all absorbance changes in this spectrum, the GSB decays with 1200 ps (τ_4).

The build-up of the pronounced SE, centered at 475 nm at very early delay times, is described by τ_1. At longer delay-times of the experiment the SE shifts continuously bathochromic, which is displayed by τ_2 and τ_3 and can be explained by a dynamic Stokes-shift. The decay of the SE signal is described with τ_4. The dynamic Stokes-shift is corroborated by the strong ESA (425 nm) which is directly present but gains in intensity and reaches its maximum after roughly 200 ps. This phenomenon is described by the first three time constants. The ESA-signal decays with τ_4. The broad structureless positive absorbance change above 550 nm is directly present after photoexcitation and exhibits only a small signal which can be inferred from the DAS expressed by τ_4 (Figure 6.8).

The transient absorption spectrum after photoexcitation at 388 nm of DEACM-Glu in the DMSO-PBS-mixture (Figure 6.9) shows overall the same spectral signatures as the transient map described above (Figure 6.8). However, some significant changes can be distinguished which is perceivable by the different values of the time constants. Again, four time constants were necessary to describe the data properly. The lifetime

signals are now distinctly shorter and decay with a time constant of 940 ps (τ_4).

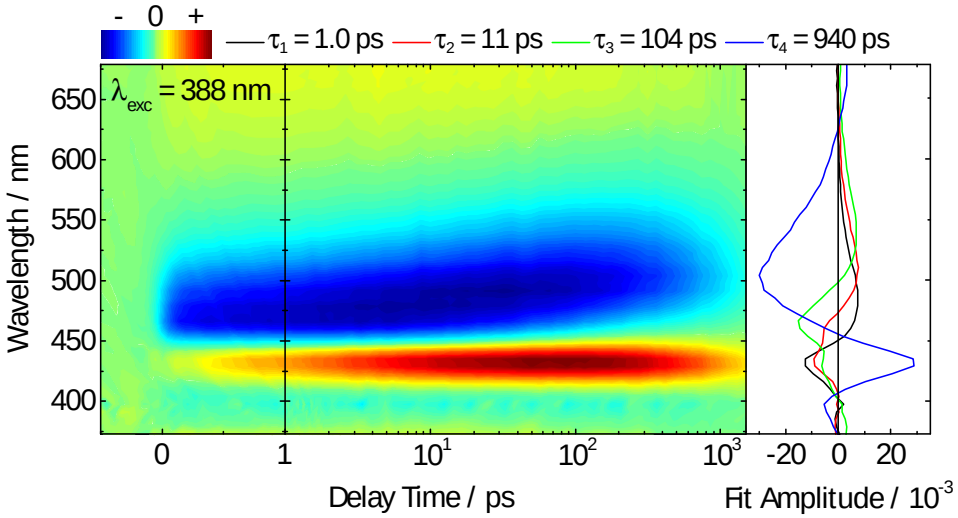

Figure 6.9: Transient absorption spectrum of DEACM-Glu in a DMSO-PBS-mixture (4:1). The sample was photoexcited at the S_1-transition at 388 nm. Red indicates positive and blue negative absorbance changes. The corresponding DAS of τ_1 (black), τ_2 (red), τ_3 (green) and τ_4 (blue) are shown on the right.

Besides of a shortened lifetime of the excited state, the second obvious difference between both measurements is the stronger red-shift of the SE at later delay times. This is highlighted by the elevated contribution of τ_3 (104 ps) at roughly 460 nm. As stated earlier, the origin of the bathochromic shift of the SE is a dynamic Stokes-shift. This effect seems to be enhanced by the additional water content of PBS. Due to this hydrogen bonds could be formed which stabilize the formation of the ion pair after photoexcitation (Figure 4.5). Moreover, the polar and protic solvent could support the formation of a TICT-intermediate (twisted intramolecular charge transfer). [150,158–160,163]

Figure 6.10 illustrates the different behavior of the SE in both experiments. The normalized transients at 473 nm reach the highest intensity after about 10 ps and decay afterwards. It is clearly seen that the measurement performed in the solvent mixture decays faster than the experiment in pure DMSO. The same applies for the transient traces at 535 nm, where the signal decays faster in the presence of water than in the case of pure DMSO. Furthermore, the transients at 535 nm show the influence of the dynamic Stokes-shift by reaching the maximum after about 150 ps. Most likely a TICT is observed in this experiment which is a common effect for coumarins exhibiting push-pull-substituents (Section 4.1.2, Figure 4.4).

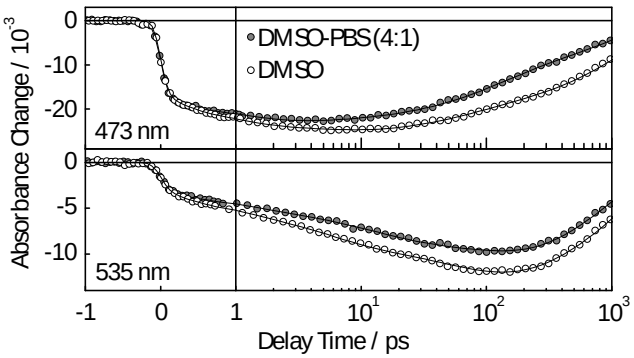

Figure 6.10: Transient absorbance changes of DEACM-Glu in DMSO (white-filled black circles) and in a 4:1 DMSO-PBS-mixture (gray circles) at two selected probe wavelengths.

6.2 ATTO 390

ATTO 390 is a strong fluorescent dye displaying high photostability and is often applied as fluorescence marker in many different systems.[207,208] The fluorophore consists of three six-membered rings, based on the coumarin structure with an annulated six-membered ring to the C7 and the C8 positions of the coumarin-structure (Figure 6.11). At the annulated ring ATTO 390 possesses a stereocenter leading to two stereoisomers. ATTO-Tec provides no information on the enantiomeric ratio besides, that it varies from batch to batch.

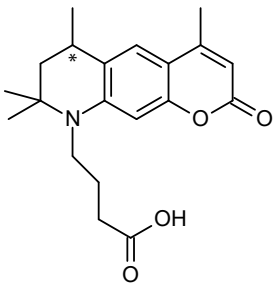

Figure 6.11: Chemical structure of ATTO 390 exhibiting a stereocenter marked with an asterisk.

The following, stationary and time-resolved spectroscopic studies on ATTO 390 shall provide insight to the photophysics of one component of the sensitizer-cage-system consisting of ATTO 390 and DEACM.

6.2.1 Stationary UV/vis Characterization

The absorption and fluorescence spectra are shown in Figure 6.12, where a large Stokes-shift of about 70 nm is visible resulting in negligible reabsorption effects. Furthermore,

ATTO 390 is distinguished by a fluorescence quantum yield of ∼1. The broad absorption band refers to the $S_0 \rightarrow S_1$-transition and enables an efficient photoexcitation between 360 nm and 410 nm. Due to the modest hydrophilic character of ATTO 390, the compound was dissolved in DMSO or DMSO-PBS-mixtures, leading to solvent-dependent shifts.

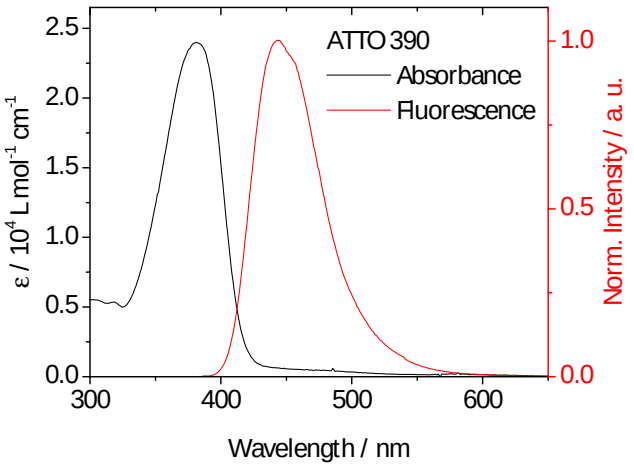

Figure 6.12: UV/vis absorption (black line) and fluorescence (red line) of ATTO 390 in DMSO.

6.2.2 Transient Absorption Spectroscopy

Ultrafast spectroscopic properties of ATTO 390 were investigated by UV/vis-pump-vis-probe experiments. For this purpose ATTO 390 was photoexcited at 388 nm close to its absorption maximum. The resulting transient absorption spectrum (Figure 6.13) is dominated by long-lived difference signals (>1.5 ns) which is in agreement with the measured fluorescence lifetime of (3.12 ± 0.09) ns in TCSPC measurements. The transient absorption spectrum displays three positive signals (<400 nm, centered at 440 nm and >600 nm) which are assigned to ESAs. All three positive signals decay with τ_3 (Figure 6.13) and most probably originate from one global positive signal which is superimposed with two intense negative signals. The first negative signal, centered at 410 nm belongs to the GSB of ATTO 390, representing only the low-energy side of the ATTO 390 absorption band, the strong overlapping ESA-signature below 400 nm compensates the bleach signal. The second negative signal (450 nm - 550 nm) is assigned to the SE, which shifts about 50 nm to lower energies over time. This effect was also observed for DEACM-OH and DEACM-Glu. Nonetheless, this effect is not as pronounced as in the other cases, which could be explained by the fixed alkyl substituent at the dialkylamino-group at the C7 position of the coumarin scaffold resulting in a confined

torsional motion of this group. Hence, a TICT-intermediate should be oppressed as reported in literature.[209]

Three time constants were necessary to describe the data of the ultrafast experiment. Apparently, all difference signals decay with τ_3, which is larger than the maximally achievable delay time of the measurement and therefore displays the end spectrum of the transient absorption measurement. The smaller time constants τ_1 and τ_2 describe the rise of the signals, which is seen in the corresponding DAS. The SE is directly present and shifts immediately to higher wavelengths (dynamic Stokes-shift), which is described with τ_1 and τ_2. Overall, the spectral signatures of ATTO 390 are comparable to those displayed in 6.8. However, DEACM-Glu does not exhibit a high-energy ESA as ATTO 390 does which overlaps most likely with the GSB, leading to a very sharp negative signal centered at 410 nm. Certainly, a strong ESA-signal around 425 nm is found for DEACM-Glu, which is less pronounced for ATTO 390 in Figure 6.13.

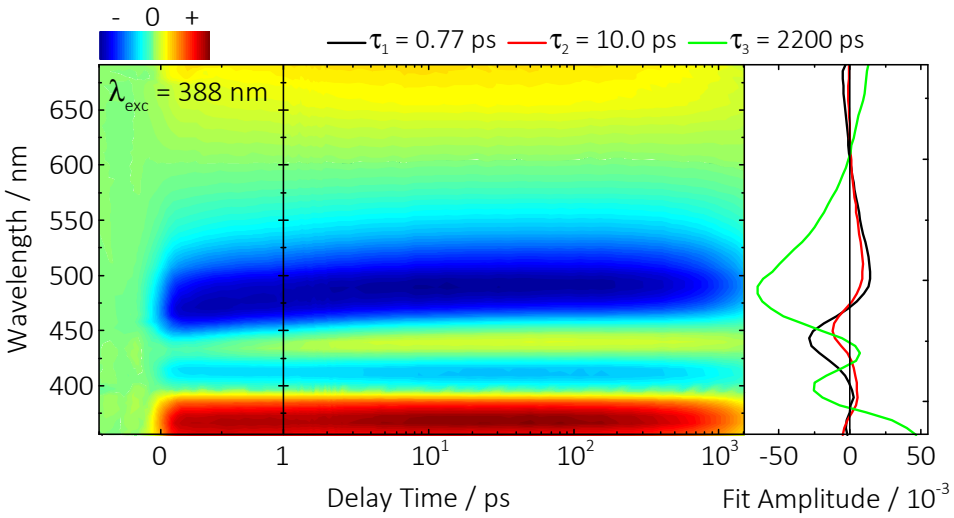

Figure 6.13: Transient absorption spectrum of ATTO 390 in DMSO. The sample was photoexcited into the S_1-state at 388 nm. Red indicates positive and blue negative absorbance changes. The corresponding DAS of τ_1 (black), τ_2 (red) and τ_3 (green) are shown on the right.

6.3 ATTO 390-DEACM-Glu

This section deals with the spectroscopic investigations of the novel antenna-cage-cargo-system ATTO 390-DEACM-Glu (I+II+III, Figure 4.6) and its corresponding photoproduct ATTO 390-DEACM-OH (I+II). Furthermore, photophysics of glutamate caged by DEACM with a propargyllinker (II+III) were examined for a better comparison of the novel triad and to assess the influence of ATTO 390.

In general, three major questions have to be answered. Firstly, does the newly designed system consisting of a 2P-sensitizer and the photolabile protecting group exhibit a greater two-photon absorption in comparison to regular DEACM? Secondly, does an energy transfer from the 2P-sensitizer onto the photocage occur and thirdly is the new system still capable to act as a photocage by liberating the caged compound glutamate? UV/vis characterization were carried out beforehand to answer these questions.

6.3.1 Stationary UV/vis Characterization

Figure 6.14 shows the absorbance of the triad composed of ATTO 390 (I), DEACM substituted at the C3 position (II) and glutamate (III) (Figure 4.6) and the absorbances of the isolated fragments. The triad exposes a very broad absorption band, ranging from 340 nm to 480 nm. Due to the alkyl chain of I and the ethinyl-subunit at the C3 position of the DEACM-scaffold an electronic decoupled system is expected. Thus, the absorbance of the triad is most likely composed of the sum of the absorption bands of the isolated fragments (Figure 6.14).

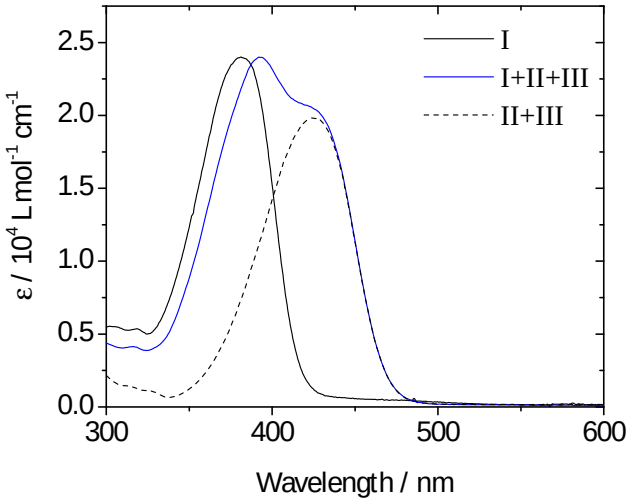

Figure 6.14: UV/vis absorption spectra of I (black line), the triad (blue line) and II+III (dashed black line) in DMSO. The absorption spectra of I and II indicate that the absorbance of triad is most likely composed of those contributions but that electronic interactions within the molecule are present.

Hence, the high-energy absorbance band around 400 nm originates from I, while the shoulder at the red flank of the absorption band refers to the absorbance of II. As already stated above, a substitution at the C3 position of the coumarin scaffold leads to a bathochromic shift in comparison to regular DEACM-OH. Hence, the absorption of II strongly resembles the red absorbance part of the triad. However, the absorption of incorporated I shifts resulting in an absorption maximum of the triad located at

400 nm which indicates electronic interactions within the dyad. Since an electronically decoupled system was expected, due to the non-conjugating linker between I and II, a π-stacking between both π-systems is considered.

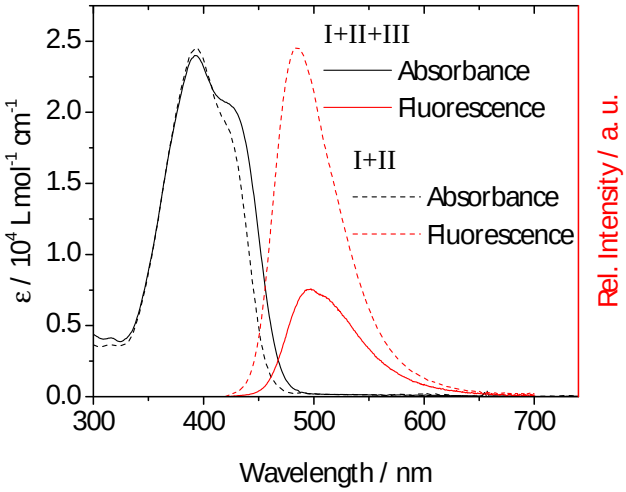

Figure 6.15: UV/vis absorption (black) and fluorescence spectra (red) of I+II (dashed line) and I+II+III (compact line) in DMSO.

The absorption and the fluorescence spectra of the triad and expected photoproduct I+II (dyad) are shown in Figure 6.15. In the case of the latter, the prominent shoulder in the red which is assigned to II, is missing or is not as pronounced as in the case of the triad. This could be explained by the fact that the absorbance of the photoproduct is hypsochromically shifted in comparison to the corresponding caged compound. This behavior was already observed for DEACM-Glu and DEACM-OH (6.3) and is reported for other coumarin-caged molecules in literature.[146,150,162,164,210–212]. In addition, the ϕ_{fl} is reduced for the caged compound compared to the photoproduct, as it was already seen for DEACM-Glu and DEACM-OH (6.2).

6.3.2 TPEF Measurements

Section 2.4 deals with the phenomenon of two-photon absorption and concludes several techniques for the determination of σ_{2P}. In this work, σ_{TPA} were determined with the TPEF-method (Section 5.5.2).[66,67] The technique was established by Xu and Webb and rely on the indirect determination of σ_{TPA} by the measurement of the fluorescence after two-photon absorption of a reference compound with known σ_{TPA} and the fluorescence after two-photon absorption of the sample with unknown values.

Rhodamine B, coumarin 307 and fluorescein were considered as reference compounds, since they exhibit decent σ_{TPA} and mainly emit in the same spectral region as I+II.

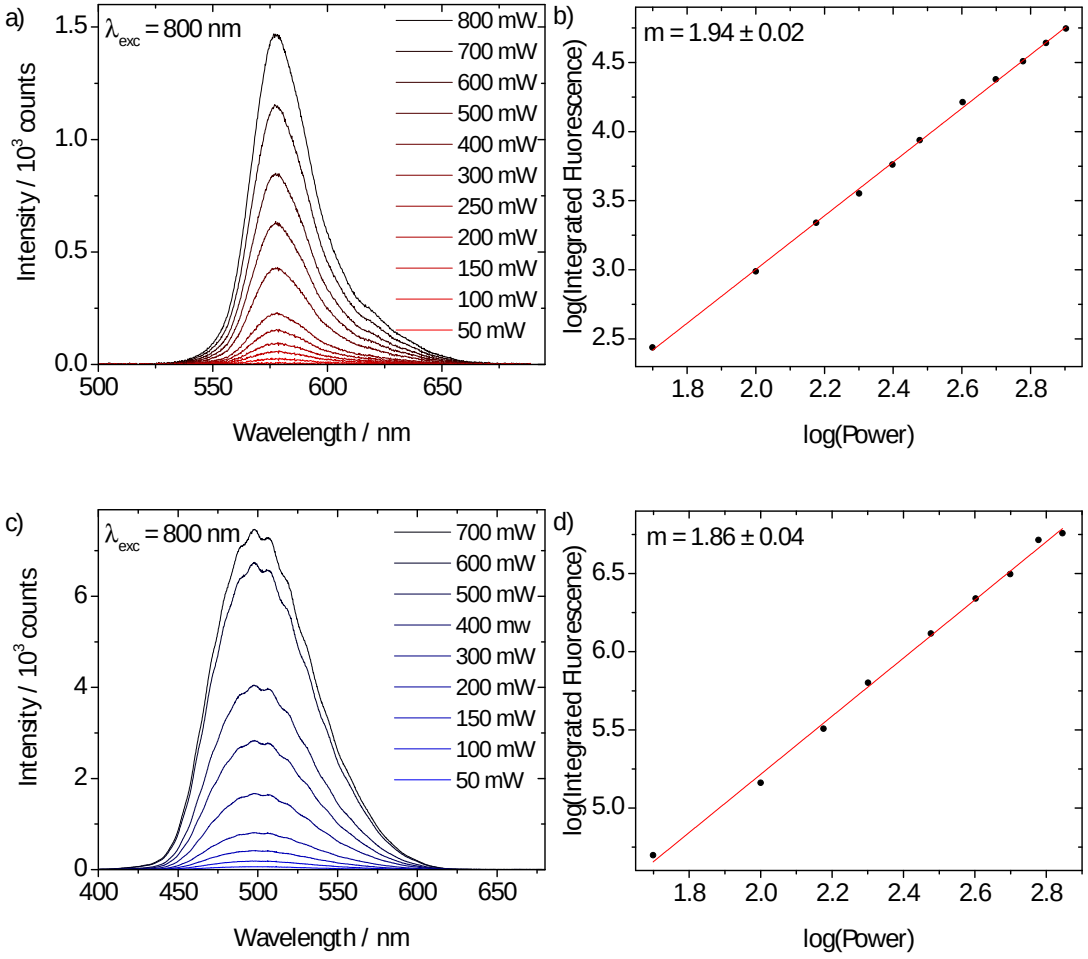

Figure 6.16: Power-dependent two-photon excited fluorescence of a) rhodamine B in MeOH and of c) the dyad in DMSO after photoexcitation at 800 nm. The logarithmic plots b) and d) show the integrated fluorescence against the power.[168]

Furthermore, the usage of more than one reference compound provides the advantage to validate the utilized setup by referencing the measured fluorescence spectra after two-photon excitation of the compounds with known σ_{TPA} on each other. For the determination of the σ_{TPA}, additional knowledge about the concentration of the sample and the refractive index of the solvent are required. Since the reference values of rhodamine B and coumarin 307 were determined in methanol (MeOH), the extinction coefficients of the samples had to be determined beforehand.

Broadband fluorescence was detected in a range from 400 nm to 700 nm after 2PA. Photoexcitation was tuned from 740 nm to 900 nm in 10 nm-steps, as reference values are given in a 10 nm-interval. In order to validate the 2PA effect, dependence on the power was investigated by photoexciting rhodamine B and I+II at 800 nm. Within the

measurement the power was varied from 50 mW to 800 mW. The power-dependent fluorescence spectra are depicted in Figure 6.16a and c, where the intensity decreases with the power. The logarithmic plots of the integrated fluorescence against the power (Figure 6.16b and d) reveal linear behavior with a slope of 1.94 and 1.86 for rhodamine B and the dyad, respectively. The determined values of the slopes illustrate an almost perfect quadratic dependence on the power and are in line with the value of (1.98 ± 0.03) for rhodamine B at excitation wavelengths of 770 and 825 nm determined by Xu and Webb.[66]

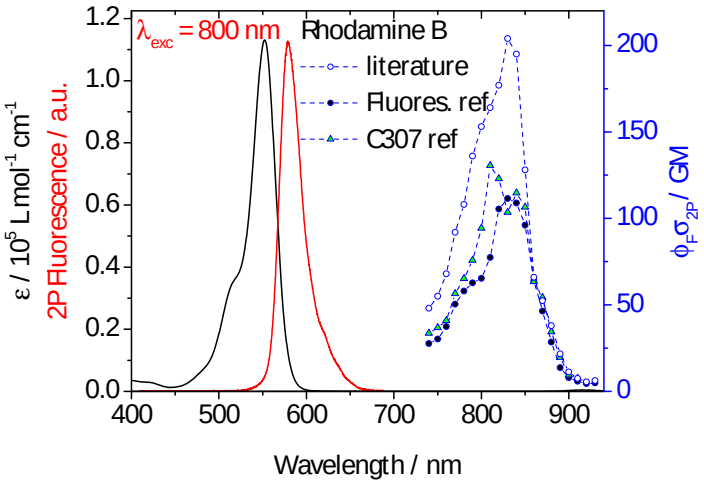

Figure 6.17: UV/vis absorption (black), two-photon excited fluorescence (red, $\lambda_{exc} = 800$ nm) and two-photon absorption spectra of rhodamine B in MeOH. The two-photon absorption spectra are taken from the literature (white circles) and measured and referenced both with fluorescein (black circles) and coumarin 307 (triangles).

The absorption, the fluorescence after photoexcitation at 800 nm and the two-photon absorption of rhodamine B are depicted in Figure 6.17. For the two photon absorption three spectra are displayed, containing the spectrum from the literature and the measured spectra referenced with fluorescein and coumarin 307. The spectral shapes of the referenced compounds are in agreement with the spectra taken from the literature.[66] However, the values deviate by a factor of two between 750 - 830 nm. In the publication of Xu and Webb a two-photon absorption spectrum is shown with values ranging from ~100 GM to about ~200 GM (Figure 6.17). In their work a large spectral width was covered by using different cavity mirror sets, which might have led to the significant deviations within the values. The absorption maximum of rhodamine B in MeOH is at 510 nm, while the two-photon absorption maximum is located at 850 nm, at half of this wavelength (425 nm) rhodamine B displays almost no absorption. The two-photon absorption spectrum of rhodamine B exhibits a local minimum at 900 nm, beyond this wavelength the absorption increases again. The spectrum indicates that two-photon

absorption is most efficient around 850 nm and shows with ∼200 GM (∼100 GM) comparatively large two-photon cross-section values. It shall be noted that TPEF is an indirect method for the determination of two-photon cross-sections. As outlined in Section 2.4.2, it is strongly coupled to the two-photon fluorescence quantum yield which should always be considered, when the values are determined with the TPEF-method.

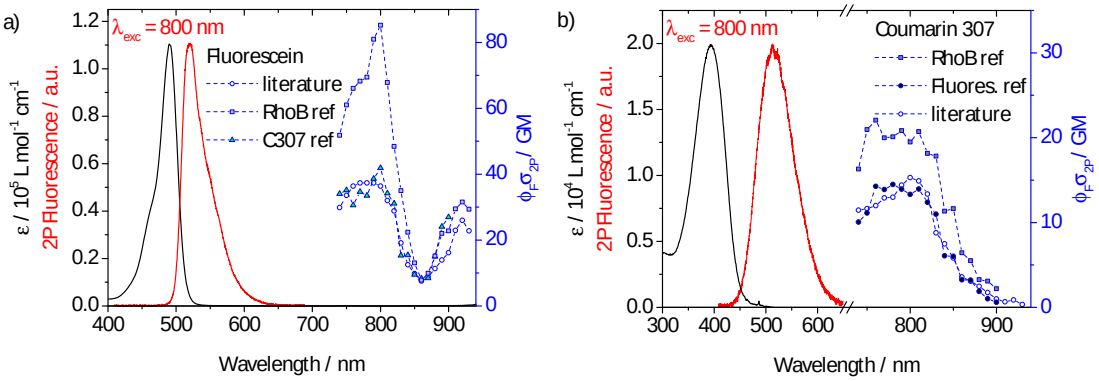

Figure 6.18: UV/vis absorption (black), two-photon excited fluorescence (red, $\lambda_{exc} = 800$ nm) and two-photon absorption spectra of fluorescein containing the literature values (white-filled blue circles) and the referenced measurements with rhodamine B (gray-filled blue squares) and coumarin 307 (green-filled blue triangles). b) UV/vis absorption (black), two-photon excited fluorescence (red, $\lambda_{exc} = 800$ nm) and two-photon absorption spectra of coumarin 307 taken from the literature (white-filled blue circles) and referenced with rhodamine b (gray-filled blue squares) as well as referenced with fluorescein (black-filled blue circles).

Figure 6.18 shows the absorbance, the fluorescence upon photoexcitation 800 nm and the two-photon absorption for a) fluorescein and b) coumarin 307. It is clearly visible that the literature values are in good agreement with the coumarin 307-referenced measurement of fluorescein and vice versa. The rhodamine B-referenced measurement of coumarin 307 and fluorescein show the expected behavior and exhibit values, which are half as high as the values extracted from the literature. Furthermore, fluorescein exhibits two-photon cross-section values of 60 GM at its maximum (820 nm), while coumarin 307 reveals values of 40 GM at an absorption maximum of 780 nm. No values for coumarin 307 are given beyond 890 nm, since no fluorescence could be detected.

All reference compounds were used in TPEF measurements of the samples with unknown σ_{TPA}, although rhodamine B shows large deviations. However, it resembles the two-photon absorption spectra of coumarin 307 and fluorescein very well. Furthermore, rhodamine B and fluorescein emit after photoexcitation beyond 900 nm, which was not detected for coumarin 307. Overall, fluorescein seems to be the best candidate for referenced TPEF measurements. Precautionary, rhodamine b and coumarin 307 were also

measured to monitor deviations within the measurement. The two-photon absorption spectra of I+II, ATTO 390 and of DEACM-OH are depicted in Figure 6.19.

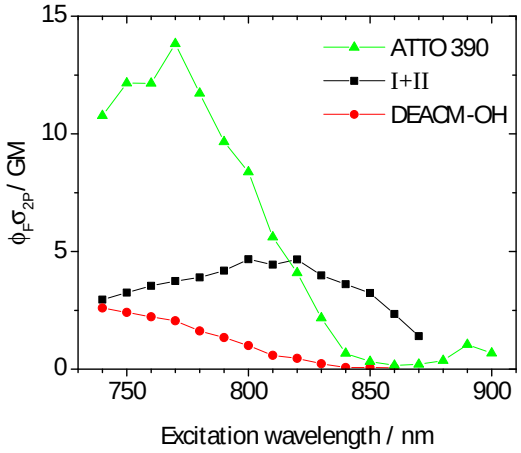

Figure 6.19: Two-photon absorption spectra of ATTO 390 (green triangles), I+II (black squares) and DEACM-OH (red circles) from 740 nm - 900 nm assessed with the TPEF-method. No data points for I+II above 870 nm and no data points of DEACM-OH above 850 nm are available, since no fluorescence was detected for the compounds in the respective range. All three two-photon absorption spectra are referenced with fluorescein and recorded in DMSO.

It is clearly recognizable that the σ_{TPA} values of DEACM-OH are the lowest of all three compounds. On the other hand I exhibits comparatively large σ_{TPA} values underlining that it is a good candidate for two-photon sensitization. I+II exhibits at all excitation wavelengths higher σ_{TPA} than DEACM-OH and in the range of 820 - 870 nm even larger values than I. However, TPEF, as an indirect method for the determination of $\sigma_{2\mathrm{P}}$, provides σ_{TPA} which depends on the material-specific ϕ_{fl} upon 2PA. In a first approximation, the one-photon excited fluorescence is equal to the fluorescence upon 2PA. Under this assumption, one-photon excited fluorescence quantum yields (ϕ_{fl}) of ATTO 390, DEACM-OH and the dyad were determined to be $\sim$1, (0.85 ± 0.09) and (0.70 ± 0.06), respectively. By taking the ϕ_{fl} into account, the two-photon absorption response of I+II is even larger.

6.3.3 Transient Absorption Spectroscopy

Ultrafast photodynamics of the dyad was investigated by femtosecond UV/vis-pump-vis-probe transient absorption measurements. Under the assumption that the absorbances of the isolated fragments resemble the absorbance of the dyad (Figure 6.14 in Section 6.3.1), although a bathochromic shift of ATTO 390 (I) is observed, the respective fragments were directly addressed by various excitation wavelengths. Hence, the chosen excitation wavelength of 365 nm should predominantly address the sensi-

tizer, whereas an exclusive photoexcitation of II at 475 nm is expected as I exhibits no absorption at this wavelength and therefore should only display the photodynamics of II. Presumably, photoexcitation at 388 nm should reveal the ultrafast spectroscopic properties of both aromatic components.

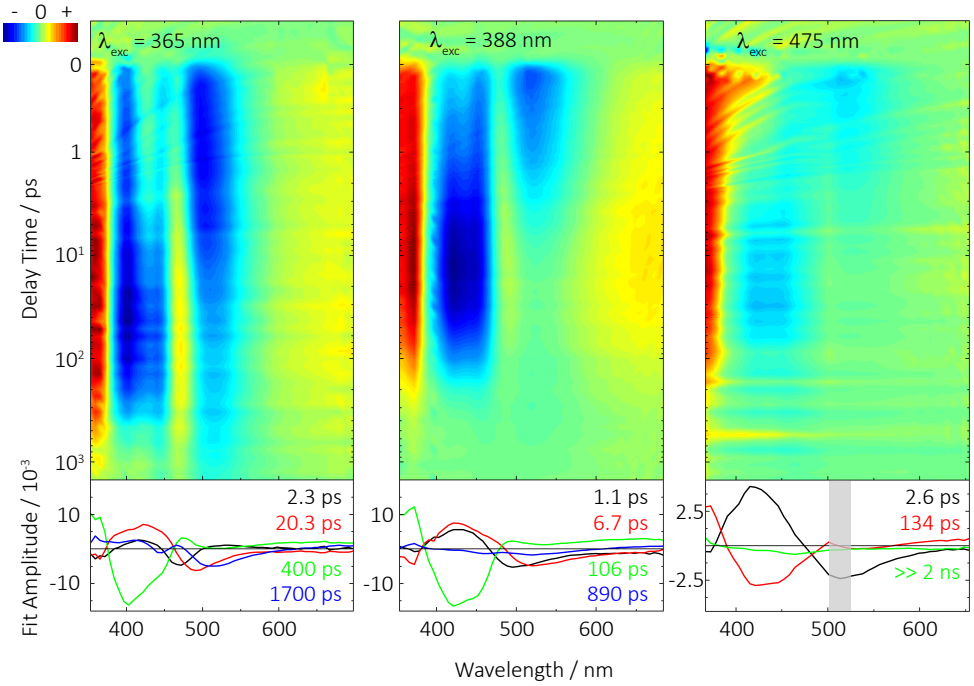

Figure 6.20: Transient absorption spectra of I+II in DMSO. The sample was photoexcited at three different wavelengths (365 nm, 388 nm and 475 nm). Red indicates positive and blue negative absorbance changes. The corresponding DAS are shown beneath the transient absorption spectra.

The resulting transient absorption spectra are depicted in Figure 6.20. On the right, the transient absorption spectrum after photoexcitation at 475 nm is shown. Due to the low absorption at this excitation wavelength, a rather noisy spectrum is obtained. However, a weak negative signal centered at 450 nm is directly present which becomes more intense at later delay times. This negative signal relates to the GSB of the DEACM-moiety. A second negative signal at around 500 - 600 nm is assigned to the SE which apparently decays very quickly with a time constant of 2.6 ps (DAS, Figure 6.20, bottom right). The same applies to a positive signal referring to the ESA of II which is located between 390 and 440 nm (Figure 6.20, right). With this time constant a third negative signal centered at 410 nm appears, which stems most likely from the GSB of I.

A direct photoexcitation of I (Figure 6.14) at 475 nm, as well as an intramolecular energy transfer (IET) from II to I, since this would imply an IET to higher energies, are excluded. Consequently, an intramolecular charge transfer (ICT) from II to I is

deduced. This assumption is supported by the short-lived excited state life time of II, indicated by the SE decay with the shortest time constant of 2.6 ps, although the ground state is not recovered yet which is indicated by the longer lived GSB of II at 450 nm. Finally, the charge recombination leads to the decay of all transient absorption signals (bleach of I and II) with a time constant of 134 ps (Figure 6.20, right).

The transient absorption spectrum recorded after photoexcitation at 388 nm depicted in Figure 6.20 (middle) is dominated by two negative signals. A closer look reveals that the negative signal from 400 - 500 nm consists of two separated signals. Similar to the transient absorption spectrum after photoexcitation at 475 nm, the negative signal between 500 and 600 nm is assigned to the SE, which seems to decay faster than the GSBs around 400 - 475 nm. As described above an ICT could be the origin of this finding. Contrarily, a fourth time constant is necessary to describe residual signals of long-wavelength SE and the GSB of II, while this time constant reveals no amplitudes for the short-wavelength GSB related to I.

The transient absorption measurement upon photoexcitation at 365 nm should represent mainly the photodynamics of I as the isolated ATTO 390 exhibits strong absorbance at this wavelength (Figure 6.20, left). The spectrum displays two intense negative bands centered at 400 and 500 nm. A third weak negative band at approximately 450 nm is directly present after photoexcitation. The negative signal at 400 nm is assigned to the short-wavelength ground state bleach of I, while the weak negative signal at 450 nm is related to the GSB of II, most probably due to direct photoexcitation. The third negative signal at 500 nm is allocated to the SE of I. However, since there is an immediate bleach of II, contributions of this moiety to the SE can be expected. Furthermore, three positive signals are observed of which two are present at time zero and frame the short-wavelength GSB and the SE. The third positive signal is centered at 475 nm and is visible after about 2 ps as it is superimposed with the strong negative signals. The data set was satisfactorily fitted with three time constants. The time constant τ_1 (2.3 ps) is most probably related to cooling and is accompanied by a red-shift of the SE and a blue-shift of the ESA of I ($<$400 nm). This is reflected by the derivative spectral feature of the τ_1 DAS between 360 - 400 nm and 450 - 500 nm. Directly photoexcited II could contribute to this time constant. A significant buildup of the GSB signal of II is described with a time constant of 20.3 ps indicating an IET from I to II. Surprisingly, the GSB of I does not seem to decay during this IET. This could be explained by a very fast ICT from II back to I, as already observed after direct photoexcitation of II (Figure 6.20, right). While both GSBs exhibit a decay component of 400 ps, the positive signals at $<$400 nm and $>$600 nm remain constant. These signals can stem either from a charge-separated state or from the ESA of I. At delay times of few hundred ps

to ns a small fraction of the GSB of II still persists, while the short-wavelength GSB completely decays. This leads to the conclusion that not all excited dyad molecules undergo the IET-ICT reaction cascade but remain in the excited state of II after IET. This is supported by the DAS of τ_3 and of τ_4 where the amplitude of τ_3 is more intense for the short-wavelength GSB, while it is positive for τ_4. Furthermore, the amplitudes of τ_4 are still negative in the wavelength-range of the GSB and SE (>500 nm) related to II describing its decay with 1.7 ns (Figure 6.20, left). This is in line with the shift of the SE to longer wavelengths corresponding to an IET from I to II.

The transient absorption measurement after photoexcitation at 475 nm are indicative for an ICT from II to I (Figure 6.20, right). On the other hand, the transient absorption spectrum upon photoexcitation at 365 nm (Figure 6.20, left) reveals the rise of the GSB signal of II but not a decrease of the GSB of I. A small part of the GSB of II lives up to 1.7 ns which is reflected by τ_4. SE of II at higher wavelengths supports the assumption of an IET from I to II. The major part of the GSB signal of II decays, like the GSB of I, after 400 ps indicating an ICT from II to I after an initial IET from I to II. This could explain the missing signature of the IET related to the GSB of I. A possible explanation supposes a certain heterogeneity of conformations. After an efficient energy transfer from I to II, a set of molecules could exhibit a conformation which facilitates an ICT from II to I resulting in the charge recombination and in a decay of the GSB signal after 400 ps. A second ensemble bears a conformation disabling the ICT resulting in the long-living GSB signal of II.

6.3.4 Quantum Chemical Calculations

In order to validate the findings gained from the ultrafast transient absorption measurements from Section 6.3.3, quantum chemical calculations were performed in the Burghardt group (Goethe-University Frankfurt). Optimization of the ground state structure of the novel photocage in gas phase and in a solvation model were calculated using the Gaussian09 program package at the TD-ωB97XD/SVP level of theory.[213]

The results of the geometry optimization displayed in Figure 6.21 (left) reveal an energetically favored conformer, where the hydrophobic moieties of I and II tend to arrange in a π-stacked manner. The alkyl chain of the ATTO 390 dye facilitates the π-stacking which is additionally corroborated by an intramolecular hydrogen bond between the hydrogen of the hydroxy group of DEACM and the carbonylic oxygen of the ATTO 390 linker. A linear conformer of I+II reveals a relative energy of about 25 kcal mol^{-1} higher than the π-stacked aggregate indicating rather low stability of the unfolded conformer.

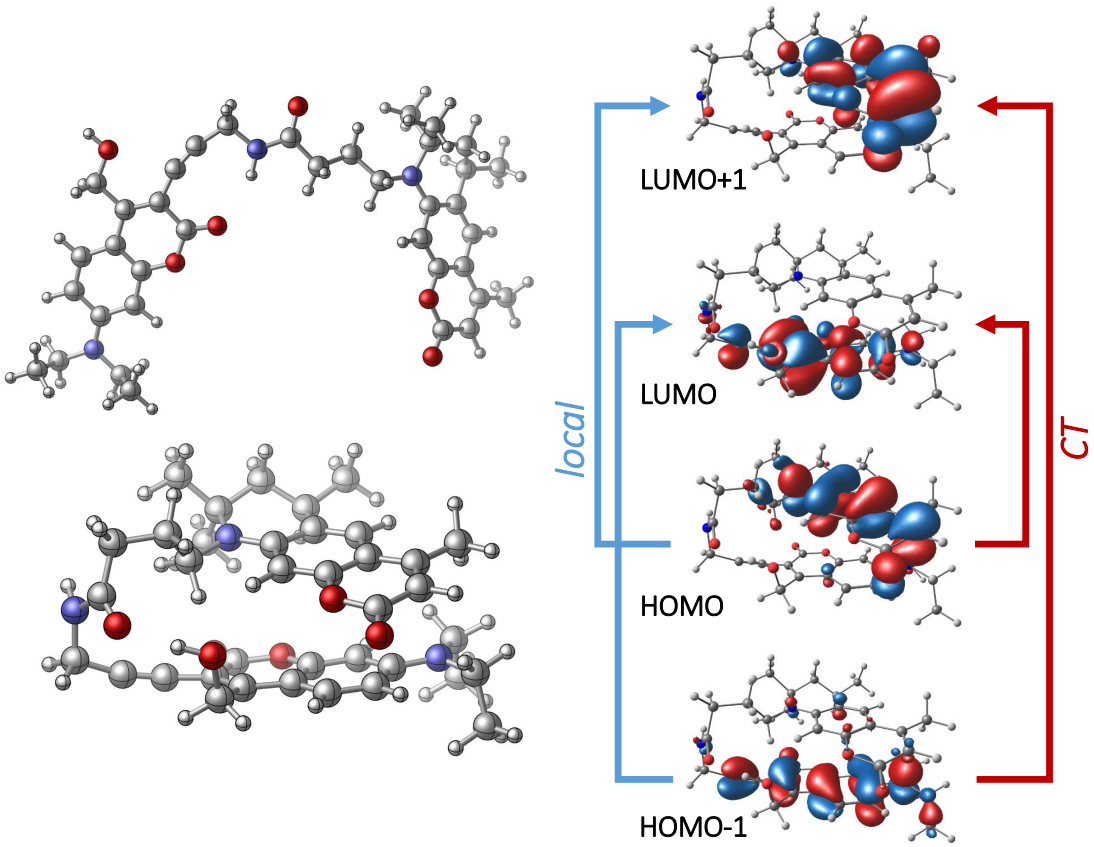

Figure 6.21: Left) Ball-and-stick model of two different conformations of the dyad (I+II) and their relative energies. While the stacked confomer exhibits an energy equal 0 (lower panel), the linear conformation displays an energy of 25 kcal mol^{-1}. Right) Results of TD-DFT calculations on the excited state analysis of the dyad are depicted on the right, revealing besides the local excitation a charge transfer contribution from I to II and vice versa. Calculations were performed and kindly provided by Konstantin Falahati.[168]

Moreover, TD-DFT calculations on the dyad using a solvation model and in gas phase were carried out to analyze the excited state dynamics. While the two bright states at 343 nm (3.6 eV) and at 306 nm (4.1 eV) reveal mainly local electronic excitation and rather marginal charge transfer contributions, the S_2-state (with an excitation energy at 320 nm (3.9 eV) is dominated by an intramolecular charge transfer character. This is directly derived by a reduced oscillator strength of one order of magnitude. The ICT-character can be inferred from the energetically preferred stacked conformation leading to a hampered exclusive electronic excitation of one of the moieties. Figure 6.21 (right) summarizes the results of the excited state analysis in which local electronic excitation is accompanied by ICT-contributions.

These findings are in good agreement with the results of the transient absorption mea-

surements where an ICT is observed from II to I. However, the results of the quantum chemical data do not support the assumption of an unstacking upon photoexcitation at 365 nm, since such a geometric rearrangement would include a lot of nuclear motion and should probably not occur on the ultrafast time scale.

6.3.5 Uncaging Experiments

The functionality of the novel photocage, in particular the liberation of the caged compound upon photoexcitation, was investigated by introducing glutamate via a carbamate to the coumarin moiety of the dyad, which consists of the two chromophores ATTO 390 and DEACM, yielding the triad I+II+III (Figure 4.6).

Irradiation of the triad should imply the decomposition of the carbamate linker and thus the release of carbon dioxide. Its asymmetric stretching mode ν_3 is known as a powerful reporter and therefore also claimed as a "vibrational chromophore".[214] Hence, uncaging experiments were conducted in the IR to interrogate carbon dioxide. Moreover, the absorbance change upon continuous irradiation of the triad was monitored in the UV/vis, since the experiments in Section 6.1.2 revealed a hypsochromic shift as well a decrease of the absorbance upon irradiation of the caged compound.

IR Measurements

Figure 6.22 shows the absorbance of the caged glutamate during continuous illumination with a central wavelength of 365 nm. The spectrum remains mainly constant, except of two prominent bands, where one rises and the other one decreases. Both absorbance changes are additionally shown in the magnifications next to the whole spectrum. The left spectrum shows the spectral window where the antisymmetric stretching mode (ν_3) of carbon dioxide (CO_2) is expected to be located.[214–217] Consequently, the increasing band centered at 2337 cm^{-1} (left) is assigned to the evolution of dissolved CO_2. Its origin most likely results from the decomposition of the carbamate linked between DEACM and glutamate. The photodecarboxylation of a caged compound linked via a carbamate to the photoactivatable cage has been shown in the past and monitors in this case the uncaging of glutamic acid.[150,170] Besides the increasing band, a second absorbance change is detected (Figure 6.22c), centered at 1722 cm^{-1} resulting most likely to the disappearance of the carbonyl vibration of the carbamate, due to its decomposition. This is in line with the generation of carbon dioxide in the photodecarboxylation reaction, since the origin of CO_2 stems from the carbamate linker. In line with this, in literature, the band centered at 1722 cm^{-1} was assigned to the absorption of the carbonyl vibration of the carbamate linker.[150,163]

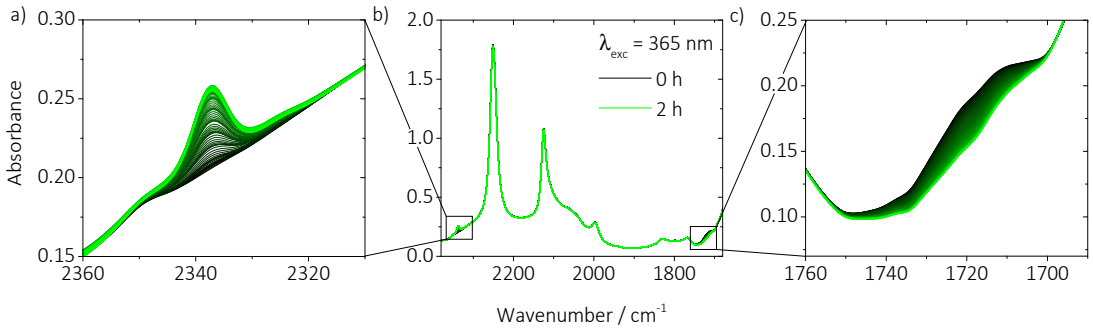

Figure 6.22: a) Formation of the CO_2-signal at 2337 cm^{-1} during continuous illumination at 365 nm of caged glutamate monitored via FTIR. b) Complete FTIR-spectra during the illumination experiment and c) decreasing band at 1722 cm^{-1}, which is allocated to the disintegration of the carbamate.

In order to investigate the influence of the two-photon antenna ATTO 390 on DEACM, uncaging experiments on glutamate caged by II (II+III) and the triad (I+II+III) were performed under identical conditions and the absorbance changes were detected in the IR-range Figure 6.23. The inset in Figure 6.23 shows the evolving asymmetric carbon dioxide band upon irradiation at 365 nm. The signal amplitude in the maximum of the increasing band (2337 cm^{-1}) was plotted against time for the novel synthesized photocage and for the photocage without antenna (Figure 6.23a). A more efficient uncaging of glutamate from the cooperative dyad is clearly evident. This is concluded from the very fast release of CO_2 displayed by a steep ascent (black circles). Both transients reach saturation indicating the end of the reaction and a successful uncaging of both compounds.

On the basis of the absorption spectra (Figure 6.14) of the novel synthesized triad and the control sample without antenna, a faster photodecarboxylation in the case of antenna-cage-cargo triad is not very surprising. The latter bears a significant absorption at 365 nm, while the absorbance of the control compound without I is negligible at this wavelength. Based on the absorption spectra, Figure 6.14 the introduction of ATTO 390 to the widely-used DEACM cage leads to an absorbance over a broader wavelength-range enabling to efficiently photoexcite the triad in this range, yielding the positive observations made in the uncaging experiment shown in Figure 6.23a.

Figure 6.23b shows the transients of the evolving antisymmetric stretching mode (ν_3) of carbon dioxide under continuous illumination with an LED with a central wavelength at 420 nm. It is again observed that the photodecarboxylation of the triad seems to be more efficient than that of the reference molecule II+III. However, a steeper rise of the reference photocage is monitored during photoexcitation at 420 nm than for 365 nm, which was expected due to the respective absorption. Intriguingly, the absorbances

of the triad and the photocage without ATTO 390 at 420 nm are more or less alike. Consequently, argumentation purely based on the absorption of both compounds at this wavelength seems to be inadequate. Electronic interactions within the triad or its CT-character, as discussed in Section 6.3.3, could be reasonable factors for the increased efficient photodecarboxylation observed in the IR experiments.

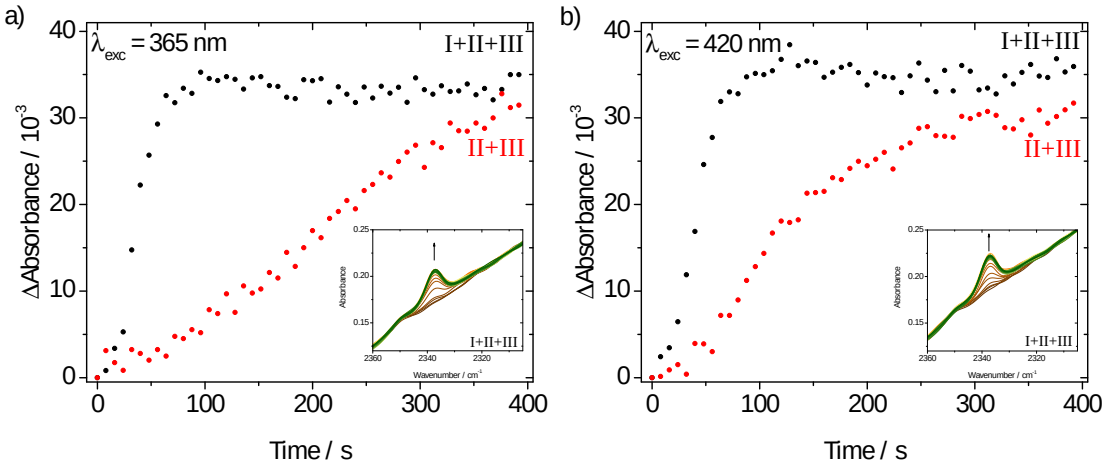

Figure 6.23: Transient absorbance changes at 2337 cm^{-1} of the triad (black circles) and of the reference photocage (red circles) monitored via FTIR measurements during photoexcitation at a) 365 nm and b) 420 nm. In both cases the rise of evolving CO_2 is faster for the triad than for the control sample without ATTO 390.

For further evaluation of the role of I within I+II+III, the sample was photoexcited at several wavelengths with the same photon flux (1.8×10^{16}; Table 6.1) The resulting absorbance changes were detected with an FTIR-spectrometer. Similar to the observations depicted in Figure 6.23, the linear rise of the evolving antisymmetric stretching mode of carbon dioxide upon illumination was fitted. The resulting slope of the linear fit was then referred to the absorption spectrum as shown in Figure 6.24. The slopes gained from the linear fit of the evolving CO_2-band after photoexcitation at the respective excitation wavelength resembles the absorbance of I+II+III with high similarity, except of the slope referring to 420 nm. A reasonable cause for this observation could be the photoexcitation of I and II in equal parts, thus a certain amount of energy is lost due to CT from II to I and from I to II. Consequently, a less efficient photodecarboxylation is detected. However, the decomposition of the carbamate linker and thus the release of CO_2 at this wavelength is still more efficient with I than without the two-photon sensitizer as seen in Figure 6.23b.

In a nutshell, the functionality by means of uncaging could be proven by continuous illumination experiments on the ATTO 390-based photocage and on a reference

Table 6.1: Peak Wavelengths and Referring Power of LEDs Used for IR-uncaging Experiments.

peak wavelength / nm	365	385	405	420	455	470
power / mW	9.8	9.3	8.8	8.5	7.9	7.6

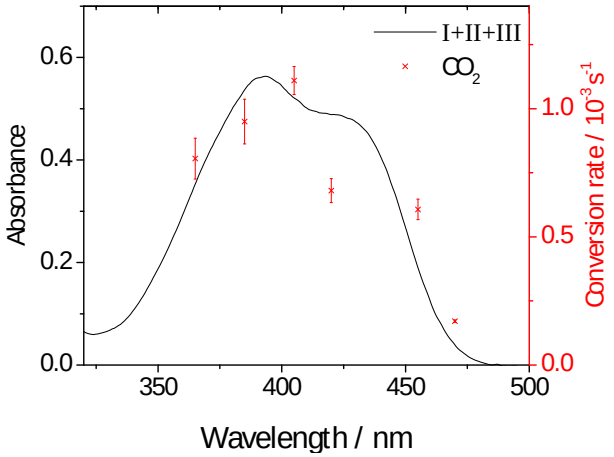

Figure 6.24: The release of CO_2 after photoexcitation at several wavelengths was detected and the transients at 2337 cm^{-1} were linearly fitted. The resulting slopes were compared to the absorption spectrum of the triad.

photocage without the 2P-sensitizer detected in the IR. This finding was derived by the decomposition of the carbamate and the accompanying photodecarboxylation monitored by the evolving antisymmetric stretching mode (ν_3) of the released carbon dioxide during continuous illumination. ν_3 is therefore excellently suited as an indicator for the uncaging of glutamate. Moreover, a positive influence of the incorporation of I is deduced from the control experiments. This can be inferred from the absorbance of I in the UV and the cooperative communication with the photocage II, enabling an uncaging reaction over a wider spectral range. The latter point also leads to a more efficient uncaging of glutamate in the case of the antenna-based photocage compared to the control compound.

UV/vis Absorption

According to literature and the findings in Section 6.1.2 a hypsochromic shift of the DEACM band should be observed in the UV/vis after photoexcitation of DEACM-caged compounds.[146,150,162,164,210–212] Figure 6.25a displays the UV/vis-absorption of I+II+III under continuous illumination at 365 nm. Figure 6.25b depicts the absorbance changes during the illumination experiment. It can be clearly seen that the absorbance in the wavelength-range between 390 nm and 420 nm increases, while the shoulder at

higher wavelengths at around 475 nm merges into the blue region. The increase of the absorbance is in line with the higher extinction coefficient found for the photoproduct I+II. Also the hypsochromic shift of the absorbance is in accordance with the observations made so far regarding uncaging experiments. An absorbance between 500 - 600 nm, as found in the uncaging experiments of DEACM-Glu (Section 6.1.2) is in this case negligible, indicating that no further photoproduct than I+II is formed. A fact supporting this assumption is the sharp isosbestic point located at around 450 nm. Derived from the results obtained in the FTIR measurements, the absorption changes observed in the stationary UV/vis measurements (Figure 6.25) are assigned to the uncaging of glutamate. Subsequently, an uncaging quantum yield (ϕ_u) of 1.5% was determined (Section 6.3.5).

For comparison, further UV/vis measurements on the reference compound II+III were performed. As already observed in the other continuous illumination experiments, the hypsochromic shift suggesting an uncaging reaction is present. However, a decrease of the absorbance maximum at around 420 nm is detected which also indicates a photodegradation of the compound. Moreover, an absorbance arises between 500 and 600 nm, which was also found in the continuous illumination experiments for DEACM-Glu (Section 6.1.2) leading to the assumption of a further photoproduct as already discussed in the previous section. Nonetheless, an ϕ_u was determined which is one order of magnitude lower than the ϕ_u of I+II+III, Section 6.3.5.

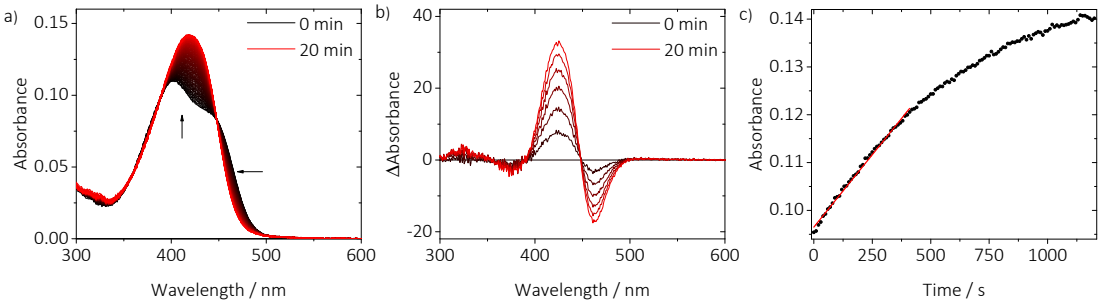

Figure 6.25: a) Absorption of I+II+III under continuous illumination at 365 nm monitored in the UV/vis revals a hypsochromic shift of the shoulder at the red side of the absorption band. Furthermore, the rise of the absorbance and the isosbestic point at around 450 nm indicate the formation of the photoproduct and hence uncaging of glutamate. b) Absorbance change of I+II+III during illumination. c) The linear behavior of the transient at 421 nm in the beginning is fitted (red line) for further calculation of the ϕ_u.

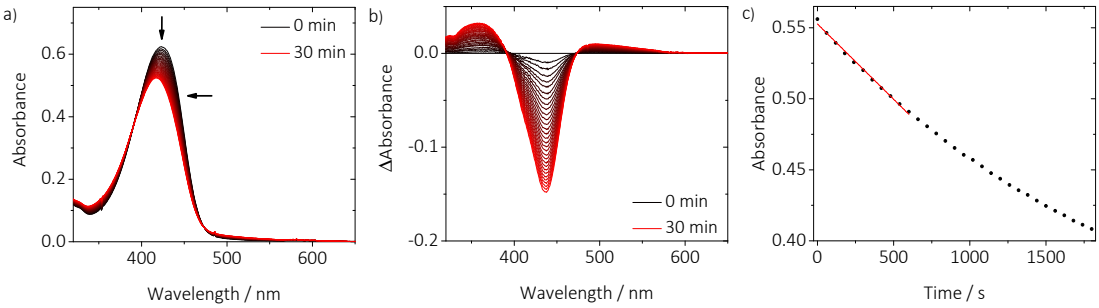

Figure 6.26: a) Absorption of II+III under continuous illumination at 365 nm monitored in the UV/vis shows a hypsochromic shift and a decrease of the absorbance. b) Absorbance change of II+III during illumination. c) The linear behavior of the transient at 440 nm in the beginning is fitted (red line) for further calculation of the ϕ_{u}.

Uncaging Quantum Yield

As described in Section 4.1, decisive information on the functionality of a photolabile protecting group can be derived from the photochemical quantum yield (ϕ_{u}) which indicates the efficiency of the observed photochemical reaction. In this particular case the uncaging reaction (ϕ_{u}) which describes the ratio between the number of liberated molecules and the number of absorbed photons by the sample at the given wavelength (Eq. 6.1).

$$\phi_{\mathrm{u}} = \frac{n_{rel}}{n_p} \tag{6.1}$$

In the past, the product of quantum yield and extinction coefficient ($\phi_{\mathrm{u}}\varepsilon(\lambda_{\mathrm{exc}})$) was increasingly used as a measure to assess the uncaging reaction at a specific wavelength.[71] Since, the photochemical reactions in the UV/vis and in the IR are assigned to the successful liberation of the caged compound glutamate, two different types for the determination of the ϕ_{u} are possible.[170] In both cases the determination of the quantum yield requires exact knowledge of various parameters.

According to the Beer-Lambert-equation, the number of released molecules can be expressed as follows (Eq. 6.2):

$$n_{rel} = \frac{A_{rel} V N_A}{\varepsilon_{rel} d} \tag{6.2}$$

with V as the excited sample volume, $\varepsilon_{\mathrm{rel}}$ as the extinction coefficient of the released product at the given wavelength and d as the pathway of the excitation light traveling through the sample.

However, the time-dependence of product formation has to be taken into account. For this purpose, the product absorbance A_{rel} is substituted by the product of the

total illumination time and m, the slope describing the linear relation between product absorption and the total illumination time t, yielding the following equation:

$$n_{rel} = \frac{mtVN_A}{\varepsilon_{rel}d} \tag{6.3}$$

The number of absorbed photons is derived from the precise knowledge of the parameters which define the excitation beam used for uncaging and the absorbance of the product at time zero. In Eq. 6.3 the energy of the excitation beam is replaced by the product of power and time. Furthermore, the proportionality between the power and the transmission of the product at time zero ($t = 0$) is taken into account, yielding the following formula for absorbed photons:

$$n_p = \frac{Pt\lambda(1 - 10^{-A_0})}{hc} \tag{6.4}$$

with λ as excitation wavelength, h as *Planck's* constant and c as the speed of light.

According to Eq. 6.1, forming the quotient of Eq. 6.3 and 6.4, the quantum yield is obtained and can be expressed in the following formula:

$$\phi_{\mathrm{u}} = \frac{n_{rel}}{n_p} = \frac{mVN_Ahc}{\varepsilon_{rel}dP\lambda(1 - 10^{-A_0})} \tag{6.5}$$

In the particular case, the absorbance changes of I+II+III induced by continuous illumination are assigned to the uncaging of glutamate (Figure 6.25). 421 nm was selected as wavelength and the early part of this transient was fitted linearly (Figure 6.25c). The resulting slope m (6.1×10^{-5}) was inserted in Eq. 6.5, as well as 1.5 mL for V, $2.1 \times 10^4\,\mathrm{M^{-1}\,cm^{-1}}$ for the extinction coefficient at 421 nm and an educt absorbance A_0 of 0.06 at the excitation wavelength ($\lambda_{\mathrm{exc}} = 365\,\mathrm{nm}$) at time zero yielding an ϕ_{u} of $(1.47 \pm 0.15)\,\%$.

However, it should be noted that the value for the quantum yield is most probably underestimated, since the referring photoproduct absorbs in the same spectral region as the initial triad. Therefore, a photoexcitation of both compounds becomes more and more realistic as the duration of the experiment evolves. ϕ_{u}-values of $(1.38 \pm 0.03)\,\%$ and $(1.62 \pm 0.04)\,\%$ were determined for excitation wavelengths at 385 nm and 455 nm and are located in a reasonable range. A wavelength-dependent behavior could not be derived, indicating that in all three cases almost the same amount of energy is used for the process of uncaging. The same procedure was applied for the reference compound II+III (Figure 6.26). By inserting m (1.1×10^{-4}) as well as 1.5 mL for V, $2.4 \times 10^4\,\mathrm{M^{-1}\,cm^{-1}}$ for the extinction coefficient at 440 nm and an educt absorbance A_0 of 0.62 at the excitation wavelength ($\lambda_{\mathrm{exc}} = 420\,\mathrm{nm}$) into Eq. 6.5 a ϕ_{u} of $(0.12 \pm 0.03)\,\%$ is obtained for the uncaging reaction of II+III.

6.4 Concluding Remarks

In this chapter the results concerning the improved photocage equipped with a 2P-sensitizer were presented. The first sections dealt with the photochemical characterization of the isolated, the well-known photocage DEACM and the antenna sensitized to 2PA ATTO 390 were investigated regarding their spectroscopic characteristics.

Stationary UV/vis measurements revealed that the caged compound (DEACM-Glu) and the corresponding photoproduct, the coumarin alcohol (DEACM-OH) exhibit similar properties. In detail, the absorbance of DEACM-OH is blue-shifted compared to the absorbance of DEACM-Glu. A similar observation was made in solvent-dependent studies, in which hypsochromic shifts were detected for the compounds in DMSO with respect to the compound in PBS. Continuous illumination experiments on DEACM-Glu induce absorbance changes which are characterized by a shift to higher energies indicating a successful uncaging reaction and are in line with the literature.[146,150,162,164,210–212] Certainly, a decrease of the absorbance during the experiment was detected which is assigned to a photodegradation. However, a second prominent absorbance change was detected at longer wavelengths. This absorption band was even more pronounced in uncaging experiments with DMSO as solvent. The reaction mechanism Figure 4.5 in Section 4.1.2 indicates the formation of a DEACM-aldehyde which is supported through literature.[165]

The solvent dependence of the DEACM-Glu dynamics was also studied in ultrafast transient absorption experiments, where shortened excited state lifetimes and a larger dynamic Stokes-shift were detected for DMSO/PBS-mixtures compared to experiments in pure DMSO. An uncaging reaction was not observed on this time scale, in fact, high similarity to transient absorption spectra of DEACM-OH are present. The fluorescence signal exhibits the most significant difference between DEACM-Glu and the corresponding photoproduct, it is quenched to one third for the caged compound.

ATTO 390 exhibits excellent fluorescent properties, which are characterized by a ϕ_{fl} of $\sim$1. In addition, it was shown that a large Stokes-shift leads to a negligible overlap between absorbance and fluorescence. Moreover, the emission band exhibits a good overlap to the absorption of a DEACM compound substituted at the C3 position. Furthermore, glutamate was linked via a carbamate to DEACM, since a photoinduced reaction would lead to a photodecarboxylation, hence the release of carbon dioxide which is characterized as powerful vibrational marker. Consequently, the uncaging reaction can be monitored.

The target system's absorbance mainly resembles those of the isolated fragments,

indicating an electronically decoupled system which can be explained by the relatively long alkyl chain between the two aromatic moieties. However, a certain intramolecular interaction can be inferred from the bathochromic shift of the ATTO 390 absorption within the dyad. On the basis of this, transient absorption spectra were performed in a wavelength-selective manner in order to address the respective fragments. The experiments revealed an ICT from DEACM to ATTO 390 and from ATTO 390 to DEACM. An IET could be inferred from the transient absorption spectrum after photoexcitation at 365 nm at later delay times. An approval of the experimental findings were provided by quantum chemical calculations. Ground state geometry optimization revealed a stacked conformation of the dyad facilitated by the alkyl chain of ATTO 390. Thus, a charge transfer character of the dyad was assumed and subsequently confirmed by excited state analysis.

The improvement of DEACM by means of 2P-response was investigated by TPEF measurements. 2PA spectra of the reference compounds and of I+II, DEACM-OH and I were obtained by varying the excitation wavelength from 730 to 900 nm. 2PA spectra of the reference compounds are in high agreement to 2PA spectra taken from the literature. The dyad exhibits at all wavelengths larger σ_{TPA} values than the widely-used DEACM. Hence, an improvement of the 2PA via this approach was achieved. The uncaging functionality was investigated in the IR and in the UV/vis by continuous illumination of I+II+III. Furthermore, a reference caged glutamate was measured under the same conditions to investigate the influence of I. Both compounds reveal the intense absorption of carbon dioxide upon photodecarboxylation. In case of the triad a more efficient uncaging was detected. Furthermore, the introduction of ATTO 390 extends the triad's absorbance in the UV enabling a more efficient absorption over a broader wavelength-range. A fact which was exploited in uncaging experiments in the UV/vis, where the earlier observed hypsochromic shift upon uncaging was visible. Furthermore, the absorption increased within illumination time which is in line with the higher extinction coefficient of the photoproduct. Finally, an ϕ_{u} of 1.5% was extracted from the experiment. Comparative experiments of II+III revealed a ϕ_{u} of one order of magnitude lower.

In summary, a novel functional photocage consisting of the common DEACM equipped with ATTO 390, as a 2P-sensitizer, was established and successfully characterized spectroscopically. Wavelength-dependent transient absorption measurements gave insight to the ultrafast photodynamics of I+II. In particular, the measurements disclosed ICT from ATTO 390 to the DEACM moiety and vice versa. This experimental finding was supported by quantum chemical calculations which additionally revealed a stacked conformation facilitating the ICT within the molecule.

7

Ultrafast Dynamics of Photoresponsive Systems

This chapter deals with the results on three different photoresponsive systems including measurements obtained with the Kerr shutter (Section 3.2). As already stated in Section 3.2.2, it is used to investigate ultrafast fluorescence. In particular, the setup for capturing femtosecond fluorescence is then advantageous over transient absorption spectroscopy, if stimulated emission in pump-probe experiments is superimposed with other signals and therefore the SE is not visible, leading to a difficult interpretation of the photodynamics.

Consequently, measurements on the Kerr shutter can be carried out to gain further information on the excited state lifetime of the photosystems of interest. In this work, three Kerr shutter measurements are shown. Two experiments were conducted on photochromic systems (Section 7.1 and 7.2). The third measurement discloses the ultrafast deactivation of photoexcited dodecin, a flavin-binding protein.

7.1 BODIPY-DTE

The here presented BODIPY-DTE dyad consists of boron-dipyrromethene (BODIPY) and dithienylethene (DTE) connected via a phenyl-ethinyl-phenyl bridge (Figure 4.10). The photomodulation of the BODIPY fluorescence via ring-opening and ring-closing DTE is described in Section 4.2.1. The emission of BODIPY is investigated with stationary and time-resolved measurements.

Figure 7.1 shows the absorbance and fluorescence of the dyad in the open and in

the photostationary state (*pss*). The absorption spectrum of the dyad in the open state comprises the absorbances of the isolated fragments, where DTE absorbs in the UV-region (λ_{max} = 328 nm) and BODIPY exhibits a very sharp absorption, peaking at 526 nm. While the open state of the BODIPY-DTE does not absorb light above 570 nm, a prominent band from approximately 560 nm to 750 nm arises in the *pss*. This absorbance stems from the closed DTE (fraction) in the *pss*. Furthermore, the absorbance of DTE in the UV experiences a bathochromic shift of about 30 nm. Due to a rather small Stokes-shift of about 20 nm the BODIPY fluorescence exhibits its maximum at 546 nm. Moreover, the fluorescence is quenched to about 5% in the *pss* compared to the fluorescence in the open state, reflecting the substantial fluorescence contrast. In addition, the dyad exhibits good photostability inferred from consecutive switching cycles, making it a promising candidate for the photomodulation of fluorescence.[181]

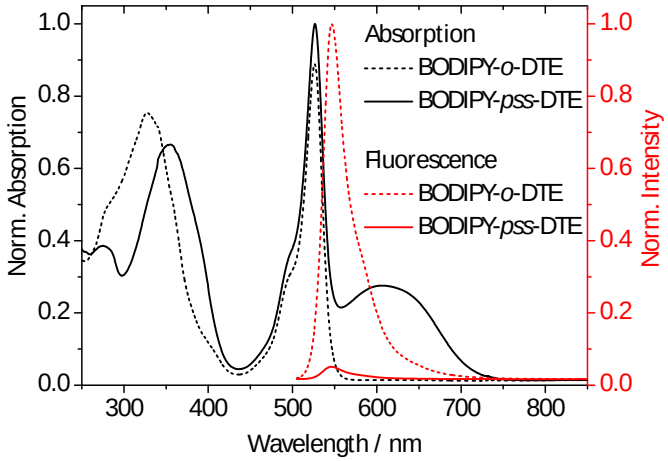

Figure 7.1: Stationary absorption and fluorescence spectra of the BODIPY-DTE dissolved in dichloromethane (DCM) in the open and the *pss*. The absorbance is composed of additive contributions of the isolated fragments. Measurements were performed and the data kindly provided by Dr. Felix Schweighöfer and Dr. Lars Dworak.[181,186]

Transient absorption measurements of the cooperative dyad in the open and the *pss* are depicted in Figure 7.2. In order to predominantly address BODIPY, both states were photoexcited close to their absorption maximum at 500 nm. The accumulation of a photoproduct was prevented by continuous back illumination with UV-light.[181] Figure 7.2 (left) displays the measurement on the open form of BODIPY-DTE where two prominent signals can be identified. A negative signal, centered at 530 nm refers to the GSB of the BODIPY moiety and is most likely overlaid with the SE. This is in line with stationary measurements which reveal a rather small Stokes-shift. The second signal is located above λ_{pr} = 675 nm and is assigned to the ESA. Both signals exhibit relatively slow decay dynamics resulting in clearly visible residual difference signals at maximal

delay time. As DTE is present in its open form in this measurement, the dyad behaves as an electronically decoupled system. Hence, the observed signals upon photoexcitation of the BODIPY fragment should solely display the donor photodynamics. An influence on the kinetics by the DTE molecule can thus not be extracted from this measurement.

Transient absorption measurement of the BODIPY-DTE in the *pss* exhibits, as well, the above described signals (Figure 7.2, right). Initially, the signals are spectrally indifferent compared to the those from the measurement on the open form but vary in amplitudes at identical probe-wavelengths. In addition, dramatically reduced lifetimes can be found where both signals decay within approximately 20 ps. This finding indicates an efficient energy transfer from the donor BODIPY to the acceptor DTE. Although the chosen λ_{exc} should predominantly excite the BODIPY-fragment, residual photoexcitation of DTE in the *pss* cannot be fully excluded. Indeed, a double difference spectrum at $t_{delay} = 0.5$ ps of the measurements on the *pss* and the open form revealed a spectral signature, which was also found after photoexcitation at 600 nm of isolated DTE, referring to the GSB of closed DTE indicating the direct photoexcitation of the DTE residue.[181] A signature of excited DTE after energy transfer is not found, as its ground state recovers after 2.2 ps and is therefore not observable.[218]

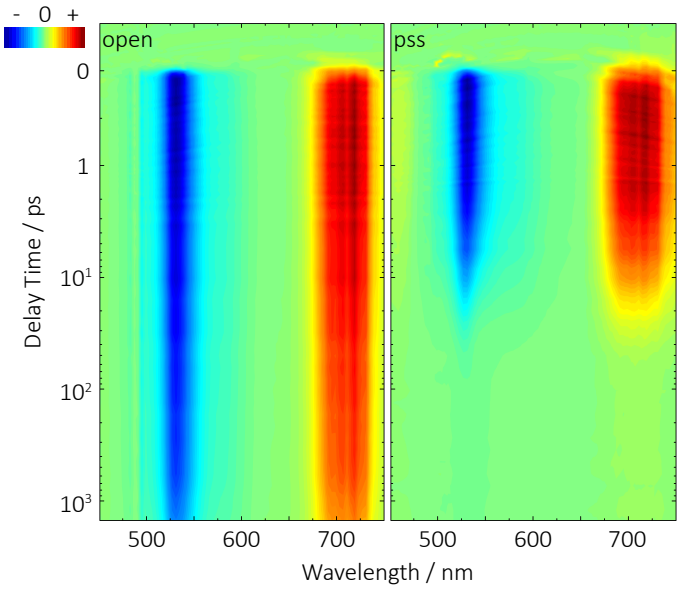

Figure 7.2: Transient absorption spectra of the open (left) and the *pss* (right) of the BODIPY-DTE dyad recorded after photoexcitation at 500 nm. Red indicates positive and blue negative absorbance changes. Measurements were performed and the data kindly provided by Dr. Felix Schweighöfer and Dr. Lars Dworak.[181,186]

Besides transient absorption measurements, time-resolved fluorescence experiments have been carried out (Figure 7.3). A fluorescence lifetime of (4.30 ± 0.01) ns was ex-

tracted from TCSPC-measurements on the open state (Section 5.5.3). The same time constant was found in measurements on the *pss*, describing the decay of the fraction of open isomer in the *pss*. Moreover, a fast signal in the ps-time regime is detected only for the *pss*, which becomes clearly visible in the difference spectrum of the traces from TCSPC-measurements (Figure 7.3b).

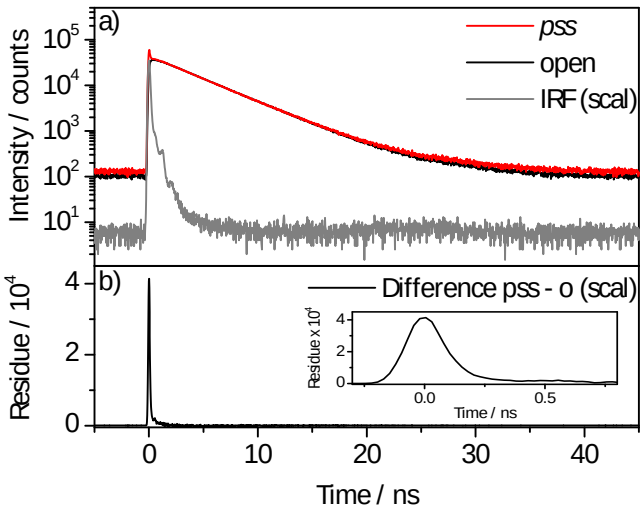

Figure 7.3: a) Time-resolved fluorescence of the BODIPY-DTE dyad in the open (black) and the *pss* (red) measured with the TCSPC method recorded after photoexcitation at 483 nm. The gray trace represents the scaled instrument response function. b) Difference of the two fluorescence traces of BODIPY-DTE in the open and in the *pss* revealing a fast signal which is magnified in the inset. Measurements were performed and the data kindly provided by Henrik Gustmann.[181]

Subsequently, time-resolved fluorescence on the early ps-time scale was recorded using a Kerr shutter setup. A photoexcitation close to the absorption maximum of BODIPY at 504 nm was chosen. The sample was continuously pumped and illuminated with UV-light to freshly generate the *pss* and to prevent accumulation of the dyad in the open form. The time-resolved fluorescence displays a fast decay after photoexcitation of BODIPY-DTE in the *pss*. Figure 7.4 reveals high agreement between the fluorescence trace recorded at 546 nm with the Kerr shutter and the transient absorption trace at $\lambda_{pr} = 547$ nm. The fluorescence and the transient absorption trace were both fitted using exponential decay functions, resulting in similar excited state lifetimes of (15.3 ± 0.4) ps and (9.7 ± 0.3) ps, respectively. As DTE is present in its closed form, it draws a highly-conjugated dyad which leads to a photochromic Förster resonance energy transfer (pcFRET) as consequence of photoexcitation of the BODIPY. Intriguingly, the orthogonal arrangement with respect to the dipole moments of both chromophores in the dyad makes a pcFRET less favorable. However, polarization changes of the solvent

or vibrational motions can influence the structure and thus facilitate the probability of a direct energy transfer from the photoexcited BODIPY to the closed form of the DTE. The energy transfer times found in the experiments are relatively unusual for orthogonally arranged FRET-pairs, but have already been reported for other comparable systems in the literature.[219,220]

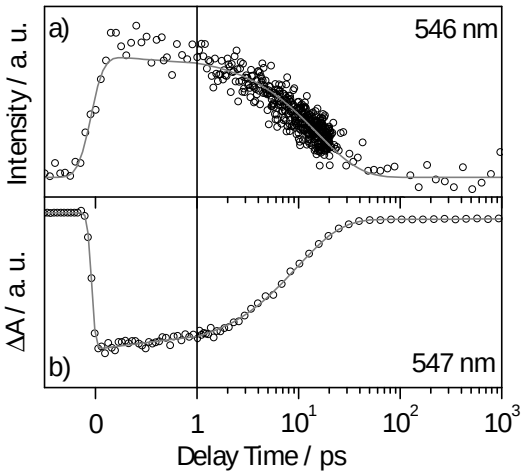

Figure 7.4: Comparison of time-resolved fluorescence and transient absorption traces of the *pss* of BODIPY-DTE recorded after photoexcitation at 504 nm and at 500 nm, respectively. In the Kerr shutter, the gate pulse (1300 nm) was generated in a two-stage OPA and was impinged with the generated fluorescence on the Kerr medium. In this case benzene was used as Kerr medium (Section 3.2) The fluorescence trace was corrected as stated in Figure 5.9.[181]

The results of the time-resolved measurements on the molecular dyad BODIPY-DTE show that the excited state lifetime from 4.3 ns for the open form is reduced by several orders of magnitude to 10 - 15 ps in the *pss*, caused by a pcFRET from the BODIPY to the DTE-moiety. The high efficiency in the dyad is most probably a result of the close proximity of 1.75 nm to the molecule fragments and vibrational motions causing a break in the orthogonal geometry.

7.2 Fulgimide

Many photochromic compounds exhibit no or only modest water-solubility. Due to sophisticated design, the here investigated molecule is a water-soluble representative of the class of photochromic fulgimides which is a derivative of the fulgides (Section 4.2.2).

Stationary measurements of the C and the Z-isomer of the water-soluble fulgimide are depicted in Figure 7.5. The absorption of the Z-isomer exhibits its maximum at 389 nm and the fluorescence is shifted about 140 nm in respect to the absorption maximum. In the visible range, the Z-isomer bears a small absorption that is most likely caused by residual C-isomer absorbance which has a maximum at 588 nm. For the C-isomer a second absorption at 317 nm is present accompanied by a prominent shoulder at the red side at around 376 nm, most likely stemming from Z-isomer absorbance. The fluorescence of the C-isomer is located in the NIR ($\lambda_{max} = 920$ nm), indicating complex excited state dynamics.

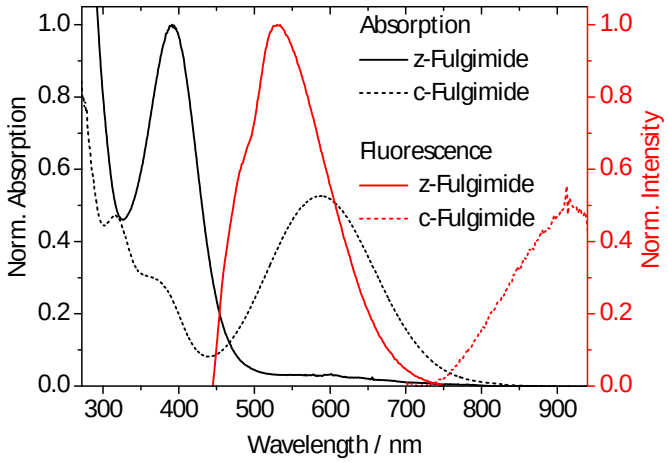

Figure 7.5: Stationary absorption and fluorescence spectra of the two isomers of the water-soluble fulgimide which take part in the cyclization reaction. The absorbance can be seen as mixture of both isomers. Measurements were performed and the data kindly provided by Chokri Boumrifak and Dr. Chavdar Slavov.[221]

The ring-closing (Z→C) reaction was investigated by means of ultrafast transient absorption spectroscopy. The transient absorption spectrum of the photoisomerization from the Z- to the C-isomer was generated by photoexciting the sample close to the absorption maximum at 388 nm (Figure 7.6). Furthermore, the sample was continuously illuminated with visible light to ensure photoexciting the Z-isomer and not photogenerated C-isomer. Figure 7.6 displays the ultrafast dynamics of the fulgimide where two strong positive signals are located below 370 nm and between 440 and 600 nm. Both signals are assigned to ESAs. Besides those, two negative signals are observed. The more

dominant signal, centered at 400 nm between the two ESA-signals, refers to the GSB of the Z-isomer. The weak signal above 600 nm is only visible in the sub-picosecond range and is assigned to the SE. As consequence of the photoinduced cyclization reaction, the formation of the C-isomer is observed, discernible on the timescale >10 ps by the photoinduced absorption at 590 nm and the remaining GSB of the Z-isomer.

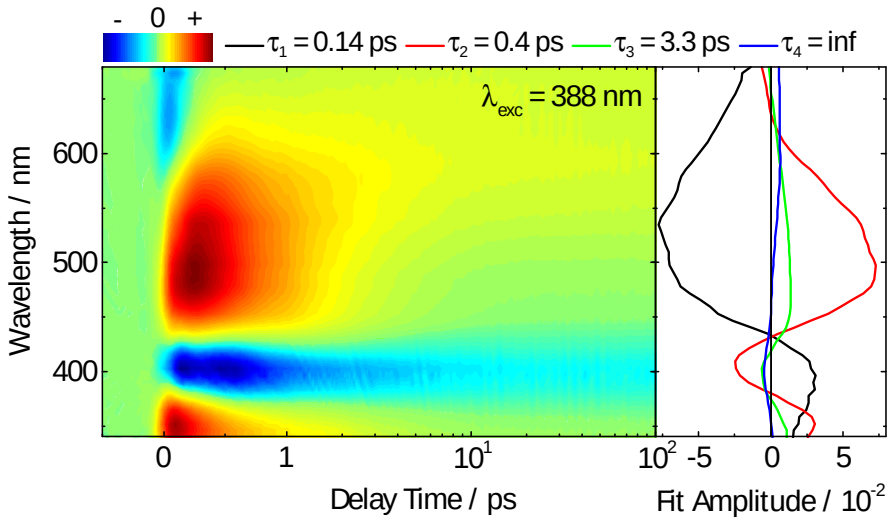

Figure 7.6: Transient absorption spectrum of the Z-isomer of the water-soluble fulgimide recorded after photoexcitation at 388 nm. Red indicates positive and blue negative absorbance changes. Measurements were performed and the data kindly provided by Chokri Boumrifak and Dr. Chavdar Slavov.[221]

The data were successfully fitted with three time constants and a fourth non-decaying time constant to describe the buildup of the C-isomer and the remaining signature of the Z-isomer. The formation of the GSB and of the ESA in the visible range are reflected by τ_1 (0.14 ps). Additionally, τ_1 seems to contribute to the decay of the SE (>575 nm), thus the time constant is associated with the relaxation in the Franck-Condon-region towards the conical intersection leading to significant spectral shifts of the ESA and the SE. Furthermore, τ_2 (0.4 ps) and τ_3 (3.3 ps) describe the decay of the GSB, SE and ESA, while τ_2 contributes with larger amplitudes compared to τ_3, indicating a biphasic decay of the excited state. The spectral characteristics of τ_2 and τ_3 exhibit high similarity, although small differences are observed. After transition through the conical intersection the Z-isomer molecule can relax to the ground state of either the C- or the Z-isomer. In case of relaxation to the C-isomer ground state, the ESA decays whereas the Z-isomer GSB remains. However, the relaxation to the Z-isomer ground state leads to the decay of both signals. Consequently, the time constant with larger GSB contributions (τ_2) should reflect a more dominant transition to the Z-isomer ground state. This is corroborated by the positive amplitudes of τ_3 at ~620 nm related to product absorption.

Indeed, a fourth infinite time constant displays the decay of the GSB and the product absorption of the C-isomer above 500 nm, resembling the vanishing Z-isomer absorption and the formation of the C-isomer absorption.

Many characteristics of the excited state dynamics can be derived by the signature of the SE. Unfortunately, the SE is mostly superimposed by the dominating ESA. Kerr shutter measurements were performed to elucidate the S_1-lifetime (Figure 7.7). For this purpose, the fulgimide was placed in a reservoir, which was continuously illuminated with visible light for the same reasons as in the transient absorption measurements stated above. During the entire measurement the sample was circularly pumped by a flow-through cuvette (Section 5.5.4). Fluorescence of the fulgimide was generated by photoexcitation at $\lambda_{exc} = 388$ nm. Subsequently, gated fluorescence was detected, resulting in the spectrum displayed in Figure 7.7 ranging from 439 nm to 609 nm from which an ultrafast decay of the excited state can be inferred.

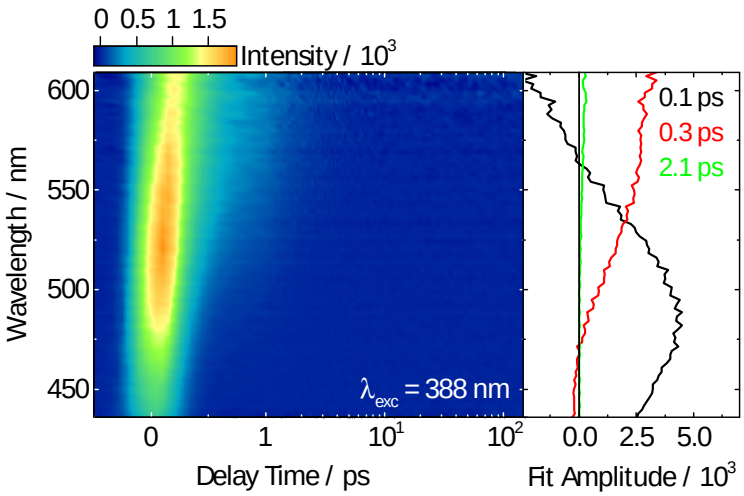

Figure 7.7: Time-resolved fluorescence spectrum of the ring-closing reaction of the water-soluble fulgimide recorded after photoexcitation at 388 nm. The DAS are shown next to the time-resolved fluorescence spectrum.[221]

The maximum of the time-resolved fluorescence at 530 nm is in good agreement with the one found in stationary measurements. The GLA of the time-resolved fluorescence provided three time constants. In the spectral region of the maximum the emission decays rapidly with the time constants of 0.1 ps and 0.3 ps (Figure 7.7, right) and a slower decay component at longer wavelengths. The decay of the fluorescence at longer wavelengths is described with two time constants (0.3 ps and 2.1 ps), implying a biphasic fluorescence decay. The necessity of a slower decay component is depicted in Figure 7.8, in which a distinguishable level of fluorescence can be observed after 1 ps. In addition, fluorescence signals at longer wavelengths increase with a delay of ~100 fs compared to

signals at higher energies, a consequence resulting from corrections concerning the GVD (Section 5.5.4). This appearance is assigned to a dynamic Stokes-shift which is reflected by the ultrafast component in the transient absorption measurement (Figure 7.6).

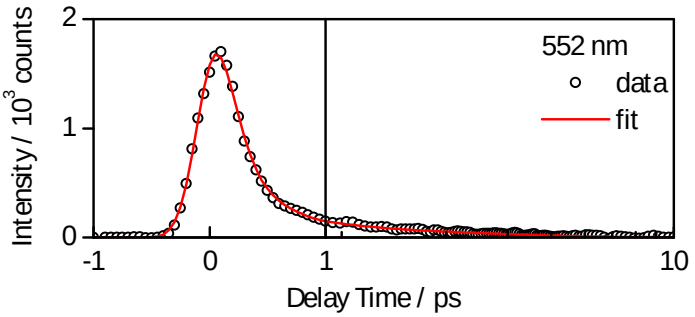

Figure 7.8: Fluorescence trace (black circles) at 552 nm recorded after photoexcitation at 388 nm and the corresponding fit (red line) resulting from a GLA with three time constants.

All three time constants are in reasonable agreement with those found in the GLA of the transient absorption measurement (Figure 7.6). The short time constant (τ_1 = 0.1 ps) reflects the relaxation from the Franck-Condon-region after photoexcitation into the S_1-state, while τ_2 (0.3 ps) and τ_3 (2.1 ps) describe the transition to the Z- and to the C-isomer ground state. These findings are in very good agreement to previously published data on similar compounds solved in acetonitrile.[222,223]

7.3 Dodecin

Dodecins are flavoproteins revealing an unique binding mode enclosing two flavins which are framed by two tryptophan residues in each of the six binding pockets. Besides flavin, dodecin binds specifically coenzyme A (CoA) as trimer in one of four binding pockets. With regard to its small size, dodecin can be seen as an efficient storage system, since one dodecin monomer binds one CoA and one flavin molecule.[63,224,225]

Dodecins can be classified into archaeal and bacterial flavoproteins, exhibiting differing structural properties from which different functional tasks are deduced. Archaeal dodecins, in particular from *Halobacterium salinarum* (*Hs*Dod) are well-studied and their function is largely understood.[63,224,225] The main function of the *Hs*Dod is the photoprotection of its cofactor Rf by ultrafast deactivation of the excited state. Staudt *et al.* postulated a deactivation mechanism which contains an electron transfer (ET) from the adjacent tryptophan residue on the photoexcited flavin.[64,65,199] Subsequent charge recombination of formed radicals yields the flavin ground state. On the other hand, the function of bacterial dodecins is yet not fully understood. Time-resolved spectroscopic characterization of FMN and Rf bound to *Mt*Dod and *Hh*Dod, respectively, unveiled a function similar to archaeal dodecins as storage and protection proteins for their prosthetic chromophores. Intriguingly, a less efficient protection of the incorporated flavin compared to archaeal dodecins is derived by longer excited state lifetimes found in the data analysis.[187] In addition, photoexcitation into the S_1-state revealed the evidence of SE which was not observed for *Hs*Dod:Rf. On the contrary, clear indications for an ET was found by means of a tryptophan cation signature which was not evident in bacterial dodecins.[64]

This work deals with the bacterial dodecin from *Mycobaterium tuberculosis* (*Mt*). *Mt* is the main cause of tuberculosis in humans. The cofactor of dodecin from *Mycobaterium tuberculosis* (*Mt*Dod) is flavin mononucleotide (FMN). Flavins are redox-active, prosthetic chromophores, consisting of an aromatic 7,8-dimethylisoalloxazine ring and an aliphatic part attached to the N10 position of the isoalloxazine. The heterocyclic isoalloxazine ring is the relevant redox and light sensing subunit of flavins. Physiologically important flavins besides FMN, are flavin adenine dinucleotide (FAD) and riboflavin (Rf, vitamin B2), which all differ in the aliphatic moiety at the N10 position. Recently, substantial dependence on the pH regarding the binding affinity of *Mt*Dod to its chromophore was reported.[187] The results gave rise to the assumption that bacterial dodecins act as FMN buffering device in which it takes up or releases its cofactor in regard to alter the conditions in their environment. In detail, an increased affinity of *Mt*Dod to FMN was found under acidic conditions (pH 5) compared to pH 7.5 close to

the physiological pH value. As a higher binding affinity is evident, shortened lifetimes should be observable in spectroscopic investigations.

7.3.1 Stationary Measurements

In general, flavins exhibit two absorption bands, where the lower-energy band corresponds to a photoexcitation into the S_1-state, whereas the high-energy band is assigned to the $S_0 \rightarrow S_2$-transition.[226,227]

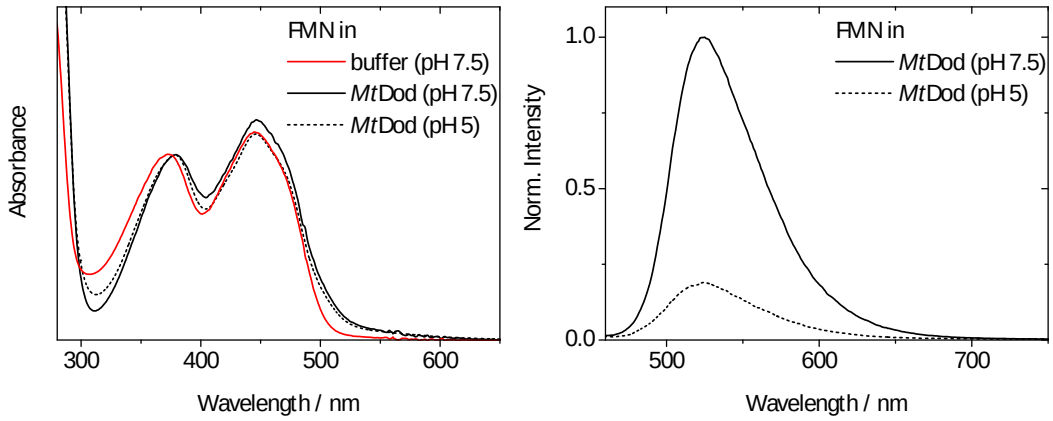

Figure 7.9: Left) Stationary absorption of free FMN (red line) and incorporated into *Mt*Dod at pH 7.5 (black line) and at pH 5 (dashed black line). The absorbances were normalized to the higher energy $S_0 \rightarrow S_2$-transition. Right) Stationary fluorescence of FMN incorporated into *Mt*Dod at pH 7.5 (black line) and at pH 5 (dashed black line).[187]

Free FMN in buffer (pH 7.5) and FMN bound to *Mt*Dod in buffer (pH 7.5 and pH 5) were characterized with stationary spectroscopy. For this purpose, UV/vis absorption spectra were recorded (Figure 7.9). Minor differences between the free chromophore and the one incorporated into *Mt*Dod can be seen, while a change in pH value entails only negligible alterations in absorption. The higher-energy $S_0 \rightarrow S_2$ transition with a maximum at 373 nm in case of the free flavin is about 7 nm red-shifted if incorporated into the dodecin, independent of the pH value. The $S_0 \rightarrow S_1$ band remains at the same spectral position. Indeed, a change in amplitude becomes visible. The redshift observed for *Mt*Dod:FMN compared to free FMN results with a high probability from the formation of hydrogen bonds to the respective amino acid residues in the binding pocket.[228] A shoulder at 480 nm, as it occurs in *Hs*Dod:Rf, is not recognizable here.[229] Nevertheless, the $S_0 \rightarrow S_1$-transition band at the red side is slightly broader for bound FMN than for free FMN. Furthermore, it can be seen that all compounds exhibit a higher low-energy absorption ($S_0 \rightarrow S_1$) compared to the high-energy absorption which is related to the $S_0 \rightarrow S_2$ transition.

Stationary fluorescence of *Mt*Dod:FMN at pH 5 is quenched to about 20% compared to fluorescence measured at pH 7.5, supporting the increased affinity to FMN under acidic conditions. The structure and the maximum of the fluorescence band remains mainly constant and is thus pH-independent.

7.3.2 Time-resolved Measurements

Figure 7.10 discloses absorbance changes after photoexcitation at 388 nm of free FMN (left) and bound to *Mt*Dod in pH 7.5 (middle) and pH 5 (right). The transient absorption spectrum of free FMN is distinguished by two long-lived negative and two positive signals. While the positive signals at 500 nm - 550 nm and above 640 nm are assigned to ESAs, occurring from transitions from S_1 to S_4 and S_3, respectively.[230]

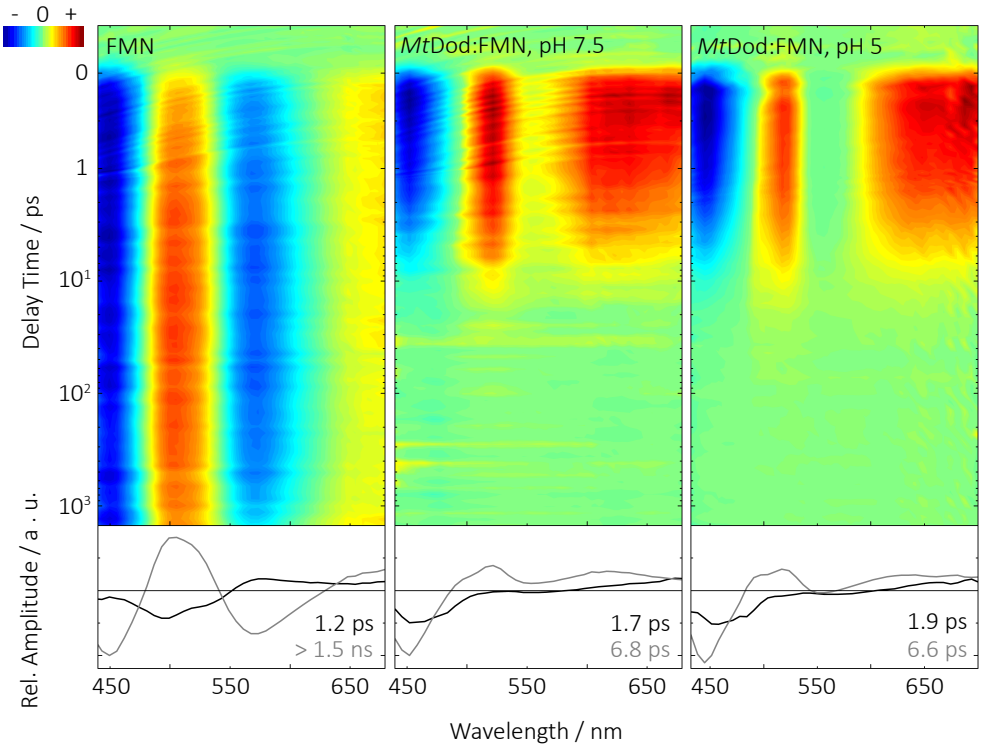

Figure 7.10: Transient absorption spectra recorded after photoexcitation at 388 nm of free FMN in buffer with a pH of 7.5 (left) and of FMN incorporated into *Mt*Dod in an aqueous buffer at pH 7.5 (middle) and pH 5 (right). Red indicates positive and blue negative absorbance changes. On the bottom the referring DAS are shown. A third time constant with small amplitudes was necessary to describe residual signals for the measurements on flavin bound to dodecin.[187]

Negative signals centered at 450 nm and between 540 and 610 nm refer to the GSB and SE, respectively. All signals are still visible after 1.5 ns indicating that FMN is still

in the excited state which is in accordance with the fluorescence lifetime of FMN of 4.4 ns.[231,232]

In contrast, lifetime signals for FMN bound in *Mt*Dod (Figure 7.10, middle and right) are dramatically shortened which is in accordance with previously recorded data on *Hs*Dod and dodecin from *Halorhodospira halophila* (*Hh*Dod).[64] For both, the GSB signal disappears after roughly 20 ps. The second difference is the missing SE signal which is most probably suppressed by larger positive signals. Astonishingly, an obvious alteration between the measurements at different pH values, as it was found for the stationary fluorescence, is indiscernible indicating that the electronic environment of FMN is unchanged at both pH conditions.

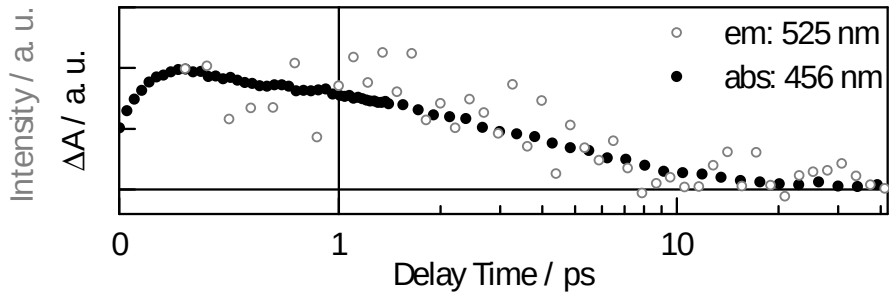

Figure 7.11: Time-resolved fluorescence trace (white-filled gray circles) at 525 nm and a normalized GSB signal (456 nm) of *Mt*Dod:FMN at pH 7.5 (black circles) recorded after photoexcitation at 400 nm and 388 nm, respectively. Delay times before time zero are not shown due to the large artifact. Fluorescence of *Mt*Dod:FMN vanishes after roughly 20 ps to an offset of about 20 % which is subtracted from the data, since it is most likely caused by free flavin.

For further clarification on the evidence of SE, ultrafast fluorescence measurements were carried out. For this purpose, *Mt*Dod:FMN was photoexcited at 400 nm and benzene-gated fluorescence was detected as described in Section 5.5.4. Figure 7.11 displays the fluorescence trace at the maximum of the stationary emission at 525 nm. For a guide to the eye, the GSB signal from Figure 7.9 (middle) was normalized accordingly, manifesting to a high degree of similarity the fluorescence decay. At this point, it shall be conceded that a certain level of long-lived fluorescence, most likely stemming from free FMN, was detected and subtracted from the data. GVD corrections were waived, since only one trace is displayed.

7.4 Concluding Remarks

This chapter introduces three different photoresponsive systems by means of two photochromic compounds and a flavin-binding protein, dodecin. Stationary absorption and fluorescence, as well as time-resolved measurements, in particular UV/vis-pump-vis-probe and Kerr shutter experiments were performed.

Stationary absorption measurements of the cooperative BODIPY-DTE in the open form and in the *pss* reveal absorbances which are composed of the isolated moieties. A pcFRET was inferred from shortened lifetimes observed in the pump-probe-experiments on the *pss*. In comparison to the experiment on the open form, in which the dyad can be viewed as electronically decoupled system, the donor fluorescence is not quenched by the DTE. Both TA measurements were supported via time-resolved fluorescence experiments. While the long-lived BODIPY emission occurring from BODIPY-DTE in its open state was detected with the TCSPC method, its time-resolution is insufficient for the rapid pcFRET mechanism. Therefore, BODIPY-DTE in the *pss* was photoexcited in the Kerr shutter. The subsequent detected fluorescence trace is highly similar to the GSB signal.

Secondly, the photochromic ring-closing reaction of a water-soluble indolylfulgimide was spectroscopically characterized. Transient absorption measurements as well as Kerr shutter experiments provided insight to this reaction. The photodynamics extracted from TA measurements unveil the relaxation from the excited state to the conical intersection. Moreover, relaxation to the ground state and the formation of the other isomer can be gathered from the results. First was confirmed by time-resolved fluorescence measurements with the help of the Kerr shutter. As the excited state lifetime cannot be fully deduced in transient absorption spectroscopy due to the superposition of several signals and the formation of the C-isomer, ultrafast fluorescence represented unambiguously the excited state dynamics. Again, substantial agreement between both measurements was found.

The last part of this chapter focused on the deactivation of the excited state of flavins bound to dodecin. In particular a pH dependent investigation is presented in which stationary measurements unveil a quenched fluorescence at pH 5 compared to emission recorded under almost physiological conditions. Surprisingly, these observations were not confirmed in transient absorption spectroscopy. Time-resolved data of FMN bound to dodecin show quenched lifetimes in contrast to measurements of free FMN which is in line with previously recorded data.

Intriguingly, stationary measurements exhibited a certain level of fluorescence of

*Mt*Dod:FMN which should be evident in time-resolved measurements, if this is originated from free FMN. However, no long-lived SE was found which indicates a homogeneous sample. Surprisingly, no signature of the SE was detected at all which contradicts the observed stationary fluorescence. The assumption that positive signals conceal the SE was tested in Kerr shutter measurements where only time-resolved fluorescence is detected. Indeed, a weak emission at pH 7.5 with high similarity to the lifetimes inferred from TA measurements was monitored.

Part IV

Conclusion

8

Conclusion and Outlook

The major aim of this work was the spectroscopic characterization of a novel antenna-photocage-system. In general, photolabile protecting groups (PPGs) are capable to mask the biological activity of an effector molecule which is covalently attached to the cage. Irradiation of the caged compound induces an irreversible photoreaction which yields the corresponding photoproduct and leads to the liberation of the biomolecule into its active state. Therefore, PPGs embody an approach to control biological systems with high spatial and temporal resolution. A promising possibility to intensify this control is given by the technique of two-photon absorption (2PA), enabling intrinsically high three-dimensional resolution caused by its quadratic dependence on the light intensity, which makes it only observable in focal points of high-power pulsed lasers. Moreover, the long-wavelength off-resonant photoexcitation in 2PA causes deeper sample penetration, while in 1PA the excitation beam is directly absorbed as it is incident on the material. Additionally to the high resolution and the deeper sample penetration, 2PA in the NIR provides the access to the "phototherapeutic window" (690 - 950 nm).

By now, the research field bears many potent photocages, but they exhibit only a modest two-photon response. Hence, the objective was to enhance the 2PA of a widely-used cage. Due to the favorable properties of coumarin-4-yl cages, DEACM was used, equipped with an antenna and therefore sensitized to 2PA. The approach is based on the fact that readily available fluorophores exhibit substantial 2PA. Consequently, ATTO 390, with a presumably large two-photon cross-section in comparison to prevailing cages, was coupled via a propargyllinker to DEACM. Once the antenna is excited, the energy is proposed to be transferred on DEACM which on the other hand shall be utilized to induce the solvent-assisted uncaging of the neurotransmitter glutamate. The successfully synthesized coumarin-based photocage, sensitized to 2PA by an antenna, was

characterized with stationary and time-resolved spectroscopic methods. In detail, the improved two-photon absorption, the energy transfer and the uncaging reaction were investigated.

Beforehand, the precursor DEACM-caged glutamate and its corresponding photoproduct DEACM-OH were spectroscopically characterized. UV/vis experiments on this compound shown in Section 6.1 unveiled slightly divergent spectral properties of the caged compound compared to the corresponding photoproduct with a minor red-shifted absorption of DEACM-Glu. Furthermore, continuous illumination of DEACM-Glu resulted in a hypsochromic shift of the absorption band related to the caged compound. The observation indicated a photoinduced reaction, although an unambiguous evidence of an uncaging reaction by the detection of the released glutamate could not be derived from these illumination experiments. In addition to stationary measurements, indications of a TICT-state were found in solvent-dependent transient absorption measurements.

Moreover, the antenna ATTO 390 was characterized by means of stationary and time-resolved methods (Section 6.2). While transient absorption measurements showed high similarities to data on coumarin, marked by relatively slow photodynamics, stationary measurements revealed a large Stokes-shift which offers a good overlap between the emission of ATTO 390 and the absorption of a DEACM molecule which is substituted at the C3 position.

On the basis of the findings in Section 6.1 the target molecule was modified by linking the glutamate to DEACM via a carbamate. Consequently, a photoreaction should cause a photodecarboxylation, which results in the formation of carbon dioxide. Its intense absorption band in the IR can be exploited as a marker to monitor the uncaging reaction.

Stationary absorption measurements of the triad composed of ATTO 390, DEACM and glutamate jointed via a carbamate (I+II+III, Figure 4.6) displayed an absorbance which most likely resembles the isolated fragments' absorbances. A closer look revealed a bathochromic shift of the short-wavelength absorption within the triad referring to the ATTO 390 absorption, indicating intramolecular interactions in an electronically decoupled system. In addition, the fluorescence of the triad compared to the corresponding photoproduct (I+II) was reduced.

2PA is quantified by the two-photon cross section which can be determined with several techniques (Section 2.4). Evidence of an increased 2PA was demonstrated by two-photon excited fluorescence (TPEF) experiments. Reference measurements on ATTO 390, DEACM-OH and I+II were conducted with rhodamine B, fluorescein and coumarin 307. Broadband fluorescence spectra of these compounds were obtained upon 2PA.

The 2PA was validated by excitation power-dependent measurements on rhodamine B and I+II, yielding an almost perfect quadratic dependence of the fluorescence intensity upon two-photon excitation. Broadband fluorescence spectra were recorded to exclude any misinterpretation caused by scattered excitation light or other perturbing signals. In addition, three reference compounds were used to diminish any uncertainties caused by the experimental setup. 2PA spectra of the reference compounds obtained from wavelength-dependent measurements display high similarity in spectral shape and magnitude compared to 2PA spectra from the literature, except of rhodamine B which exhibited values only half as large as stated in reference 67. Nonetheless, literature values of rhodamine B were reported with a substantially large error. Two-photon action cross sections inferred from TPEF experiments display an increased two-photon response at all wavelengths by the novel photocage compared to the common DEACM photocage. However, the fluorescence quantum yield (ϕ_{fl}) has to be considered. In first approximation, ϕ_{fl} upon one-photon excitation of the three compounds were determined, displaying the lowest ϕ_{fl} for the dyad I+II, consequently, its 2P response is presumably larger.

Evidence of an intramolecular energy transfer was provided by femtosecond UV/vis-pump-vis-probe experiments. The dyad (I+II) was photoexcited in a wavelength-selective fashion in order to predominantly address either I or II. On the basis of the absorbances of I and II, the absorption of I+II consists of the absorbances of both fragments. Hence, a photoexcitation at 475 nm should predominantly photoexcite the DEACM moiety (II). The obtained transient absorption spectrum gives rise to the assumption of a possible intramolecular charge transfer (ICT). Clear indications can be disclosed by a negative signal at longer wavelengths related to the SE of II which decays with a time constant of 2.6 ps, but a still persistent ground state bleach (GSB) of II. Within the first 2.6 ps the formation of a short-wavelength GSB is observed and assigned to I. A time constant of 130 ps describes the decay of both signals caused by the charge recombination and the repopulation of the ground state.

In contrast, an excitation wavelength at 365 nm was chosen in order to photoexcite I. Again, three negative signals are observed where the short-wavelength signal is related to the GSB of I. The second negative signal at longer wavelengths gave an indication for a direct photoexcitation of II, as it was assigned to the GSB of II. An intramolecular energy transfer (IET) could be observed with a time constant of ∼20 ps most likely accompanied by a subsequent ICT from to II to I. The experimental findings were corroborated by theoretical calculations, in particular by excited state analysis, revealing the charge transfer character of the dyad enabled by its stacked aggregate inferred as energetic minimum from ground state geometry optimizations.

The functionality of the antenna-photocage-system in terms of an uncaging reaction was investigated by recording absorbance spectra in the UV/vis- and in the IR-range during continuous illumination experiments. Additionally to I+II+III, a reference photocage without ATTO 390 (II+III) was measured under the same conditions to assess the direct influence of I. As a preliminary point, the introduction of ATTO 390 extends the triad's absorbance in the UV enabling a more efficient excitation over a broader wavelength-range, a fact which was exploited in the uncaging experiments. Photoexcitation at 365 nm displays the intense absorption of carbon dioxide in IR measurements upon photodecarboxylation for I+II+III and II+III. Indeed, a more efficient uncaging was detected for the photocage which is equipped with I. In addition, a more efficient uncaging was obtained for I+II+III than for II+III after photoexciting the samples at 420 nm, an observation which is assigned to the increased π-system within I+II+III. Absorption changes in the UV/vis during continuous illumination were perceived by a hypsochromic shift of the long-wavelength absorption band related to II within I+II+III, a finding which is in line with results from Section 6.1. Moreover, an increase in absorbance was noticeable which is in agreement with the extinction coefficient of I+II. Hence, an uncaging quantum yield (ϕ_u) of 1.5% was determined from continuous illumination experiments in the UV/vis. Comparative measurements of II+III revealed an one order of magnitude lower ϕ_u.

In a nutshell, a new photocage with the common DEACM and ATTO 390 which facilitates the 2PA, was successfully characterized with spectroscopic methods. In detail, increased 2PA of I+II compared to DEACM was found in TPEF measurements, insights to ultrafast photodynamics were provided by wavelength-dependent transient absorption measurements and successful uncaging of glutamate via a photodecarboxylation reaction was monitored in the IR.

The results of the antenna-photocage-system demonstrate the enhancement of 2PA by attachment of an antenna without negatively influencing the functionality of the uncaging process. In the next step, improvements of the investigated system aim to suppress the charge transfer character which is promoted by the stacked conformation enabled by the relatively long alkyl chain of ATTO 390. Recently, a dye similar to ATTO 390 without an alkyl chain was synthesized in the group of Prof. Dr. Heckel (Goethe-University, Frankfurt). By now, its coupling to the DEACM derivative was not successful, but it exhibits already promising results concerning the 2PA. The validation of this approach should further motivate the introduction of other antenna systems with increased two-photon cross sections, e.g. quantum dots to the photocage.

Different photoresponsive systems were examined by time-resolved spectroscopic tech-

niques. The ultrashort fluorescence of these systems was captured with a Kerr shutter setup (Section 5.5.4). Time-resolved fluorescence directly reflects the excited state lifetime which can also be disclosed by transient absorption measurements. Albeit, in pump-probe-experiments several signals may superimpose entailing a sophisticated deconvolution. Precise information on the excited state dynamics in the femtosecond- to picosecond-range can be gained with the Kerr shutter setup by recording fluorescence with high temporal resolution.

The first of the three investigated systems deals with a cooperative dyad exhibiting a highly-efficient pcFRET (photochromic Förster resonance energy transfer). Stationary absorption measurements on the cooperative BODIPY-DTE (borodipyrromethene-dithienylethene) in the open form and in the photostationary state (*pss*) clearly indicated that the dyad's absorbance consists most likely of the sum of the isolated fragments' absorbances. Moreover, the BODIPY donor exhibits very sharp absorbance and emission bands which are relatively close to each other, revealing a small Stokes-shift. Transient absorption experiments on the dyad in the open state and in the *pss* were carried out in order to investigate the ultrafast dynamics. A photoexcitation at 500 nm was chosen which predominantly addressed the BODIPY donor. The resulting spectrum of the open form was dominated by long-lived signals related to the electronically excited BODIPY, indicating an excited state lifetime larger than the investigated temporal range. The transient absorption spectrum of the *pss* exhibited a decay on the picosecond time scale, from which a pcFRET was derived. The *pss* BODIPY-DTE discloses a highly-conjugated system due to a closed form of the photochromic DTE. This facilitates an energy transfer from the photoexcited BODIPY to the DTE, leading to the reduced donor fluorescence. The transient absorption measurements were corroborated by time-resolved fluorescence experiments. A lifetime of 4.3 ns was deduced from the long-lived BODIPY emission when the dyad is in its open state with the technique of time-correlated single photon counting (TCSPC). As its time-resolution is insufficient for the rapid pcFRET mechanism, other techniques i.e. the Kerr shutter were required. Therefore, *pss* BODIPY-DTE was photoexcited at 504 nm in the Kerr shutter setup. The detected fluorescence decays with a time constant of 15 ps and exhibits high similarity to the GSB signal from transient absorption experiments.

Besides the BODIPY-DTE, a second photochromic compound was investigated. In particular, the photochromic ring-closing reaction of a water-soluble indolylfulgimide was spectroscopically characterized. Transient absorption measurements provided direct insight to the mechanism in which, after photoexcitation, the ultrafast movement out of the Franck-Condon-region and the fast biphasic relaxation of the molecule through the conical intersection was deduced. Time-resolved fluorescence measurements with the aid

of the Kerr shutter were performed, as the SE in transient absorption measurements was veiled due to the superposition of several signals. Global lifetime analysis of the broadband fluorescence captured with the Kerr shutter provided three time constants where the shortest reflects the relaxation out of the Franck-Condon-region towards the conical intersection. The fluorescence decay is described by two time constants (0.3 ps and 2.1 ps), indicating a biphasic transition to the electronic ground state. All three time constants exhibit essential agreement with those inferred from transient absorption measurements.

The excited state deactivation in flavoproteins, in detail the flavin-binding dodecin from *Mycobacterium tuberculosis* has been investigated with different spectroscopic techniques. Stationary fluorescence measurements at different pH values unveil a quenched emission at pH 5 compared to the one recorded under physiological conditions (pH 7.5). Conspicuously, these observations were not confirmed by transient absorption measurements as they exhibited high similarity in their dynamics and spectral signature. Moreover, a negative signal from the SE was not found. Still, the spectral signature related to the SE is most probably visible as a dip in the larger positive signals. The time-resolved fluorescence was investigated in Kerr shutter measurements in which weak emission at pH 7.5 was found. Moreover, the emission decay dynamics is in good agreement with the GSB signal from transient absorption measurements.

In total, ultrafast fluorescence of two photochromic systems and of a flavin bound to the protein dodecin was captured with a Kerr shutter setup. All three cases provide insight to the excited state lifetime and emphasize the findings of transient absorption measurements by unraveling the superimposed SE signals. Satisfactorily, the fluorescence dynamics are in good agreement with the excited state dynamics, which were obtained by transient absorption measurements, rendering the complementary results of both methods.

9

Zusammenfassung

Ein Hauptziel dieser Arbeit war die spektroskopische Charakterisierung einer neuartigen photolabilen Schutzgruppe (PPG, englisch für *photolabile protecting group*), welche sich durch eine zusätzliche Antenne von anderen PPGs unterscheidet. Im Allgemeinen sind PPGs, auch *Photocages* genannt, in der Lage, die Aktivität eines Effektormoleküls, das kovalent an die PPG gebunden ist, zu maskieren. Dieser Komplex wird als *Caged Compound* bezeichnet. Die Bestrahlung eines *Caged Compounds* induziert eine irreversible Photoreaktion zum entsprechenden Photoprodukt sowie zur Freisetzung des gebundenen Moleküls und somit in seinen aktiven Zustand. Hierdurch verkörpern PPGs einen vielversprechenden Ansatz zur Kontrolle von biologischen Systemen mit hoher räumlicher und zeitlicher Auflösung. Eine Möglichkeit, diese Kontrolle zu verbessern, bietet die Technik der Zwei-Photonen Absorption (2PA), welche durch ihre quadratische Abhängigkeit von der Lichtintensität eine intrinsisch hohe dreidimensionale Auflösung ermöglicht, so dass diese nur in Brennpunkten eines fokussierten leistungsstarken gepulsten Laserstrahls zu beobachten ist. Des Weiteren bewirkt die langwellige, nicht-resonante Photoanregung in der 2PA eine höhere Eindringtiefe, während in der Ein-Photonen Absorption der Anregungsstrahl absorbiert wird, sobald dieser auf das Material trifft. Zusätzlich bietet die 2PA im Infraroten den Zugang zum "phototherapeutischen Fenster"(690 - 950 nm) mittels Licht eines nicht zellschädigen Spektralbereichs.

Dieses Forschungsfeld hat bereits eine Vielzahl an Erfolg versprechenden *Photocages* hervorgebracht. Allerdings weisen diese mitunter nur eine geringe 2PA auf, weshalb die Motivation, eine PPG mit erhöhter 2PA zu entwickeln, bestärkt wurde. Hierzu wurde aufgrund seiner verheißungsvollen Eigenschaften die Cumarin-4-yl-Schutzgruppe (7-Diethylaminocumarin-4-yl)methyl (DEACM) als Basis verwendet, welche mit dem Fluorophor ATTO 390 ausgestattet wurde. Im Vergleich zu herkömmlichen PPGs weisen

einige kommerziell erhältliche Fluorophore einen substanziell größeren Zwei-Photonen-Einfangquerschnitt auf. Die erfolgreich synthetisierte Cumarin-basierte PPG mit mutmaßlich erhöhter 2PA wurde mit stationären und zeitaufgelösten spektroskopischen Methoden charakterisiert. Hierbei wurde die Zwei-Photonen-Absorption, der Energietransfer von der Antenne zur PPG sowie die Freisetzungsreaktion eines gebundenen Effektormoleküls untersucht.

Zuvor wurden die jeweiligen Molekülteile ATTO 390 sowie DEACM-geschütztes Glutamat (DEACM-Glu) isoliert betrachtet. Die Ergebnisse der letztgenannten Verbindung und des korrespondierenden Photoprodukts sind in Kapitel 6.1 dargestellt. Hierbei wies die Absorption von DEACM-Glu im UV/Vis-Bereich eine leichte Rotverschiebung im Vergleich zur Absorption des Photoprodukts auf. Darüber hinaus zeigten Absorptionsspektren unter kontinuierlicher Belichtung von DEACM-Glu eine hypsochrome Verschiebung, was ein eindeutiger Hinweis auf eine photoinduzierte Reaktion ist, jedoch nicht zwangsläufig einer Freisetzungsreaktion zugeordnet werden muss, da mit UV/vis Spektroskopie keine direkte Detektion von Glutamat erfolgen kann. Neben stationären Messungen wurden lösungsmittelabhängige transiente Absorptionsmessungen durchgeführt, die Hinweise auf einen verdrillten intramolekularen Ladungstransferzustand, einen sogenannten *TICT state* (englisch für *twisted intramolecular charge transfer*) gaben. Darüber hinaus wurde die Antenne ATTO 390 mittels stationärer und zeitaufgelöster Methoden (Kapitel 6.2) charakterisiert. Während transiente Absorptionsmessungen große Ähnlichkeiten zu Daten anderer Cumarine aufwiesen, die durch eine relativ langsame Photodynamik gekennzeichnet sind, zeigten stationäre Messungen eine große Stokes-Verschiebung, welche einen guten Überlapp zwischen der Emission von ATTO 390 und der Absorption eines DEACM-Moleküls, das an der C3-Position substituiert ist, zur Folge hat. Auf den Erkenntnissen aus Kapitel 6.1 basierend, wurde das Zielmolekül entsprechend modifiziert, indem eine Carbamatbindung zwischen DEACM und Glutamat eingeführt wurde. Diese besitzt den Vorteil, dass eine entsprechende Belichtung des Moleküls eine Photodecarboxylierung induziert und somit Kohlendioxid freigesetzt wird. Dieses zeichnet sich durch eine intensive Absorptionsbande im IR aus, welche als Marker für die Beobachtung der Freisetzungsreaktion verwendet werden kann. Die Absorption der Triade bestehend aus ATTO 390, DEACM und Glutamat (I+II+III) zeigt, dass diese höchstwahrscheinlich aus den Absorptionen der isolierten Fragmente besteht. Bei genauerer Betrachtung des Absorptionsspektrums ist eine bathochrome Verschiebung der kurzwelligen Absorption, die ATTO 390 zuzuordnen ist, erkennbar. Dies könnte bereits auf intramolekulare Wechselwirkungen im elektronisch entkoppelten System hinweisen. Des Weiteren wurde in stationären Fluoreszenzmessungen eine niedrigere Fluoreszenz der Triade im Vergleich zum korrespondierenden Photoprodukt

(I+II) gefunden.

Die Quantifizierung der 2PA wird durch den Zwei-Photonen-Einfangquerschnitt ausgedrückt, welcher mittels verschiedenster Techniken bestimmt werden kann (Kapitel 2.4). Der Nachweis der erhöhten 2PA wurde durch Zwei-Photonen-induzierte Fluoreszenz (TPEF, englisch für *two-photon excited fluorescence*) erbracht, eine Methode, durch die man über die Fluoreszenz nach Zwei-Photonen-Anregung auf den Zwei-Photonen-Einfangquerschnitt rückschließen kann. Hierzu wurden breitbandige Fluoreszenzspektren mittels 2PA von ATTO 390, DEACM-OH und I+II aufgenommen und mit Fluoreszenzspektren von Rhodamin B, Fluorescein und Cumarin 307 referenziert. Die 2PA wurde durch Messungen mit variierender Anregungsenergie an Rhodamin B und I+II bestätigt, welche eine fast perfekte quadratische Abhängigkeit der Fluoreszenzintensität nach vorangegangener 2PA widerspiegelten. 2PA-Spektren der Referenzverbindungen aus wellenlängenabhängigen Messungen besaßen große Übereinstimmung zu 2PA-Spektren aus der Literatur. Eine Ausnahme bildeten einige Werte des Zwei-Photonen-Einfangquerschnitts von Rhodamin B, die jedoch auch in der Literatur eine erhebliche Unsicherheit aufweisen.[67] Die Werte des Zwei-Photonen-Einfangquerschnitts von I+II waren über alle Wellenlängen hinweg größer als die von DEACM-OH. Allerdings muss bei der verwendeten Methode die Fluoreszenzquantenausbeute (ϕ_{fl}) berücksichtigt werden. In erster Näherung wurde ϕ_{fl} der drei Verbindungen nach Ein-Photonen Aktivierung bestimmt, wobei die Dyade I+II die niedrigste ϕ_{fl} der drei untersuchten Moleküle aufwies, wodurch ihre 2PA vermutlich noch größer ist.

Der Beweis eines intramolekularen Energietransfers von der Antenne zu DEACM erfolgte durch transiente Absorptionsspektroskopie. Hierfür wurde die Dyade (I+II) wellenlängenabhängig angeregt, um selektiv zum einen I und zum anderen II zu adressieren. Aufgrund der Annahme, dass die Absorption der Dyade sich aus den Absorptionen der jeweiligen Molekülteile zusammensetzt, sollte eine langwellige Photoanregung bei 475 nm die Photodynamik der DEACM-Einheit (II) widerspiegeln. Das transiente Absorptionsspektrum zeigte einen schnellen Zerfall der stimulierten Emission (SE) von II mit einer Zeitkonstante von 2.6 ps. Gleichzeitig jedoch ist das Grundzustandsbleichen (GSB, englisch für *ground state bleach*) von II weiterhin sichtbar. Innerhalb der ersten 2.6 ps wurde die Bildung eines kurzwelligen GSBs, welches I zugeordnet wurde, beobachtet. Dies deutete auf einen intramolekularen Ladungstransfer (ICT, englisch für *intramolecular charge transfer*) von II auf I hin. Die Ladungsrekombination und somit der Zerfall aller Signale erfolgt mit einer Zeitkonstante von ∼130 ps. Im Gegensatz dazu wurde mit einer Photoanregung bei 365 nm innerhalb der Dyade überwiegend I adressiert. Wiederum wurden drei negative Signale beobachtet, von denen das kurzwellige Signal dem GSB von I und das langwelligere negative Signal II zugeordnet wurde.

Das direkte Auftauchen des GSBs nach Photoanregung ließ eine direkte Photoanregung von II vermuten. Ein intramolekularer Energietransfer (IET, englisch für *intramolecular energy transfer*) konnte mit einer Zeitkonstante von ∼20 ps beobachtet werden, welcher wahrscheinlich von einem nachgelagerten ICT von II auf I begleitet wurde. Die experimentellen Ergebnisse wurden durch quantenchemische Rechnungen bestätigt, die den Ladungstransfercharakter der Dyade aufzeigten, der durch eine gestapelte Anordnung der π-Systeme ermöglicht wurde. Diese Konformation wurde als energetisches Minimum aus Optimierungen der Grundzustandsgeometrie abgeleitet.

Die Funktionalität des Antennen-Photocage-Systems wurde durch Aufnahme von Absorptionsspektren im UV/Vis- und IR-Bereich während kontinuierlicher Belichtung untersucht. Außerdem wurde unter den gleichen Bedingungen ein Referenzmolekül ohne den Farbstoff ATTO 390 (II+III) gemessen, woraus der direkte Einfluss von I abgeleitet werden konnte. Durch die Einführung von ATTO 390 an das DEACM-Molekül wird eine effizientere Absorption über einen breiteren Wellenlängenbereich ermöglicht. Für beide Verbindungen wurde nach Photoanregung bei 365 nm die intensive Absorption von Kohlendioxid aufgrund der Photodecarboxylierung detektiert. Tatsächlich wurde für die mit I ausgestattete PPG eine effizientere Freisetzung festgestellt. Diese Beobachtung wurde auch nach Photoanregung bei 420 nm gemacht, was dem erweiterten π-System innerhalb I+II+III zugeordnet wurde. Absorptionsänderungen während kontinuierlicher Belichtung wurden ebenfalls im UV/Vis-Bereich detektiert, in welchen eine hypsochrome Verschiebung der langwelligen Absorptionsbande, die II zuzuordnen ist, festgestellt wurde. Ein Befund, der mit den Ergebnissen aus Kapitel 6.1 übereinstimmt. Weiterhin konnte ein Anstieg der Absorption den Spektren entnommen werden, was mit dem erhöhten Extinktionskoeffizienten von I+II übereinstimmt. Eine Quantenausbeute der Freisetzungsreaktion (ϕ_u) von 1,5% konnte aus diesen Messungen ermittelt werden. Messungen an II+III ergaben eine um eine Größenordnung niedrigere ϕ_u im Vergleich zur Triade.

Zusammenfassend wurde eine neue PPG bestehend aus DEACM und ATTO 390, das die 2P-Absorption erhöht, erfolgreich mit spektroskopischen Methoden charakterisiert. Hierbei wurden in TPEF-Messungen eine im Vergleich zu DEACM-OH erhöhte 2PA von I+II gefunden. Informationen zur ultraschnellen Photodynamik wurden durch wellenlängenabhängige transiente Absorptionsmessungen erzielt und die erfolgreiche Freisetzung von Glutamat über eine Photodecarboxylierungsreaktion im IR-Bereich wurde detektiert.

Die Ergebnisse zum Antennen-Photocage-System zeigen auf, dass durch Anbringen einer Antenne die 2PA verbessert werden kann, ohne hierbei die Funktionalität des

Freisetzungsprozesses negativ zu beeinflussen. In einem nächsten Schritt zielen Verbesserungen des untersuchten Systems darauf ab, den Ladungstransfercharakter des Systems, welcher durch die gestapelte Konformation begünstigt wird, zu unterdrücken. Die energetisch günstige Konformation wird durch die relativ lange Alkylkette des ATTO 390 ermöglicht. Vor Kurzem wurde in der Gruppe von Prof. Heckel (Goethe-Universität, Frankfurt) ein ATTO 390-ähnlicher Farbstoff ohne Alkylkette synthetisiert. Bislang war die Kopplung an ein entsprechendes DEACM-Derivat nicht erfolgreich. Letzteres weist jedoch bereits vielversprechende Eigenschaften bezüglich der 2PA auf. Die Validierung dieses Ansatzes sollte die Einführung anderer Antennensysteme mit erhöhten Zwei-Photonen-Einfangquerschnitten, wie z.B. Quantenpunkte, weiter motivieren.

Der zweite Ergebnisteil dieser Arbeit konzentriert sich auf drei verschiedene Photosysteme, die sich durch sehr kurzlebige Fluoreszenz auszeichnen. Diese wurde mit einem Kerrschalter (Kapitel 5.5.4) aufgenommen. Die zeitaufgelöste Fluoreszenz stellt einen direkten Zugang zur Lebensdauer des angeregten Zustands dar. Diese kann zwar auch durch transiente Absorptionsmessungen ermittelt werden, ist allerdings unter Umständen durch die Superposition mehrerer Signale nur schwer bestimmbar. Genauere Informationen über die Dynamik im angeregten Zustand im Femto- bis Pikosekundenbereich können mit dem Kerrschalter durch Aufzeichnung der Fluoreszenz mit hoher zeitlicher Auflösung gewonnen werden.

Das erste der drei untersuchten Systeme umfasst eine kooperative Chromophor-Photoschalter-Dyade, welche einen hocheffizienten pcFRET (photochromen Förster-Resonanzenergietransfer) aufweist. Stationäre Absorptionsmessungen an der kooperativen BODIPY-DTE-Dyade (englisch für *boron-dipyrromethene-dithienylethene*) in der offenen Form und im photostationären Zustand (*pss* englisch für *photostationary state*) zeigten, dass die Absorption höchstwahrscheinlich aus den Absorptionen der isolierten Fragmente besteht. Weiterhin weist der BODIPY Donor eine sehr scharfe Absorptions- sowie Emissionsbande auf, zwischen welchen eine kleine Stokes-Verschiebung steht. Die Ultrakurzzeitdynamik der Dyade im offenen Zustand sowie im *pss* wurde mittels transienter Absorptionsspektroskopie untersucht. Photoanregung bei 500 nm adressierte hierbei überwiegend den BODIPY Donor. Das resultierende Spektrum der offenen Form wurde von langlebigen Signalen dominiert, welche dem elektronisch angeregten BODIPY zuzuordnen sind und eine Lebensdauer aufweisen, die größer als der untersuchte Zeitbereich ist. Zusätzlich wurde das transiente Absorptionsspektrum der Dyade im *pss* aufgenommen, aus welchem ein pcFRET aufgrund verkürzter Lebenszeiten der Differenzsignale abgeleitet wurde. Das BODIPY-DTE stellt im *pss* ein hochkonjugiertes System dar, welches durch die geschlossene Form des photochromen DTEs einen Energietransfer vom photoangeregten BODIPY zum DTE ermöglicht. Bei diesem Prozess wird die Fluoreszenz des

Donors um einige Größenordnungen reduziert. Beide transienten Absorptionsmessungen wurden durch zeitaufgelöste Fluoreszenzexperimente bestätigt. Eine Lebenszeit von 4.3 ns der langlebigen BODIPY-Emission im offenen Zustand wurde mit der Technik der zeitkorrelierten Einzelphotonenzählung (TCSPC, englisch für *time-correlated single photon counting*) gemessen. Da die Zeitauflösung der TCSPC-Methode für den schnellen FRET-Mechanismus nicht ausreicht, wurde das BODIPY-DTE im *pss* bei 504 nm im Kerrschalter angeregt. Die detektierte Fluoreszenztransiente zerfällt mit einer Zeitkonstante von etwa 15 ps und weist hierbei sehr hohe Ähnlichkeiten mit dem GSB-Signal aus transienten Absorptionsexperimenten auf.

Neben BODIPY-DTE wurde die photochrome Ringschlussreaktion eines wasserlöslichen Indolylfulgimids spektroskopisch charakterisiert. Transiente Absorptionsmessungen geben einen direkten Einblick in den Mechanismus der Reaktion, in welcher, nach Photoanregung, die Relaxation aus dem Franck-Condon Bereich und die schnelle biphasische Relaxation des Moleküls über die konische Durchschneidung abgeleitet werden kann. Zeitaufgelöste Fluoreszenzmessungen wurden mit Hilfe des Kerrschalters durchgeführt, da die SE in transienten Absorptionsmessungen durch die Überlagerung mehrerer Signale nicht vollständig zu erkennen war. Die globale Lebensdaueranalyse der mit dem Kerrschalter aufgenommenen Breitband-Fluoreszenz lieferte drei Zeitkonstanten, wobei die kürzeste die Relaxation in Richtung der konischen Durchschneidung reflektierte (0.1 ps). Die Repopulation des Grundzustands wurde mit zwei Zeitkonstanten von 0.3 ps und 2.1 ps beschrieben, was auf eine biphasische Relaxation in den elektronischen Grundzustand hindeutet. Alle drei Zeitkonstanten weisen wesentliche Übereinstimmung mit den Zeitkonstanten aus der globalen Lebensdaueranalyse der transienten Absorptionsmessungen auf.

Im dritten Teil wurde die Deaktivierung des elektronisch angeregten Zustands des flavinbindenden Dodecins aus *Mycobacterium tuberculosis* mit Hilfe von unterschiedlichen spektroskopischen Methoden charakterisiert. Stationäre Fluoreszenzmessungen bei unterschiedlichen pH-Werten zeigten bei pH 5 eine reduzierte Fluoreszenz verglichen zu der Fluoreszenz unter physiologischen Bedingungen (pH 7,5). Auffällig ist, dass diese Beobachtungen durch transiente Absorptionsmessungen nicht bestätigt werden konnten, da diese eine große Ähnlichkeit bezüglich der Dynamik und der spektralen Signatur zueinander besaßen. Ein negatives Signal, hervorgerufen durch die SE, wurde hierbei nicht gefunden. Allerdings konnte in den zerfallsassoziierten Spektren eine spektrale Signatur beobachtet werden, die auf eine SE hindeutete, welche allerdings mit größeren positiven Signalen überlagert ist. Dieser Aspekt wurde in einer Kerrschalter-Messung untersucht, in der eine schwache Emission bei pH 7,5 festgestellt werden konnte. Zusätzlich wies die Zerfallsdynamik der Emission eine ausgezeichnete Übereinstimmung

mit dem GSB-Signal aus den transienten Absorptionsmessungen auf.

Insgesamt wurde, zusätzlich zu stationären Absorptions- und Fluoreszenzmessungen sowie zeitaufgelösten transienten Absorptionsmessungen, ultraschnelle Fluoreszenz zweier photochromer Systeme und von Dodecin-gebundenem Flavin mit Hilfe eines Kerrschalters aufgenommen. Alle drei Fälle geben direkten Einblick in die Lebensdauer des angeregten Zustands und geben zusätzliche erläuternde Informationen zu den Ergebnissen der transienten Absorptionsspektroskopie. Des Weiteren ähnelte die Lebensdauer der Fluoreszenz in hoher Übereinstimmung der Dynamik des angeregten Zustands, die aus transienten Absorptionsmessungen abgeleitet wurde, wodurch die Komplementärität der Ergebnisse beider Methoden gezeigt wurde.

Bibliography

[1] Göppert-Mayer, M. Über Elementarakte mit Zwei Quantensprüngen. *Ann. Phys.* **1931**, *401*, 273–294.

[2] Kaiser, W.; Garrett, C. G. B. Two-Photon Excitation in $CaF_2 : Eu^{2+}$. *Phys. Rev. Lett.* **1961**, *7*, 229–232.

[3] Pawlicki, M.; Collins, H. A.; Denning, R. G.; Anderson, H. L. Two-Photon Absorption and the Design of Two-Photon Dyes. *Angew. Chem., Int. Ed.* **2009**, *48*, 3244–3266.

[4] McClain, W. M. Two-Photon Molecular Spectroscopy. *Acc. Chem. Res.* **1974**, *7*, 129–135.

[5] Goodman, L.; Rava, R. P. Two-Photon Spectra of Aromatic Molecules. *Acc. Chem. Res.* **1984**, *17*, 250–257.

[6] Parthenopoulos, D. A.; Rentzepis, P. M. Three-dimensional Optical Storage Memory. *Science* **1989**, *245*, 843–845.

[7] Strickler, J. H.; Webb, W. W. Three-dimensional Optical Data Storage in Refractive Media by Two-Photon Point Excitation. *Opt. Lett.* **1991**, *16*, 1780–1782.

[8] Glezer, E. N.; Milosavljevic, M.; Huang, L.; Finlay, R. J.; Her, T.-H.; Callan, J. P.; Mazur, E. Three-dimensional Optical Storage Inside Transparent Materials. *Opt. Lett.* **1996**, *21*, 2023–2025.

[9] Kawata, S.; Kawata, Y. Three-Dimensional Optical Data Storage Using Photochromic Materials. *Chem. Rev.* **2000**, *100*, 1777–1788.

[10] Walker, E.; Rentzepis, P. M. Two-Photon Technology: A New Dimension. *Nat. Photon.* **2008**, *2*, 406–408.

[11] Cumpston, B. H. et al. Two-Photon Polymerization Initiators for Three-dimensional Optical Data Storage and Microfabrication. *Nature* **1999**, *398*, 51–54.

[12] Maruo, S.; Nakamura, O.; Kawata, S. Three-dimensional Microfabrication with Two-Photon-absorbed Photopolymerization. *Opt. Lett.* **1997**, *22*, 132–134.

[13] LaFratta, C. N.; Fourkas, J. T.; Baldacchini, T.; Farrer, R. A. Multiphoton Fabrication. *Angew. Chem., Int. Ed.* **2007**, *46*, 6238–6258.

[14] Kawata, S.; Sun, H.-B.; Tanaka, T.; Takada, K. Finer Features for Functional Microdevices. *Nature* **2001**, *412*, 697–698.

[15] Farsari, M.; Chichkov, B. N. Two-Photon Fabrication. *Nat. Photon.* **2009**, *3*, 450–452.

[16] Zhou, W.; Kuebler, S. M.; Braun, K. L.; Yu, T.; Cammack, J. K.; Ober, C. K.; Perry, J. W.; Marder, S. R. An Efficient Two-Photon-generated Photoacid Applied to Positive-tone 3D Microfabrication. *Science* **2002**, *296*, 1106–1109.

[17] Ovsianikov, A.; Viertl, J.; Chichkov, B. N.; Oubaha, M.; MacCraith, B.; Sakellari, I.; Giakoumaki, A.; Gray, D.; Vamvakaki, M.; Farsari, M.; Fotakis, C. Ultra-low Shrinkage Hybrid Photosensitive Material for Two-Photon Polymerization Microfabrication. *ACS Nano* **2008**, *2*, 2257–2262.

[18] Weiß, T.; Hildebrand, G.; Schade, R.; Liefeith, K. Two-Photon Polymerization for Microfabrication of Three-dimensional Scaffolds for Tissue Engineering Application. *Eng. Life Sci.* **2009**, *9*, 384–390.

[19] Zhang, Y.-L.; Chen, Q.-D.; Xia, H.; Sun, H.-B. Designable 3D Nanofabrication by Femtosecond Laser Direct Writing. *Nano Today* **2010**, *5*, 435–448.

[20] Denk, W.; Strickler, J. H.; Webb, W. W. Two-Photon Laser Scanning Fluorescence Microscopy. *Science* **1990**, *248*, 73–76.

[21] Denk, W. Two-Photon Scanning Photochemical Microscopy: Mapping Ligand-gated Ion Channel Distributions. *Proc. Natl. Acad. Sci. USA* **1994**, *91*, 6629–6633.

[22] Williams, R. M.; Piston, D. W.; Webb, W. W. Two-Photon Molecular Excitation Provides Intrinsic 3-dimensional Resolution for Laser-based Microscopy and Microphotochemistry. *FASEB J.* **1994**, *8*, 804–813.

[23] Xu, C.; Zipfel, W.; Shear, J. B.; Williams, R. M.; Webb, W. W. Multiphoton Fluorescence Excitation: New Spectral Windows for Biological Nonlinear Microscopy. *Proc. Natl. Acad. Sci. USA* **1996**, *93*, 10763–10768.

[24] Denk, W.; Svoboda, K. Photon Upmanship: Why Multiphoton Imaging is More Than a Gimmick. *Neuron* **1997**, *18*, 351–357.

[25] Bewersdorf, J.; Pick, R.; Hell, S. W. Multifocal Multiphoton Microscopy. *Opt. Lett.* **1998**, *23*, 655–657.

[26] Shear, J. B. Multiphoton-Excited Fluorescence in Bioanalytical Chemistry. *Anal. Chem.* **1999**, *71*, 598A–605A.

[27] Helmchen, F.; Denk, W. Deep Tissue Two-photon Microscopy. *Nat. Methods* **2005**, *2*, 932–940.

[28] Zipfel, W. R.; Williams, R. M.; Webb, W. W. Nonlinear Magic: Multiphoton Microscopy in the Biosciences. *Nat. Biotechnol.* **2003**, *21*, 1369–1377.

[29] Leupold, D.; Kochevar, I. E. Multiphoton Photochemistry in Biological Systems Introduction. *Photochem. Photobiol.* **1997**, *66*, 562–565.

[30] Fisher, W. G.; Partridge Jr., W. P.; Dees, C.; Watcher, E. A. Simultaneous Two-Photon Activation of Type-I Photodynamic Therapy Agents. *Photochem. Photobiol.* **1997**, *66*, 141–155.

[31] Frederiksen, P. K.; Jorgensen, M.; Ogilby, P. R. Two-Photon Photosensitized Production of Singlet Oxygen. *J. Am. Chem. Soc.* **2001**, *123*, 1215–1221.

[32] Gao, D.; Agayan, R. R.; Xu, H.; Philbert, M. A.; Kopelman, R. Nanoparticles for Two-Photon Photodynamic Therapy in Living Cells. *Nano Lett.* **2006**, *6*, 2383–2386.

[33] Kim, S.; Ohulchanskyy, T. Y.; Pudavar, H. E.; Pandey, R. K.; Prasad, P. N. Organically Modified Silica Nanoparticles Co-encapsulating Photosensitizing Drug and Aggregation-enhanced Two-Photon Absorbing Fluorescent Dye Aggregates for Two-Photon Photodynamic Therapy. *J. Am. Chem. Soc.* **2007**, *129*, 2669–2675.

[34] Brown, S. Photodynamic Therapy: Two Photons are Better Than One. *Nat. Photon.* **2008**, *2*, 394–395.

[35] Collins, H. A.; Khurana, M.; Moriyama, E. H.; Mariampillai, A.; Dahlstedt, E.; Balaz, M.; Kuimova, M. K.; Drobizhev, M.; Yang, V. X. D.; Phillips, D.; Rebane, A.; Wilson, B. C.; Anderson, H. L. Blood-vessel Closure Using Photosensitizers Engineered for Two-Photon Excitation. *Nat. Photon.* **2008**, *2*, 420–424.

[36] Noguchi, J.; Nagaoka, A.; Watanabe, S.; Ellis-Davies, G. C. R.; Kitamura, K.; Kano, M.; Matsuzaki, M.; Kasai, H. In Vivo Two-Photon Uncaging of Glutamate Revealing the Structure-Function Relationships of Dendritic Spines in the Neocortex of Adult Mice. *J. Physiol.* **2011**, *589*, 2447–2457.

[37] Furuta, T.; Wang, S. S.-H.; Dantzker, J. L.; Dore, T. M.; Bybee, W. J.; Callaway, E. M.; Denk, W.; Tsien, R. Y. Brominated 7-Hydroxycoumarin-4-ylmethyls: Photolabile Protecting Groups with Biologically Useful Cross-Sections for Two Photon Photolysis. *Proc. Natl. Acad. Sci. USA* **1999**, *96*, 1193–1200.

[38] Lipp, P.; Niggli, E. Fundamental Calcium Release Events Revealed by Two-Photon Excitation Photolysis of Caged Calcium in Guinea-Pig Cardiac Myocytes. *J. Physiol.* **1998**, *508*, 801–809.

[39] Matsuzaki, M.; Ellis-Davies, G. C.; Nemoto, T.; Iino, M.; Kasai, H. Dendritic Spine Geometry is Critical for AMPA Receptor Expression in Hippocampal CA1 Pyramidal Neurons. *Nat. Neurosci.* **2001**, *4*, 1086–1092.

[40] Bort, G.; Gallavardin, T.; Ogden, D.; Dalko, P. I. From One-Photon to Two-Photon Probes: "Caged" Compounds, Actuators, and Photoswitches. *Angew. Chem., Int. Ed.* **2013**, *52*, 4526–4537.

[41] Waldeck, D. H. Photoisomerization Dynamics of Stilbenes. *Chem. Rev.* **1991**, *91*, 415–436.

[42] Görner, H.; Kuhn, H. J. *Cis-Trans Photoisomerization of Stilbenes and Stilbene-Like Molecules. In Advances in Photochemistry*; Wiley-VCH: New York, 1995.

[43] Rau, H.; Lueddecke, E. On the Rotation-Inversion Controversy on Photoisomerization of Azobenzenes. Experimental Proof of Inversion. *J. Am. Chem. Soc.* **1982**, *104*, 1616–1620.

[44] Bandara, H. M. D.; Burdette, S. C. Photoisomerization in Different Classes of Azobenzene. *Chem. Soc. Rev.* **2012**, *41*, 1809–1825.

[45] Irie, M. Diarylethenes for Memories and Switches. *Chem. Rev.* **2000**, *100*, 1685–1716.

[46] Irie, M.; Fukaminato, T.; Sasaki, T.; Tamai, N.; Kawai, T. A Digital Fluorescent Molecular Photoswitch. *Nature* **2002**, *420*, 759–760.

[47] Liang, Y. C.; Dvornikov, A. S.; Rentzepis, P. M. Nonvolatile Read-out Molecular Memory. **2003**, *100*, 8109–8112.

[48] Berberich, M.; Krause, A. M.; Orlandi, M.; Scandola, F.; Würthner, F. Toward Fluorescent Memories with Nondestructive Readout: Photoswitching of Fluorescence by Intramolecular Electron Transfer in a Diaryl Ethene-Perylene Bisimide Photochromic System. *Angew. Chem., Int. Ed.* **2008**, *47*, 6616–6619.

[49] Bossi, M. L.; Belov, V.; Polyakova, S.; Hell, S. W. Reversible Red Fluorescent Molecular Switches. *Angew. Chem., Int. Ed.* **2006**, *45*, 7462–7465.

[50] Fölling, J.; Polyakova, S.; Belov, V.; van Blaaderen, A.; Bossi, M. L.; Hell, S. W. Synthesis and Characterization of Photoswitchable Fluorescent Silica Nanoparticles. *Small* **2008**, *4*, 134–142.

[51] Tian, Z.; Wu, W.; Wan, W.; Li, A. D. Q. Single-Chromophore-Based Photoswitchable Nanoparticles Enable Dual-Alternating-Color Fluorescence for Unambiguous Live Cell Imaging. *J. Am. Chem. Soc.* **2009**, *131*, 4245–4252.

[52] Soh, N.; Yoshida, K.; Nakajima, H.; Nakano, K.; Imato, T.; Fukaminato, T.; Irie, M. A Fluorescent Photochromic Compound for Labeling Biomolecules. *Chem. Commun.* **2007**, *0*, 5206–5208.

[53] Zhu, L.; Wu, W.; Zhu, M.-Q.; Han, J. J.; Hurst, J. K.; Li, A. D. Q. Reversibly Photoswitchable Dual-Color Fluorescent Nanoparticles as New Tools for Live-Cell Imaging. *J. Am. Chem. Soc.* **2007**, *129*, 3524–3526.

[54] Zou, Y.; Yi, T.; Xiao, S.; Li, F.; Li, C.; Gao, X.; Wu, J.; Yu, M.; Huang, C. Amphiphilic Diarylethene as a Photoswitchable Probe for Imaging Living Cells. *J. Am. Chem. Soc.* **2008**, *130*, 15750–15751.

[55] Stafforst, T.; Hilvert, D. Kinetic Characterization of Spiropyrans in Aqueous Media. *Chem. Commun.* **2009**, *0*, 287–288.

[56] Sadovski, O.; Beharry, A. A.; Zhang, F.; Woolley, G. A. Spectral Tuning of Azobenzene Photoswitches for Biological Applications. *Angew. Chem., Int. Ed.* **2009**, *48*, 1484–1486.

[57] Kohl-Landgraf, J.; Braun, M.; Özçoban, C.; Gonçalves, D. P. N.; Heckel, A.; Wachtveitl, J. Ultrafast Dynamics of a Spiropyran in Water. *J. Am. Chem. Soc.* **2012**, *134*, 14070–14077.

[58] Heng, S.; McDevitt, C. A.; Stubing, D. B.; Whittall, J. J.; Thompson, J. G.; Engler, T. K.; Abell, A. D.; Monro, T. M. Microstructured Optical Fibers and Live Cells: A Water-Soluble, Photochromic Zinc Sensor. *Biomacromolecules* **2013**, *14*, 3376–3379.

[59] Özçoban, C.; Halbritter, T.; Steinwand, S.; Herzig, L.-M.; Kohl-Landgraf, J.; Askari, N.; Groher, F.; Fürtig, B.; Richter, C.; Schwalbe, H.; Suess, B.; Wachtveitl, J.; Heckel, A. Water-Soluble Py-BIPS Spiropyrans as Photoswitches for Biological Applications. *Org. Lett.* **2015**, *17*, 1517–1520.

[60] Steinwand, S.; Halbritter, T.; Rastädter, D.; Ortiz-Sánchez, J. M.; Burghardt, I.; Heckel, A.; Wachtveitl, J. Ultrafast Spectroscopy of Hydroxy-Substituted Azobenzenes in Water. *Chem. Eur. J.* **2015**, *21*, 15720–15731.

[61] Rutter, J.; Winge, D. R.; Schiffman, J. D. Succinate Dehydrogenase - Assembly, Regulation and Role in Human Disease. *Mitochondrion.* **2010**, *10*, 393–401.

[62] Thiagarajan, V.; Byrdin, M.; Eker, A. P. M.; Müller, P.; Brettel, K. Kinetics of Cyclobutane Thymine Dimer Splitting by DNA Photolyase Directly Monitored in the UV. *Proc. Natl. Acad. Sci. USA* **2011**, *108*, 9402–9407.

[63] Grininger, M.; Staudt, H.; Johansson, P.; Wachtveitl, J.; Oesterhelt, D. Dodecin is the Key Player in Flavin Homeostasis of Archaea. *J. Biol. Chem.* **2009**, *284*, 13068–13076.

[64] Staudt, H.; Oesterhelt, D.; Grininger, M.; Wachtveitl, J. Ultrafast Excited-State Deactivation of Flavins Bound to Dodecin. *J. Biol. Chem.* **2012**, *287*, 17637–17644.

[65] Staudt, H.; Hoesl, M. G.; Dreuw, A.; Serdjukow, S.; Oesterhelt, D.; Budisa, N.; Wachtveitl, J.; Grininger, M. Directed Manipulation of a Flavoprotein Photocycle. *Angew. Chem., Int. Ed.* **2013**, *52*, 8463–8466.

[66] Xu, C.; Webb, W. W. Measurement of Two-Photon Excitation Cross Sections of Molecular Fluorophores with Data from 690 to 1050 nm. *J. Opt. Soc. Am. B* **1996**, *13*, 481–491.

[67] Albota, M. A.; Xu, C.; Webb, W. W. Two-Photon Fluorescence Excitation Cross Sections of Biomolecular Probes from 690 to 960 nm. *Appl. Opt.* **1998**, *37*, 7352–7356.

[68] Birge, R. R.; Pierce, B. M. Semiclassical Time-dependent Theory of Two-Photon Spectroscopy. The Effect of Dephasing in the Virtual Level on the Two-Photon Excitation Spectrum of Isotachysterol. *Int. J. Quantum Chem.* **1986**, *29*, 639–656.

[69] Abe, M.; Chitose, Y.; Jakkampudi, S.; Thuy, P. T. T.; Lin, Q.; Van, B. T.; Yamada, A.; Oyama, R.; Sasaki, M.; Katan, C. Design and Synthesis of Two-Photon

Responsive Chromophores for Near-Infrared Light-Induced Uncaging Reactions. *Synthesis* **2017**, *49*, 3337–3346.

[70] König, K. Multiphoton Microscopy in Life Sciences. *J. Microsc.* **2000**, *200*, 83–104.

[71] Klán, P.; Šolomek, T.; Bochet, C. G.; Blanc, A.; Givens, R.; Rubina, M.; Popik, V.; Kostikov, A.; Wirz, J. Photoremovable Protecting Groups in Chemistry and Biology: Reaction Mechanisms and Efficacy. *Chem. Rev.* **2013**, *113*, 119–191.

[72] Brown, E. B.; Shear, J. B.; Adams, S. R.; Tsien, R. Y.; Webb, W. W. Photolysis of Caged Calcium in Femtoliter Volumes Using Two-Photon Excitation. *Biophys. J.* **1999**, *76*, 489–499.

[73] Pettit, D. L.; Wang, S. S.-H.; Gee, K. R.; Augustine, G. J. Chemical Two-Photon Uncaging: a Novel Approach to Mapping Glutamate Receptors. *Neuron* **1997**, *19*, 465–471.

[74] Ellis-Davies, G. C. R. Caged Compounds: Photorelease Technology for Control of Cellular Chemistry and Physiology. *Nat. Methods* **2007**, *4*, 619–628.

[75] Fichte, M. A. H.; Weyel, X. M. M.; Junek, S.; Schäfer, F.; Herbivo, C.; Goeldner, M.; Specht, A.; Wachtveitl, J.; Heckel, A. Three-Dimensional Control of DNA Hybridization by Orthogonal Two-Color Two-Photon Uncaging. *Angew. Chem., Int. Ed.* **2016**, *55*, 8948–8952.

[76] Gatterdam, V.; Ramadass, R.; Stoess, T.; Fichte, M. A. H.; Wachtveitl, J.; Heckel, A.; Tampé, R. Three-dimensional Protein Networks Guided by Two-Photon Activation. *Angew. Chem., Int. Ed.* **2014**, *53*, 5680–5684.

[77] Sinha, D. K.; Neveu, P.; Gagey, N.; Aujard, I.; Benbrahim-Bouzidi, C.; Le Saux, T.; Rampon, C.; Gauron, C.; Goetz, B.; Dubruille, S.; Baaden, M.; Volovitch, M.; Bensimon, D.; Vriz, S.; Jullien, L. Photocontrol of Protein Activity in Cultured Cells and Zebrafish with One- and Two-Photon Illumination. *ChemBioChem* **2010**, *11*, 653–663.

[78] Richers, M. T.; Amatrudo, J. M.; Olson, J. P.; Ellis-Davies, G. C. R. Cloaked Caged Compounds: Chemical Probes for Two-Photon Optoneurobiology. *Angew. Chem., Int. Ed.* **2017**, *56*, 193–197.

[79] Agarwal, H. K.; Janicek, R.; Chi, S.-H.; Perry, J. W.; Niggli, E.; Ellis-Davies, G. C. R. Calcium Uncaging with Visible Light. *J. Am. Chem. Soc.* **2016**, *138*, 3687–3693.

[80] Korzycka, K. A.; Bennett, P. M.; Cueto-Diaz, E. J.; Wicks, G.; Drobizhev, M.; Blanchard-Desce, M.; Rebane, A.; Anderson, H. L. Two-Photon Sensitive Protecting Groups Operating via Intramolecular Electron Transfer: Uncaging of GABA and Tryptophan. *Chem. Sci.* **2015**, *6*, 2419–2426.

[81] Atkins, P. W.; de Paula, J. *Physikalische Chemie*; Viley-VCH: New York, 2006.

[82] Rumi, M.; Perry, J. W. Two-Photon Absorption: an Overview of Measurements and Principles. *Adv. Opt. Photonics* **2010**, *2*, 451–518.

[83] Albota, M. et al. Design of Organic Molecules with Large Two-Photon Absorption Cross Sections. *Science* **1998**, *281*, 1653–1656.

[84] Cueto-Diaz, E. J.; Picard, S.; Chevasson, V.; Daniel, J.; Hugues, V.; Mongin, O.; Genin, E.; Blanchard-Desce, M. Cooperative Dyads for Two-Photon Uncaging. *Org. Lett.* **2015**, *17*, 102–105.

[85] Gascón-Moya, M.; Pejoan, A.; Izquierdo-Serra, M.; Pittolo, S.; Cabré, G.; Hernando, J.; Alibés, R.; Gorostiza, P.; Busqué, F. An Optimized Glutamate Receptor Photoswitch with Sensitized Azobenzene Isomerization. *J. Org. Chem.* **2015**, *80*, 9915–9925.

[86] Sperber, P.; Penzkofer, A. S_0–S_n Two-Photon Absorption Dynamics of Rhodamine Dyes. *Opt. Quantum Electron.* **1986**, *18*, 381–401.

[87] Tutt, L. W.; Boggess, T. F. A Review of Optical Limiting Mechanisms and Devices Using Organics, Fullerenes, Semiconductors and Other Materials. *Prog. Quantum Electron.* **1993**, *17*, 299–338.

[88] Sutherland, R. L. *Handbook of Nonlinear Optics*; Marcel Dekker: New York, 1996.

[89] Chapple, P. B.; Staromlynska, J.; Hermann, J. A.; McKay, T. J.; McDuff, R. G. Single-Beam Z-Scan: Measurement Techniques and Analysis. *J. Nonlinear Opt. Phys. Mater.* **1997**, *6*, 251–293.

[90] van Stryland, E. W.; Sheik-Bahae, M. *"Z-Scan" in Characterization Techniques and Tabulations for Organic Nonlinear Optical Materials*; Marcel Dekker: New York, 1998.

[91] Kamada, K.; Matsunaga, K.; Yoshino, A.; Ohta, K. Two-Photon-Absorption-Induced Accumulated Thermal Effect on Femtosecond Z-Scan Experiments Studied with Time-Resolved Thermal-Lens Spectrometry and its Simulation. *J. Opt. Soc. Am. B* **2003**, *20*, 529–537.

[92] Lakowicz, J. R. *Principles of Fluorescence Spectroscopy*; Springer US: Boston, 2006.

[93] Kasha, M. Characterization of Electronic Transitions in Complex Molecules. *Discuss. Faraday Soc.* **1950**, *9*, 14–19.

[94] Valeur, B.; Berberan-Santos, M. N. *Molecular Fluorescence. Principles and Applications*; Wiley-VCH: New York, 2012.

[95] Sauer, M.; Hofkens, J.; Enderlein, J. *Handbook of Fluorescence Spectroscopy and Imaging. From Single Molecules to Ensembles*; Wiley-VCH: New York, 2011.

[96] Fluorescence-related publications; Date of Access: 15$^{\text{th}}$ August 2018; https://apps.webofknowledge.com.

[97] Haken, H.; Wolf, H. C. *Molekülphysik und Quantenchemie*; Springer Verlag: Berlin, Heidelberg, New York, 2006.

[98] Klán, P.; Wirz, J. *Photochemistry of Organic Compounds: From Concepts to Practice*; Wiley-VCH: New York, 2009.

[99] Beer, M.; Longuet-Higgins, H. C. Anomalous Light Emission of Azulene. *J. Chem. Phys.* **1955**, *23*, 1390–1391.

[100] Leupin, W.; Wirz, J. Low-Lying Electronically Excited States of Cycl[3.3.3]azine, a Bridged 12π-Perimeter. *J. Am. Chem. Soc.* **1980**, *102*, 6068–6075.

[101] Leupin, W.; Magde, D.; Persy, G.; Wirz, J. 1,4,7-Triazacycl[3.3.3]azine: Basicity, Photoelectron Spectrum, Photophysical Properties. *J. Am. Chem. Soc.* **1986**, *108*, 17–22.

[102] Kropp, J. L.; Stanley, C. C. The Temperature Dependence of Ovalene Fluorescence. *Chem. Phys. Lett.* **1971**, *9*, 534–538.

[103] Amirav, A.; Even, U.; Jortner, J. Intermediate Level Structure in the S_2 State of the Isolated Ultracold Ovalene Molecule. *Chem. Phys. Lett.* **1980**, *69*, 14–17.

[104] Nickel, B. Delayed Fluorescence from Upper Excited Singlet States S_n (n>1) of the Aromatic Hydrocarbons 1,2-Benzanthracene, Fluoranthene, Pyrene, and Chrysene in Methylcyclohexane. *Helv. Chim. Acta* **1978**, *61*, 198–222.

[105] Nickel, B.; Karbach, H.-J. Complete Spectra of the Delayed Luminescence from Aromatic Compounds in Liquid Solutions: on the Observability of Direct Radiative Triplet–Triplet Annihilation. *Chem. Phys.* **1990**, *148*, 155–182.

[106] Demas, J. N. *Excited-State Lifetime Measurements*; Academic Press: New York, 1983.

[107] O'Connor, D. V.; Phillips, D. *Time-correlated Single Photon Counting*; Academic Press: London, 1984.

[108] Becker, W. *Advanced Time-correlated Single Photon Counting Techniques. Springer Series in Chemical Physics, Vol. 81*; Springer Verlag: Berlin, Heidelberg, New York, 2005.

[109] Lemmetyinen, H.; Tkachenko, N. V.; Valeur, B.; Hotta, J.-I.; Ameloot, M.; Ernsting, N. P.; Gustavsson, T.; Boens, N. Time-Resolved Fluorescence Methods. *Pure Appl. Chem.* **2014**, *86*, 1969–1998.

[110] Heinz, B. Alte Photoreaktionen in Neuem Licht - Ultraschnelle Spektroskopie an Fulgimiden und Photolabilen Schutzgruppen. Ph.D. thesis, Ludwig-Maximilians-Universität München, 2008.

[111] Schmidt, B. Femtosekunden-Fluoreszenzspektroskopie Photoisomerisierender Moleküle. Ph.D. thesis, Ludwig-Maximilians-Universität München, 2004.

[112] Arzhantsev, S.; Maroncelli, M. Design and Characterization of a Femtosecond Fluorescence Spectrometer Based on Optical Kerr Gating. *Appl. Spectrosc.* **2005**, *59*, 206–220.

[113] Eom, I.; Joo, T. Polar Solvation Dynamics of Coumarin 153 by Ultrafast Time-Resolved Fluorescence. *J. Chem. Phys.* **2009**, *131*, 244507.

[114] Schmidt, B.; Laimgruber, S.; Zinth, W.; Gilch, P. A Broadband Kerr Shutter for Femtosecond Fluorescence Spectroscopy. *Appl. Phys. B* **2003**, *76*, 809–814.

[115] Nikogosyan, D. N. Beta Barium Borate (BBO) A Review of its Properties and Applications. *Appl. Phys. A* **1991**, *52*, 359–368.

[116] Boyd, R. *Nonlinear Optics*; Academic Press: London, 2008.

[117] Shen, Y. R. *The Principles of Nonlinear Optics*; Wiley-VCH: New York, 2002.

[118] Schanz, R.; Kovalenko, S. A.; Kharlanov, V.; Ernsting, N. P. Broad-Band Fluorescence Upconversion for Femtosecond Spectroscopy. *Appl. Phys. Lett.* **2001**, *79*, 566–568.

[119] Demtröder, W. *Laserspektroskopie: Grundlagen und Techniken*; Springer Verlag: Berlin, Heidelberg, New York, 2007.

[120] Schäfer, B. *Lehrbuch für Experimentalphysik, Optik*; H. Niedrig, Walter de Gruyter: Berlin, New York, 1993.

[121] Zinth, W.; Körner, H. J. *Physik 3 Optik, Quantenphänomene und Aufbau der Atome*; Oldenbourg: München Wien, 1998.

[122] Silfvast, W. T. *Laser Fundamentals*; Cambridge University Press: Cambridge, 2000.

[123] Trojanowski, P. Breitbandige, Zeitaufgelöste Spektroskopie als Empfindliche Methode zur Beobachtung von Biomolekularer Dynamik. Ph.D. thesis, Goethe-Universität Frankfurt, 2014.

[124] Duguay, M. A. The Ultrafast Optical Kerr Shutter. *Prog. Opt.* **1976**, *14*, 161–193.

[125] Takeda, J.; Nakajima, K.; Kurita, S.; Tomimoto, S.; Saito, S.; Suemoto, T. Time-Resolved Luminescence Spectroscopy by the Optical Kerr-Gate Method Applicable to Ultrafast Relaxation Processes. *Phys. Rev. B.* **2000**, *62*, 10083–10087.

[126] Herrmann, J.; Wilhelmi, B. *Laser für Ultrakurze Lichtimpulse*; Physik-Verlag: Weinheim, 1984.

[127] Appavoo, K.; Sfeir, M. Y. Enhanced Broadband Ultrafast Detection of Ultraviolet Emission Using Optical Kerr Gating. *Rev. Sci. Instrum.* **2014**, *85*, 055114.

[128] Aber, J. E.; Newstein, M. C.; Garetz, B. A. Femtosecond Optical Kerr Effect Measurements in Silicate Glasses. *J. Opt. Soc. Am. B* **2000**, *17*, 120–127.

[129] Kalpouzos, C.; Lotshaw, W. T.; McMorrow, D.; Kenney-Wallace, G. A. Femtosecond Laser-induced Kerr Responses in Liquid Carbon Disulfide. *J. Phys. Chem.* **1987**, *91*, 2028–2030.

[130] Kinoshita, S.; Ozawa, H.; Kanematsu, Y.; Tanaka, I.; Sugimoto, N.; Fujiwara, S. Efficient Optical Kerr Shutter for Femtosecond Time-Resolved Luminescence Spectroscopy. *Rev. Sci. Instrum.* **2000**, *71*, 3317–3322.

[131] Neelakandan, M.; Pant, D.; Quitevis, E. L. Reorientational and Intermolecular Dynamics in Binary Liquid Mixtures of Hexafluorobenzene and Benzene: Femtosecond Optical Kerr Effect Measurements. *Chem. Phys. Lett.* **1997**, *265*, 283–292.

[132] Goeldner, M.; Givens, R. S. *Dynamic Studies in Biology: Phototriggers, Photoswitches and Caged Biomolecules*; Wiley-VCH: New York, 2005.

[133] Mayer, G.; Heckel, A. Biologically Active Molecules with a "Light Switch". *Angew. Chem., Int. Ed.* **2006**, *45*, 4900–4921.

[134] Bochet, C. G.; Blanc, A. *Photolabile Protecting Groups in Organic Synthesis. In Handbook of Synthetic Photochemistry*; Viley-VCH: New York, 2010; pp 417–447.

[135] Brieke, C.; Rohrbach, F.; Gottschalk, A.; Mayer, G.; Heckel, A. Light-Controlled Tools. *Angew. Chem., Int. Ed.* **2012**, *51*, 8446–8476.

[136] Ankenbruck, N.; Courtney, T.; Naro, Y.; Deiters, A. Optochemical Control of Biological Processes in Cells and Animals. *Angew. Chem., Int. Ed.* **2018**, *57*, 2768–2798.

[137] Kumpulainen, T.; Lang, B.; Rosspeintner, A.; Vauthey, E. Ultrafast Elementary Photochemical Processes of Organic Molecules in Liquid Solution. *Chem. Rev.* **2017**, *117*, 10826–10939.

[138] Tamai, N.; Miyasaka, H. Ultrafast Dynamics of Photochromic Systems. *Chem. Rev.* **2000**, *100*, 1875–1890.

[139] Rautio, J.; Meanwell, N. A.; Di, L.; Hageman, M. J. The Expanding Role of Prodrugs in Contemporary Drug Design and Development. *Nat. Rev. Drug. Discov.* **2018**, *17*, 559–578.

[140] Barltrop, J. A.; Schofield, P. Photosensitive Protecting Groups. *Tetrahedron Lett.* **1962**, *16*, 697–699.

[141] Engels, J.; Schlaeger, E.-J. Synthesis, Structure, and Reactivity of Adenosine Cyclic 3',5'-phosphate-benzyltriesters. *J. Med. Chem.* **1977**, *20*, 907–911.

[142] Dienes, A.; Shank, C. V.; Trozzolo, A. M. Evidence for Exciplex Laser Action in Coumarin Dyes by Measurements of Stimulated Fluorescence. *Appl. Phys. Lett.* **1970**, *17*, 189–191.

[143] Schimitschek, E. J.; Trias, J. A.; Hammond, P. R.; Atkins, R. L. Laser Performance and Stability of Fluorinated Coumarin Dyes. *Opt. Commun.* **1974**, *11*, 352–355.

[144] Givens, R. S.; Matuszewski, B. Photochemistry of Phosphate Esters: An Effecient Method for Generation of Electrophiles. *J. Am. Chem. Soc.* **1984**, *106*, 6860–6861.

[145] Furuta, T. *Coumarin-4-ylmethyl Phototriggers. In Dynamic Studies in Biology*; Viley-VCH: New York, 2005.

[146] Hagen, V.; Bendig, J.; Frings, S.; Eckardt, T.; Helm, S.; Reuter, D.; Kaupp, U. B. Highly Efficient and Ultrafast Phototriggers for cAMP and cGMP by Using Long-Wavelength UV/Vis-Activation. *Angew. Chem., Int. Ed.* **2001**, *40*, 1045–1048.

[147] Menge, C.; Heckel, A. Coumarin-Caged dG for Improved Wavelength-Selective Uncaging of DNA. *Org. Lett.* **2011**, *13*, 4620–4623.

[148] Rodrigues-Correia, A.; Weyel, X. M. M.; Heckel, A. Four Levels of Wavelength-Selective Uncaging for Oligonucleotides. *Org. Lett.* **2013**, *15*, 5500–5503.

[149] Ohtsuki, T.; Kanzaki, S.; Nishimura, S.; Kunihiro, Y.; Sisido, M.; Watanabe, K. Phototriggered Protein Syntheses by Using (7- Diethylaminocoumarin-4-yl)methoxycarbonyl-caged aminoacyl tRNAs. *Nat. Commun.* **2016**, *7*, 12501.

[150] Herzig, L.-M.; Elamri, I.; Schwalbe, H.; Wachtveitl, J. Light-Induced Antibiotic Release from a Coumarin-Caged Compound on the Ultrafast Timescale. *Phys. Chem. Chem. Phys.* **2017**, *19*, 14835–14844.

[151] Goguen, B. N.; Aemissegger, A.; Imperiali, B. Sequential Activation and Deactivation of Protein Function Using Spectrally Differentiated Caged Phosphoamino Acids. *J. Am. Chem. Soc.* **2011**, *133*, 11038–11041.

[152] Abu-Eittah, R. H.; El-Tawil, B. A. H. The Electronic Absorption Spectra of Some Coumarins. A Molecular Orbital Treatment. *Can. J. Chem.* **1985**, *63*, 1173–11179.

[153] Moore, T. A.; Harter, M. L.; Song, P.-S. Ultraviolet Spectra of Coumarins and Psoralens. *J. Mol. Spectrosc.* **1971**, *40*, 144–157.

[154] Schade, B.; Hagen, V.; Schmidt, R.; Herbrich, R.; Krause, E.; Eckardt, T.; Bendig, J. Deactivation Behavior and Excited-State Properties of (Coumarin-4-yl) methyl Derivatives. 1. Photocleavage of (7-Methoxycoumarin-4-yl)methyl-Caged Acids with Fluorescence Enhancement. *J. Org. Chem.* **1999**, *64*, 9109–9117.

[155] Eckardt, T.; Hagen, V.; Schade, B.; Schmidt, R.; Schweitzer, C.; Bendig, J. Deactivation Behavior and Excited-State Properties of (Coumarin-4-yl)methyl Derivatives. 2. Photocleavage of Selected (Coumarin-4-yl)methyl-Caged Adenosine Cyclic 3′,5′-Monophosphates with Fluorescence Enhancement. *J. Org. Chem.* **2002**, *67*, 703–710.

[156] Liu, X.; Cole, J. M.; Xu, Z. Substantial Intramolecular Charge Transfer Induces Long Emission Wavelengths and Mega Stokes Shifts in 6-Aminocoumarins. *J. Phys. Chem. C* **2017**, *121*, 13274–13279.

[157] Hansen, M. J.; Velema, W. A.; Lerch, M. M.; Szymanski, W.; Feringa, B. L. Wavelength-Selective Cleavage of Photoprotecting Groups: Strategies and Applications in Dynamic Systems. *Chem. Soc. Rev.* **2015**, *44*, 3358–3377.

[158] Nag, A.; Bhattacharyya, K. Role of Twisted Intramolecular Charge Transfer in the Fluorescence Sensitivity of Biological Probes: Diethylaminocoumarin Laser Dyes. *Chem. Phys. Lett.* **1990**, *169*, 12–16.

[159] Singha, S.; Kim, D.; Roy, B.; Sambasivan, S.; Moon, H.; Rao, A. S.; Kim, J. Y.; Joo, T.; Park, J. W.; Rhee, Y. M.; Wang, T.; Kim, K. H.; Shin, Y. H.; Jung, J.; Ahn, K. H. A Structural Remedy Toward Bright Dipolar Fluorophores in Aqueous Media. *Chem. Sci.* **2015**, *6*, 4335–4342.

[160] Phukan, S.; Saha, M.; Pal, A. K.; Bhasikuttan, A. C.; Mitra, S. Intramolecular Charge Transfer in Coumarin Based Donor-Acceptor Systems: Formation of a New Product Through Planar Intermediate. *J. Photochem. Photobiol. A* **2015**, *303-304*, 67–79.

[161] Schmidt, R.; Geissler, D.; Hagen, V.; Bendig, J. Kinetics Study of the Photocleavage of (Coumarin-4-yl)methyl Esters. *J. Phys. Chem. A* **2005**, *109*, 5000–5004.

[162] Schmidt, R.; Geissler, D.; Hagen, V.; Bendig, J. Mechanism of Photocleavage of (Coumarin-4-yl)methyl Esters. *J. Phys. Chem. A* **2007**, *111*, 5768–5774.

[163] Herzig, L.-M. Molekulare Dynamik der Freisetzung eines photolabil geschützten Antibiotikums. Ph.D. thesis, Goethe-Universität Frankfurt, 2018.

[164] van Wilderen, L. J. G. W.; Neumann, C.; Rodrigues-Correia, A.; Kern-Michler, D.; Mielke, N.; Reinfelds, M.; Heckel, A.; Bredenbeck, J. Picosecond Activation of the DEACM Photocage Unravelled by VIS-Pump-IR-Probe Spectroscopy. *Phys. Chem. Chem. Phys.* **2017**, *19*, 6487–6496.

[165] Chitose, Y.; Abe, M.; Furukawa, K.; Lin, J.-Y.; Lin, T.-C.; Katan, C. Design and Synthesis of a Caged Carboxylic Acid with a Donor-π-Donor Coumarin Structure: One-Photon and Two-Photon Uncaging Reactions Using Visible and Near-Infrared Lights. *Org. Lett.* **2017**, *19*, 2622–2625.

[166] Kamatham, N.; Da Silva, J. P.; Givens, R. S.; Ramamurthy, V. Melding Caged Compounds with Supramolecular Containers: Photogeneration and Miscreant Behavior of the Coumarylmethyl Carbocation. *Org. Lett.* **2017**, *19*, 3588–3591.

[167] Jakob, A. Synthese von Zwei-Photonen-Schutzgruppen für Oligonukleotide und Peptide. Ph.D. thesis, Goethe-Universität Frankfurt, 2018.

[168] Hammer, C. A.; Falahati, K.; Jakob, A.; Klimek, R.; Burghardt, I.; Heckel, A.; Wachtveitl, J. Sensitized Two-Photon Activation of Coumarin Photocages. *J. Phys. Chem. Lett.* **2018**, *9*, 1448–1453.

[169] Curtis, D. R.; Watkins, J. C. The Excitation and Depression of Spinal Neurones by Structurally Related Amino Acids. *J. Neurochem.* **1960**, *6*, 117–141.

[170] Buhr, F.; Kohl-Landgraf, J.; tom Dieck, S.; Hanus, C.; Chatterjee, D.; Hegelein, A.; Schuman, E. M.; Wachtveitl, J.; Schwalbe, H. Design of Photocaged Puromycin for Nascent Polypeptide Release and Spatiotemporal Monitoring of Translation. *Angew. Chem., Int. Ed.* **2015**, *54*, 3717–3721.

[171] Hirshberg, Y.; Fischer, E. Photochromism and Reversible Multiple Internal Transitions in Some Spiropyrans at Low Temperatures. Part I. *J. Chem. Soc.* **1954**, *0*, 297–303.

[172] Giordano, L.; Jovin, T. M.; Irie, M.; Jares-Erijman, E. A. Diheteroarylethenes as Thermally Stable Photoswitchable Acceptors in Photochromic Fluorescence Resonance Energy Transfer (pcFRET). *J. Am. Chem. Soc.* **2002**, *124*, 7481–7489.

[173] Fukaminato, T.; Umemoto, T.; Iwata, Y.; Yokojima, S.; Yoneyama, M.; Nakamura, S.; Irie, M. Photochromism of Diarylethene Single Molecules in Polymer Matrices. *J. Am. Chem. Soc.* **2007**, *129*, 5932–5938.

[174] van der Molen, S. J.; Liao, J.; Kudernac, T.; Agustsson, J. S.; Bernard, L.; Calame, M.; van Wees, B. J.; Feringa, B. L.; Schönenberger, C. Light-Controlled Conductance Switching of Ordered Metal-Molecule-Metal Devices. *Nano Lett.* **2009**, *9*, 76–80.

[175] Fihey, A.; Perrier, A.; Browne, W. R.; Jacquemin, D. Multiphotochromic molecular systems. *Chem. Soc. Rev.* **2015**, *44*, 3719–3759.

[176] Woodward, R. B.; Hoffmann, R. Stereochemistry of Electrocyclic Reactions. *J. Am. Chem. Soc.* **1965**, *87*, 395–397.

[177] Woodward, R. B.; Hoffmann, R. The Conservation of Orbital Symmetry. *Angew. Chem., Int. Ed.* **1969**, *8*, 781–853.

[178] Hoffmann, R.; Woodward, R. B. Orbital Symmetry Control of Chemical Reactions. *Science* **1970**, *167*, 825–831.

[179] Fukaminato, T.; Doi, T.; Tamaoki, N.; Okuno, K.; Ishibashi, Y.; Miyasaka, H.; Irie, M. Single-Molecule Fluorescence Photoswitching of a

Diarylethene−Perylenebisimide Dyad: Non-Destructive Fluorescence Readout. *J. Am. Chem. Soc.* **2011**, *133*, 4984–4990.

[180] Natali, M.; Giordani, S. Molecular Switches as Photocontrollable "Smart" Receptors. *Chem. Soc. Rev.* **2012**, *41*, 4010–4029.

[181] Schweighöfer, F.; Dworak, L.; Hammer, C. A.; Gustmann, H.; Zastrow, M.; Rück-Braun, K.; Wachtveitl, J. Highly Efficient Modulation of FRET in an Orthogonally Arranged BODIPY–DTE Dyad. *Sci. Rep.* **2016**, *6:28638*.

[182] Heller, H. G.; Langen, J. R. Photochromic Heterocyclic Fulgides. Part 3. The Use of (E)-α-(2,5-dimethyl-3-furylethylidene)(isopropylidene)succinic anhydride as a Simple Convenient Chemical Actinometer. *J. Chem. Soc., Perkin Trans. 2* **1981**, *0*, 341–343.

[183] Santiago, A.; Becker, R. S. Photochromic Fulgides. Spectroscopy and Mechanism of Photoreactions. *J. Am. Chem. Soc.* **1968**, *90*, 3654–3658.

[184] Yokoyama, Y. Fulgides for Memories and Switches. *Chem. Rev.* **2000**, *100*, 1717–1740.

[185] Chen, X.; Islamova, N. I.; Garcia, S. P.; DiGirolamo, J. A.; Lees, W. J. Synthesis and Optical Properties of Aqueous Soluble Indolylfulgimides. *J. Org. Chem.* **2009**, *74*, 6777–6783.

[186] Schweighöfer, F. Dynamik von Energietransferprozessen in Photoschaltbaren Molekularen Dyaden. Ph.D. thesis, Goethe-Universität Frankfurt, 2017.

[187] Bourdeaux, F.; Hammer, C. A.; Vogt, S.; Schweighöfer, F.; Nöll, G.; Wachtveitl, J.; Grininger, M. Flavin Storage and Sequestration by *Mycobacterium Tuberculosis* Dodecin. *ACS Infect. Dis.* **2018**, *4*, 1082–1092.

[188] Crosby, J. N., G. A. und Demas Measurement of Photoluminescence Quantum Yields. A Review. *J. Phys. Chem.* **1971**, *75*, 991–1024.

[189] Williams, A. T. R.; Winfield, S. A.; Miller, J. N. Relative Fluorescence Quantum Yields Using a Computer-Controlled Luminescence Spectrometer. *Analyst* **1983**, *108*, 1067–1071.

[190] Ware, W. R.; Rothman, W. Relative Fluorescence Quantum Yields Using an Integrating Sphere. The Quantum Yield of 9,10-diphenylanthracene in Cyclohexane. *Chem. Phys. Lett.* **1976**, *39*, 449–453.

[191] The Nobel Prize in Physics 2018; Date of Access: 15th October 2018; https://www.nobelprize.org/prizes/physics/2018/summary/.

[192] *CPA-Series 2110, User's Manual*; Clark-MXR.

[193] Tamura, K.; Haus, H.; Ippen, E. Self-Starting Additive Pulse Mode-Locked Erbium Fibre Ring Laser. *Electron. Lett.* **1992**, *28*, 2226–2228.

[194] *Tsunami, Mode-locked Ti:sapphire Laser, User's Manual*; Spectra-Physics.

[195] *Millenia V, Diode-Pumped, CW Visible Laser, User's Manual*; Spectra-Physics.

[196] *Spitfire Ace, Ultrafast Amplifier, User's Manual*; Spectra-Physics.

[197] Reuß, A. Functional Dynamics of Ribonucleic Acids. Ph.D. thesis, Goethe-Universität Frankfurt, 2016.

[198] Steinwand, S. Conformational Control of Organic Molecules by Azobenzene-Based Photoswitches – A Spectroscopic Study. Ph.D. thesis, Goethe-Universität Frankfurt, 2016.

[199] Staudt, H. Kurzzeitspektroskopische Untersuchungen an Flavoproteinen: Photoprotektion von Flavinen in Dodecinen und Erste Schritte der Peptidfaltung. Ph.D. thesis, Goethe-Universität Frankfurt, 2012.

[200] Fork, R. L.; Shank, C. V.; Hirlimann, C.; Yen, R.; Tomlinson, W. J. Femtosecond White-light Continuum Pulses. *Opt. Lett.* **1983**, *8*, 1–3.

[201] Slavov, C.; Hartmann, H.; Wachtveitl, J. Implementation and Evaluation of Data Analysis Strategies for Time-Resolved Optical Spectroscopy. *Anal. Chem.* **2015**, *87*, 2328–2336.

[202] Ernsting, N. P.; Breffke, J.; Vorobyev, D. Y.; Duncan, D.; Pfeffer, I. Subpicosecond Fluorescence Evolution of Amino-Cyano-Stilbenes in Methanol: Polar Solvation Obeys Continuum Theory Without Evidence of Twisting. *Phys. Chem. Chem. Phys.* **2008**, *10*, 2043–2049.

[203] Sajadi, M.; Dobryakov, A. L.; Garbin, E.; Ernsting, N. P.; Kovalenko, S. A. Time-Resolved Fluorescence Spectra of Cis-Stilbene in Hexane and Acetonitrile. *Chem. Phys. Lett.* **2010**, *489*, 44–47.

[204] von Sellmeier, W. Zur Erklärung der Abnormen Farbenfolge im Spectrum Einiger Substanzen. *Ann. Phys.* **1871**, *219*, 272–282.

[205] Preat, J.; Jacquemin, D.; Wathelet, V.; André, J.-M.; Perpète, E. A. TD-DFT Investigation of the UV Spectra of Pyranone Derivatives. *J. Phys. Chem. A* **2006**, *110*, 8144–8150.

[206] Winters, B. H.; Mandelberg, H. I.; Mohr, W. B. Photochemical Products in Coumarin Laser Dyes. *Appl. Phys. Lett.* **1974**, *25*, 723–725.

[207] Banal, J. L.; Kondo, T.; Veneziano, R.; Bathe, M.; Schlau-Cohen, G. S. Photophysics of J-Aggregate-Mediated Energy Transfer on DNA. *J. Phys. Chem. Lett.* **2017**, *8*, 5827–5833.

[208] Howes, P.; Green, M.; Levitt, J.; Suhling, K.; Hughes, M. Phospholipid Encapsulated Semiconducting Polymer Nanoparticles: Their Use in Cell Imaging and Protein Attachment. *J. Am. Chem. Soc.* **2010**, *132*, 3989–3996.

[209] Barooah, N.; Mohanty, J.; Pal, H.; Bhasikuttan, A. C. Non-Covalent Interactions of Coumarin Dyes With Cucurbit[7]uril Macrocycle: Modulation of ICT to TICT State Conversion. *Org. Biomol. Chem.* **2012**, *10*, 5055–5062.

[210] Pinheiro, A. V.; Baptista, P.; Lima, J. C. Light Activation of Transcription: Photocaging of Nucleotides for Control over RNA Polymerization. *Nucleic Acids Res* **2008**, *36*, e90.

[211] Herbivo, C.; Omran, Z.; Revol, J.; Javot, H.; Specht, A. Synthesis and Characterization of Cell-Permeable Caged Phosphates that Can Be Photolyzed by Visible Light or 800 nm Two-Photon Photolysis. *ChemBioChem* **2013**, *14*, 2277–2283.

[212] Goegan, B.; Terzi, F.; Bolze, F.; Cambridge, S.; Specht, A. Synthesis and Characterization of Photoactivatable Doxycycline Analogues Bearing Two-Photon-Sensitive Photoremovable Groups Suitable for Light-Induced Gene Expression. *ChemBioChem* **2018**, *19*, 1341–1348.

[213] Frisch, M. J. et al. Gaussian 09, Revision D.01. 2013.

[214] Brinzer, T.; Berquist, E. J.; Ren, Z.; Dutta, S.; Johnson, C. A.; Krisher, C. S.; Lambrecht, D. S.; Garrett-Roe, S. Ultrafast Vibrational Spectroscopy (2D-IR) of CO_2 in Ionic Liquids: Carbon Capture From Carbon Dioxide's Point of View. *J. Chem. Phys.* **2015**, *142*, 212425.

[215] Falk, M.; Miller, A. G. Infrared Spectrum of Carbon Dioxide in Aqueous Solution. *Vib. Spectrosc.* **1992**, *4*, 105–108.

[216] Schaden, S.; Haberkorn, M.; Frank, J.; Baena, J. R.; Lendl, B. Direct Determination of Carbon Dioxide in Aqueous Solution Using Mid-Infrared Quantum Cascade Lasers. *Appl. Spectrosc.* **2004**, *58*, 667–670.

[217] Straub, S.; Brünker, P.; Lindner, J.; Vöhringer, P. An Iron Complex with a Bent, O-Coordinated CO_2 Ligand Discovered by Femtosecond Mid-Infrared Spectroscopy. *Angew. Chem., Int. Ed.* **2018**, *57*, 5000–5005.

[218] Schweighöfer, F.; Dworak, L.; Braun, M.; Zastrow, M.; Wahl, J.; Burghardt, I.; Rück-Braun, K.; Wachtveitl, J. Vibrational Coherence Transfer in an Electronically Decoupled Molecular Dyad. *Sci. Rep.* **2015**, *5:9368*.

[219] Langhals, H.; Esterbauer, A. J.; Walter, A.; Riedle, E.; Pugliesi, I. Förster Resonant Energy Transfer in Orthogonally Arranged Chromophores. *J. Am. Chem. Soc.* **2010**, *132*, 16777–16782.

[220] Nalbach, P.; Pugliesi, I.; Langhals, H.; Thorwart, M. Noise-Induced Förster Resonant Energy Transfer Between Orthogonal Dipoles in Photoexcited Molecules. *Phys. Rev. Lett.* **2012**, *108*, 218302.

[221] Slavov, C.; Boumrifak, C.; Hammer, C. A.; Trojanowski, P.; Chen, X.; Lees, W. J.; Wachtveitl, J.; Braun, M. The Ultrafast Reactions in the Photochromic Cycle of Water-Soluble Fulgimide Photoswitches. *Phys. Chem. Chem. Phys.* **2016**, *18*, 10289–10296.

[222] Heinz, B.; Malkmus, S.; Laimgruber, S.; Dietrich, S.; Schulz, C.; Rück-Braun, K.; Braun, M.; Zinth, W.; Gilch, P. Comparing a Photoinduced Pericyclic Ring Opening and Closure: Differences in the Excited State Pathways. *J. Am. Chem. Soc.* **2007**, *129*, 8577–8584.

[223] Draxler, S.; Brust, T.; Malkmus, S.; Koller, F. O.; Heinz, B.; Laimgruber, S.; Schulz, C.; Dietrich, S.; Rück-Braun, K.; Zinth, W.; Braun, M. Ultrafast Reaction Dynamics of the Complete Photo Cycle of an Indolylfulgimide Studied by Absorption, Fluorescence and Vibrational Spectroscopy. *J. Mol. Liq.* **2008**, *141*, 130–136.

[224] Grininger, M.; Zeth, K.; Oesterhelt, D. Dodecins: a Family of Lumichrome Binding Proteins. *J. Mol. Biol.* **2006**, *357*, 842–857.

[225] Grininger, M. The Function of the Halophilic Dodecin. Ph.D. thesis, Ludwig-Maximilians-Universität München, 2008.

[226] Stanley, R. J.; Jang, H. Electronic Structure Measurements of Oxidized Flavins and Flavin Complexes Using Stark-Effect Spectroscopy. *J. Phys. Chem. A* **1999**, *103*, 8976–8984.

[227] Stanley, R. J.; MacFarlane IV, A. W. Ultrafast Excited State Dynamics of Oxidized Flavins: Direct Observations of Quenching by Purines. *J. Phys. Chem. A* **2000**, *104*, 6899–6906.

[228] Sikorska, E.; Khmelinskii, I. V.; Worrall, D. R.; Koput, J.; Sikorski, M. Spectroscopy and Photophysics of Iso- and Alloxazines: Experimental and Theoretical Study. *J. Fluoresc.* **2004**, *14*, 57–64.

[229] Staudt, H. Kurzzeitspektroskopische Untersuchungen an Flavoproteinen: Photoprotektion von Flavinen in Dodecinen und erste Schritte der Peptidfaltung. Ph.D. thesis, Goethe-Universität Frankfurt, 2012.

[230] MacFarlane IV, A. W.; Stanley, R. J. Evidence of Powerful Substrate Electric Fields in DNA Photolyase: Implications for Thymidine Dimer Repair. *Biochemistry* **2001**, *40*, 15203–15214.

[231] Wahl, P.; Auchet, J. C.; Visser, A. J. W. G.; Müller, F. Time-Resolved Fuorescence of Flavin Adenine Dinucleotide. *FEBS Lett.* **1974**, *44*, 67–70.

[232] Visser, A. J. W. G.; Müller, F. Time-Resolved Fuorescence on Flavins and Flavoproteins. *Methods Enzymol.* **1980**, *66*, 373–385.

Scientific Contributions

Publications

- Bordeaux, F.; Hammer, C. A.; Vogt, S.; Schweighöfer, F.; Nöll, G.; Wachtveitl, J.; Grininger, M. Flavin Storage and Sequestration by Mycobacterium Tuberculosis Dodecin. *ACS Infect. Dis.* **2018**, *4*, 1082-1092.

- Hammer, C. A.; Falahati, K.; Jakob, A.; Klimek, R.; Burghardt, I.; Heckel, A.; Wachtveitl, J. Sensitized Two-Photon Activation of Coumarin Photocages. *J. Phys. Chem. Lett.* **2018**, *9*, 1448-1453.

- Schweighöfer, F.; Dworak, L.; Hammer, C. A.; Gustmann, H.; Zastrow, M.; Rück-Braun, K.; Wachtveitl, J. Highly Efficient Modulation of FRET in an Orthogonally Arranged BODIPY-DTE Dyad. *Sci. Rep.* **2016**, *6:28638*.

- Slavov, C.; Boumrifak, C.; Hammer, C. A.; Trojanowski, P.; Chen, X.; Lees, W. J.; Wachtveitl, J.; Braun M. The Ultrafast Reactions in the Photochromic Cycle of Water-soluble Fulgimide Photoswitches. *Phys. Chem. Chem. Phys.* **2016**, *18*, 10289-10296.

Poster Contributions

- "*Ultrafast Deactivation Processes in Flavin-binding Proteins*", 27^{th} PhotoIUPAC **2018**, Dublin (Ireland)

- "*Molecular Insights into a Novel Two-photon Sensitized Coumarin Caged Glutamate Triad*", Design and Light Control **2017**, Niedernberg (Germany)

- "*Ultrafast Fluorescence of Photoswitches Captured with the Kerr Shutter*", Joint meeting between GRK2039 and CLiC **2016**, Les Houches (France)

Oral Presentations

- "*Sensitized Two-Photon Activation of Coumarin Photocages*", CLiC Evaluation, **2018**, Frankfurt (Germany)
- "*Exciting Times Ahead for Coumarin Photocages*", External seminar of the Institute of Physical and Theoretical Chemistry, Goethe-University Frankfurt, **2018**, Hirschegg (Austria)
- "*Spectroscopic Studies on a Novel Two-photon Sensitized Coumarin Caged Glutamate Triad*", CLiC summer school, **2017**, Niedernberg (Germany)
- "*Uncaging Dynamics of Caged Glutamate*", CLiC summer school, **2016**, Lindau (Germany)
- "*Ultrafast Fluorescence Captured with the Kerr-shutter*", Joint meeting between GRK2039 and CLiC **2016**, Freudenstadt-Lauterbad (Germany)
- "*Ultrafast Time-resolved Investigations of Mycobacterium Tuberculosis Dodecin*", External seminar of the Institute of Physical and Theoretical Chemistry, Goethe-University Frankfurt, **2016**, Hirschegg (Austria)
- "*Two-photon Uncaging*", CLiC summer school **2015**, Konstanz (Germany)

Erklärung

Ich erkläre hiermit, dass ich mich bisher keiner Doktorprüfung im Mathematisch-Naturwissenschaftlichen Bereich unterzogen habe.

Frankfurt am Main, den .....

Unterschrift

Versicherung

Ich erkläre hiermit, dass ich die vorgelegte Dissertation über

„Spectroscopic Characterization of Photoresponsive Systems: from Chromoproteins to Switchable and Caged Compounds“

selbständig angefertigt und mich anderer Hilfsmittel als der in ihr angegebenen nicht bedient habe, insbesondere, dass alle Entlehnungen aus anderen Schriften mit Angabe der betreffenden Schrift gekennzeichnet sind.

Ich versichere, die Grundsätze der guten wissenschaftlichen Praxis beachtet, und nicht die Hilfe einer kommerziellen Promotionsvermittlung in Anspruch genommen zu haben.

Frankfurt am Main, den .....

Unterschrift